APPLICATIONS OF CORRELATED 2D-ACAR AND DBAR USING A LOW-ENERGY POSITRON BEAM

DISSERTATION

Angelo M. Bonavita, Major, USAF

AFIT-ENP-DS-16-M-056

DEPARTMENT OF THE AIR FORCE
AIR UNIVERSITY

AIR FORCE INSTITUTE OF TECHNOLOGY

Wright-Patterson Air Force Base, Ohio

APPROVED FOR PUBLIC RELEASE; DISTRIBUTION UNLIMITED.

The views expressed in this thesis are those of the author and do not reflect the official policy or position of the United States Air Force, Department of Defense, or the United States Government. This material is declared a work of the U.S. Government and is not subject to copyright protection in the United States.

AFIT-ENP-DS-16-M-056

APPLICATIONS OF CORRELATED 2D-ACAR AND DBAR USING A LOW-ENERGY POSITRON BEAM

DISSERTATION

Presented to the Faculty

Graduate School of Engineering and Management

Air Force Institute of Technology

Air University

Air Education and Training Command

in Partial Fulfillment of the Requirements for the

Degree of Doctor of Philosophy

Angelo M. Bonavita, MS Nuclear Engineering

Major, USAF

March 2016

APPROVED FOR PUBLIC RELEASE; DISTRIBUTION UNLIMITED.

AFIT-ENP-DS-16-M-056

APPLICATIONS OF CORRELATED 2D-ACAR AND DBAR USING A LOW-ENERGY POSITRON BEAM

DISSERTATION

Angelo M. Bonavita, MS Nuclear Engineering
Major, USAF

Committee Membership:

Larry W. Burggraf, PhD, (Chairman)

Dr. Mark E. Oxley, (Member)

Dr. James C. Petrosky, (Member)

Dr. Christopher S. Williams, (Member)

ADEDEJI B. BADIRU, PhD
(Dean, Graduate School of Engineering and Management)

AFIT-ENP-DS-16-M-056

Abstract

The three-dimensional positron annihilation spectroscopy system (3D-PASS) at the Air Force Institute of Technology (AFIT) correlates coincidence Doppler broadening of annihilation radiation (DBAR) with two-dimensional angular correlation of annihilation radiation (2D-ACAR) measurements using two position-sensitive, high-purity germanium (HPGe) detectors. This research integrated a low-energy positron beam with the 3D-PASS, creating a state-of-the-art PAS laboratory at AFIT to probe surfaces of novel materials. The low photoelectric cross section of germanium, combined with the limited output of the radioisotope-based positron beam, produced sparse data necessitating careful data extraction. Processing techniques employed to increase 3D-PASS spectra quality include an improved algorithm for determining radiation-interaction position on HPGe double-sided strip detectors, a momentum sampling function (MSF) based correction scheme and spectra folding informed by crystal symmetries. The three-dimensional nature of the correlated data allowed for leveraging multiple axes of crystal symmetry and producing two-dimensional momentum plots along different projection directions. Integration of the 3D-PASS with a low-energy positron beam enables future studies of enhanced annihilation as well as nondestructive characterization of material surfaces.

Acknowledgements

Success was only possible through much assistance, mentoring, and moral support.

I am grateful to my research committee for their patience and guidance. I would like to thank my advisor, Dr. Larry Burggraf for challenging me to directly confront difficult problems.

Many AFIT faculty and staff contributed significantly. I am indebted to Dr. David Turner for his guidance on ultra-high vacuum systems, and to Dr. Justin Clinton for inspiration during algorithm development. Thanks to AFIT technicians Eric Taylor and Greg Smith, for spending hours with me troubleshooting. Many thanks to the AFIT machine shop, especially Brian Crabtree, Chris Harkless, Jan LeValley, and Dan Ryan.

Equipment integration required vendor assistance beyond normal expectations. I would like to thank Dr. Rod Greaves, for his guidance with the positron beam system. I am also grateful to Dr. Ethan Hull and Mr. Greg Chaffins from PhD Co for HPGe strip detector assistance.

The support from peers, family, and friends was a vital part of this effort. Core support came from peers, including Matt Morello, Greg Van Dyk, Tony Kelly, James Fee, and Mike Dexter. Encouragement from my parents, Mike & Pat Bonavita, though from afar, stoked motivation. Thanks to Matt Turner for keeping me grounded, Tim McClelland for accelerating the literature search, and Elise Thomasson for proof-reading early drafts.

Angelo M. Bonavita

Table of Contents

Page

Abstract iv

Acknowledgements v

List of Figures ix

List of Tables xii

List of Abbreviations xiii

I. Introduction 1

1.1 Brief History of Positron Physics 2
1.2 Positron Annihilation Spectroscopy System (3D-PASS) Overview 5
1.3 Positron Beam Overview 7
1.4 Motivation for this Research 8
1.5 Organization of this Document 9

II. Theoretical Aspects 10

2.1 Momentum Effects on Annihilation Radiation 10
2.2 Positron Interactions with Matter 16
2.3 Segmented Detector Physics 20

III. Experimental Setup 23

3.1 Description of the Positron Beam Source 24
3.1.1 Growing a Neon Moderator 27
3.1.2 Rare Gas Moderator Efficiency 28
3.1.3 Producing Positron Pulses 30
3.1.4 Beam Pulse Width 31
3.2 Positron Propagation Interface 33
3.2.1 Transfer Magnets 34
3.2.2 Target Chamber 34
3.2.3 Positron Energy Control 36
3.2.4 Imaging the positron beam 36
3.2.5 Beam Diagnostic Equipment 38
3.3 Description of the 3D-PASS 38
3.3.1 Spatial Resolution 40
3.3.2 Energy Resolution 41
3.4 Discussion of System Resolution 43

Page

3.5 Distance: Balancing Count Rate and Momentum Resolution . . . 46
3.5.1 Beam Pulse Count Rate Estimate . . . 48

IV. Data Processing and Analysis . . . 50

4.1 Discussion of Data . . . 50
4.2 Incident Radiation Position . . . 52
4.2.1 Full Energy Position Determination . . . 54
4.2.2 Charge Shared Position Determination . . . 57
4.2.3 Position Determination Algorithm . . . 58
4.3 Shared Energy Correction . . . 59
4.3.1 Energy Calculation Algorithm . . . 60
4.4 Momentum Calculation Algorithm . . . 62
4.5 Momentum Sampling Correction . . . 64
4.5.1 MSF Algorithm . . . 66
4.5.2 The Impact of Symmetry on the MSF . . . 67
4.5.3 Center Estimation . . . 72
4.5.4 Symmetry Folding . . . 73

V. Results and Discussion . . . 74

5.1 Interpolation Improvements . . . 74
5.2 MSF Improvements . . . 75
5.3 Copper Standard Source . . . 78
5.4 Lithium Tetraborate . . . 85
5.4.1 Undoped Lithium Tetraborate . . . 86
5.4.2 Silver-Doped Lithium Tetraborate . . . 87
5.4.3 Copper-Doped Lithium Tetraborate . . . 88
5.4.4 Comparison of Lithium Tetraborate Samples . . . 88
5.5 Silver-Doped Zinc Sulfide . . . 91

VI. Conclusions and Suggestions for Future Work . . . 93

6.1 Suggestions for Future Work . . . 93
6.1.1 Equipment Augmentation . . . 93
6.1.2 Further Processing Improvements . . . 94

Appendix A. Momentum Sampling Function Algorithm . . . 96

A.1 Algorithm Development . . . 96
A.2 Correction Stragtegy . . . 98

Page

Appendix B. Maintenance Instrumentation 100

B.1 NIM Bin Setup 100
B.2 Energy Window Setup 102
Bibliography 103

Vita 112

List of Figures

Figure		Page
1	AFIT Positron Annihilation Spectroscopy Laboratory	2
2	3D-PASS	6
3	AFIT Slow Positron Beam	8
4	Momentum Effects on Annihilation Gamma Rays	13
5	Doppler Shift as a Function of Velocity.	14
6	Calculated Positron Implantation Depth in Lithium Tetraborate	18
7	Charge Cloud Creation	21
8	Top View of AFIT Positron Laboratory	23
9	AFIT Slow Positron Beam	24
10	Annihilation Detection During Moderator Growth	29
11	Positron Pulse Detection	32
12	Derivative of Detected Positron Pulse	32
13	Second Derivative of Detected Positron Pulse	33
14	3D-PASS Sample Mount	35
15	Pulsed Beam Spot Image	37
16	Beam Spot Image in Pass-Through Mode	37
17	DSSD Strip Geometry	39
18	Spatial Resolution Experiment Setup	41
19	Schematic view of the 2D-ACAR setup.	43
20	Momentum Resolution as a Function of Distance	47
21	Summary of Event Types in DSSD	53
22	Detector Strip Diagram For Full-Event Measurements	54

Figure Page

23 Detector Strip Diagram For Charge-Sharing Event Measurements . . . 57

24 Comparison of Energy Fraction for Full and Shared Events . . . 59

25 Momentum Sampling Bias Example . . . 64

26 Idealized Momentum Sampling Functions . . . 65

27 MSF for JIMÉNEZ's Spectrometer . . . 71

28 MSF for WILLIAMS' Spectrometer . . . 71

29 MSF Profile for Prior System Configuration . . . 76

30 Comparison of MSF for Configurations . . . 76

31 Comparison of MSFfor Potential Configurations . . . 77

32 Unweighted Copper ACAR Results . . . 78

33 Unweighted Copper Results . . . 79

34 Weighted Copper DBARResults . . . 80

35 Binding Energy versus Doppler Broadening for Copper Sample. . . . 80

36 Copper ACAR with Symmetry Folding . . . 81

37 Copper (100) Plane Momentum Measurement . . . 82

38 3D perspective of Copper Fermi Surface. . . . 83

39 Copper Momentum Magnitude Distribution . . . 84

40 The Calculated Electronic Bulk Band Structure of Lithium Tetraborate . . . 85

41 LTB ACAR Results As Presented By FAGAN-KELLY . . . 86

42 LTB Spectra Produced Using Processing Developed In This Work . . . 87

43 LTB First Brillouin Zone [5, 86]. . . . 87

Figure Page

44 Silver-Doped LTB Momentum 88

45 Silver-Doped LTB Results 89

46 Cu-Doped LTB Results 89

47 Lineshape Parameters for Doped LTB Crystals 90

48 Silver-Doped ZnS Results 92

49 TTL Compliant Detector Setup 101

List of Tables

Table		Page
1	Electrode Potential Settings During Trap Operations.	30
2	Summary of Select System Parameters.	46
3	Example data from Spec72 Data Acquisition System.	51
4	Efficiency in a Representative 5×5 Pixel using Jiménez's reported data.	70
5	χ^2 Metric of Fit	73
6	Improved coincident counts by including charge sharing.	75
7	Line Shape Parameter Summary.	90
8	Components used.	101

List of Abbreviations

Abbreviation		Page
AFIT	Air Force Institute of Technology	1
3D-PASS	Three-Dimensional Positron Annihilation Spectroscopy System	1
PAS	Positron Annihilation Spectroscopy	5
ACAR	Angular Correlation of Annihilation Radiation	5
DBAR	Doppler Broadening of Annihilation Radiation	5
PALS	Positron Annihilation Lifetime Spectroscopy	5
HPGe	High-Purity Germanium	6
RGM	Rare Gas Moderator	7
DSSD	Double-Sided Strip Detectors	21
SCCM	Standard Cubic Centimeters per Minute	28
FWHM	Full Width at Half Maximum	31
SSI	Single-Site Interaction	52
CCE	Close Compton Event	52
MSF	Momentum Sampling Function	65
LCW	Lock-Crisp-West	94
TTL	Transistor-Transistor Logic	100
NIM	Nuclear Instrumentation Modules	100
SCA	Single Channel Analyzer	100
MCB	Multi-Channel Buffer	102

APPLICATIONS OF CORRELATED 2D-ACAR AND DBAR USING A LOW-ENERGY POSITRON BEAM

I. Introduction

Positrons directly probe the three-dimensional electron momentum distribution of metal and semiconductor materials. Positrons have the benefit of avoiding electron-electron correlation effects that affect some measurement techniques. Positrons reveal information about occupied electron energy states as well as the presence of negatively charged defects. Due to their positive charge, positrons are particularly useful in identifying vacancies and other negatively-charged defects with a sensitivity unmatched by other techniques. Low-energy positron beams enhance research by enabling material surface studies. Attempts to study material properties by measuring annihilation radiation is called positron annihilation spectroscopy. This research presents the integration of a low-energy positron beam with a three-dimensional positron annihilation spectroscopy system at the Air Force Institute of Technology (AFIT), and reports processing improvements to the data collected from this one-of-a-kind momentum measurement system.

In 2012, Stephen JIMÉNEZ constructed a Three-Dimensional Positron Annihilation Spectroscopy System (3D-PASS) (Figure 1), based on the doctoral work of Christopher WILLIAMS [52]. In the present research, a slow positron beam system serves as the positron source for the 3D-PASS spectrometer. The addition of this beam system expands the capability at AFIT to study the surface properties of materials, in addi-

tion to, bulk properties. Ultimately, these efforts will culminate in establishing the creation of a capability to measure slow positron resonant-enhanced annihilation at solid surfaces.

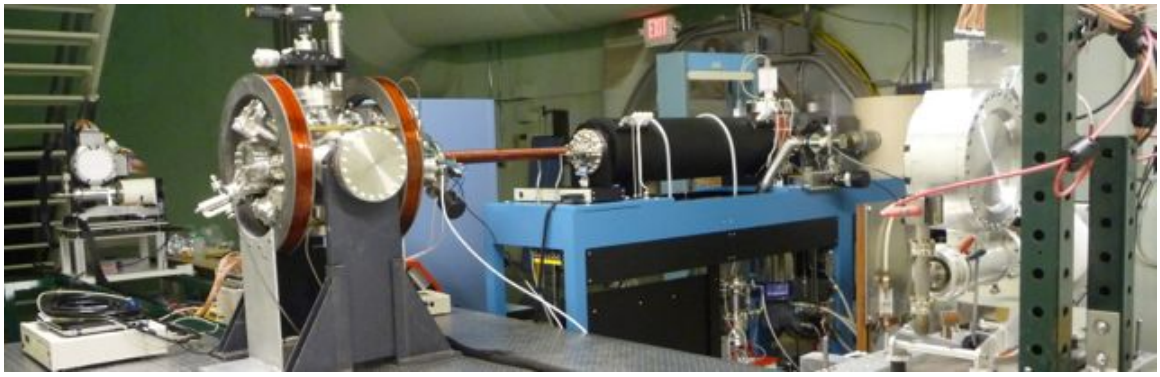

Figure 1. AFIT Positron Spectroscopy Lab: Low-energy positron beam and 3D-PASS spectrometer.

1.1 Brief History of Positron Physics

In 1928, DIRAC wrote that negative solutions to the new quantum mechanical wave equations for electrons could not be simply ignored [25], added further interpretation in a 1930 paper that negative-energy electrons would move through an electromagnetic field as if they had opposite charge [26], and later coined the term 'anti-electron' to describe the unknown particle [27]. This particle would have the same mass as the electron but possess a positive charge. Unaware of DIRAC's prediction, in 1933 a 'positive electron' was experimentally observed by ANDERSON and given the name 'positron' [3]. BLACKETT and OCCHIALINI realized that DIRAC's anti-electron and ANDERSON's positron were the same particle, and started using DIRAC's theory to test experimental observations of positron behavior [14].

DIRAC's prediction included a process where an electron and anti-electron would annihilate each other. DIRAC postulated that perhaps all negative energy states were already filled with electrons, a concept known as the 'Dirac Sea'. Electrons in this sea would not interact with the observable world due to the Pauli exclusion principle. If a negative energy state became available, it would be a hole in the Dirac sea, and interact as an anti-electron. A nearby electron would then be inclined to fill this lower energy state, annihilating both the electron and the anti-electron. In a process similar to the generation of x-rays, radiation would result from the transition with an energy of at least $2m_ec^2$, or 1022 keV, accounting for the combined rest mass of the particles. DIRAC stated that at least two photons would be required to account for conservation of energy and momentum [26]. OPPENHEIMER added that if momentum was conserved by a nearby nucleus, such as in the case of a tightly bound electron, annihilation may result in a single photon [66]. The probability of annihilation with a K-shell electron was calculated by BHABHA and found to be extremely small in comparison to annihilation with free electrons, and concluded two photon annihilation is the most probable mode [13].

ANDERSON noted in his 1936 Nobel Lecture that Joliot and Thibaud were the first to observe annihilation radiation, saying: "The annihilation radiation is of the proper intensity and the energy of its individual corpuscles is approximately the required amount of one-half million electron-volts, corresponding to the complete annihilation of the positron" [4]. KLEMPERER further demonstrated that annihilation radiation occurred in pairs, concluding that single-photon annihilation 'must be extremely rare' [53].

Generally, positrons lose most of their kinetic energy before annihilation. If this was not true, then excess momentum would manifest as a large deviation from collinearity of annihilation photons. ALICHANIAN provided the first experimental

measurement, determining collinearity to within 30 degrees [2]. BERINGER improved this estimate in 1942, confirming that annihilation photons were within a degree of being collinear [10]. This experimental evidence agreed with the theory that the thermalization time of the positron was short compared to its lifetime in a material, meaning that excess momentum could be attributed to the electron. With the availability of improved angular resolution, DEBENEDETTI stated "In general, it is clear that the study of the angular distribution of annihilation radiation with scintillation counters in coincidence will help throw light on electronic momentum distributions, in the atoms and molecules of gases and in liquids and solids" [23].

In addition to an angular effect, the momentum of the positron-electron pair also has an effect on the energy of emitted radiation. As already noted, early measurements confirmed annihilation radiation energies of about one-half million electron-volts [4, 53]. In 1949, the experiments of DUMOND were the first to show a variation in annihilation energies greater than the detector resolution, which DUMOND ascribed to the Doppler effect from the motion of the electron-positron pair with an energy corresponding to conduction electrons in copper [29]. About the same time as DUMOND's experiments, theorists were exploring the positron's role in a strange new atom.

A hydrogen-like atom consisting of a positron and an electron orbiting each other was first proposed by MOHOROVIČIĆ in 1934, as reported in a review by BERKO [12]. A few years later, RUARK suggested the name positronium (Ps) [74]. ORE calculated in 1949 the lifetime of Ps in different spin states: 140 ns for ortho-Ps, annihilating into 3 gamma rays, and 0.125 ns for para-Ps, which decays by 2 gamma annihilation [67]. Using these expected lifetimes, DEUTSCH found evidence of the Ps atom in 1951 [24]. DEUTSCH's technique to measure Ps lifetime lead to experiments by Bell & Graham to measure positron lifetimes in liquids and solids [8].

Collectively, the techniques studying angular correlation, doppler broadening, and positron lifetimes compose the field of Positron Annihilation Spectroscopy (PAS). Only a few years after DeBenedetti's experiments in collinearity, physicists were beginning to use positrons to probe the electrical properties of materials by studying the Angular Correlation of Annihilation Radiation (ACAR) [40]. By 1980, instrumentation had become refined enough to determine the angle between annihilation gamma rays in two dimensions, and 2D-ACAR measurement began to replace its one-dimensional predecessor [11, 90]. Early studies of doppler broadening suffered due to the poor energy resolution of available detectors. The emergence of the first lithium-drifted germanium (GeLi) detectors in the late 1960's improved energy resolution enough to enable the Doppler Broadening of Annihilation Radiation (DBAR) technique [64]. Additional improvements to the DBAR technique would be gained in the late 1970's when detectors were used in coincidence to reduce the effect of background counts [60]. Positron lifetime measurements, now known as Positron Annihilation Lifetime Spectroscopy (PALS), combined with DBAR to form a powerful tool for studying negatively charge defects in materials. The next section provides a brief introduction to the PAS spectrometer used at AFIT, which correlate the ACAR and DBAR measurement techniques.

1.2 Positron Annihilation Spectroscopy System (3D-PASS) Overview

Traditionally, spectrometers provided only a projection of electron-positron momentum distribution. Information about the longitudinal component is determined via DBAR, while the transverse component is measured using ACAR. Simultaneous ACAR and DBAR measurements would allow a researcher to directly measure the 3D electron momentum distribution. Until recently, however, detectors possessing both the position resolution needed for ACAR and the high energy resolution needed for

DBAR were unavailable. In the 1970s, SINGRU attempted to combine these techniques using sodium iodide (NaI) and GeLi detectors in a collinear point-slit geometry to calculate the longitudinal momentum component and one transverse momentum component [77, 78]. In 2010, WILLIAMS used position-sensitive, segmented High-Purity Germanium (HPGe) detectors to simultaneously conduct 2D-ACAR and DBAR measurements of coincident annihilation gamma rays [91].

The AFIT 3D-PASS is a spectrometer for simultaneously measuring all three components of the electron-positron momentum of a target material based on WILLIAM's design. The 3D-PASS is composed of three major components: a target chamber, and two diametrically opposing HPGe detectors (Figure 2). Position-sensitive, high-energy resolution detectors, detailed in Chapter III, are the key element enabling 3D-PASS.

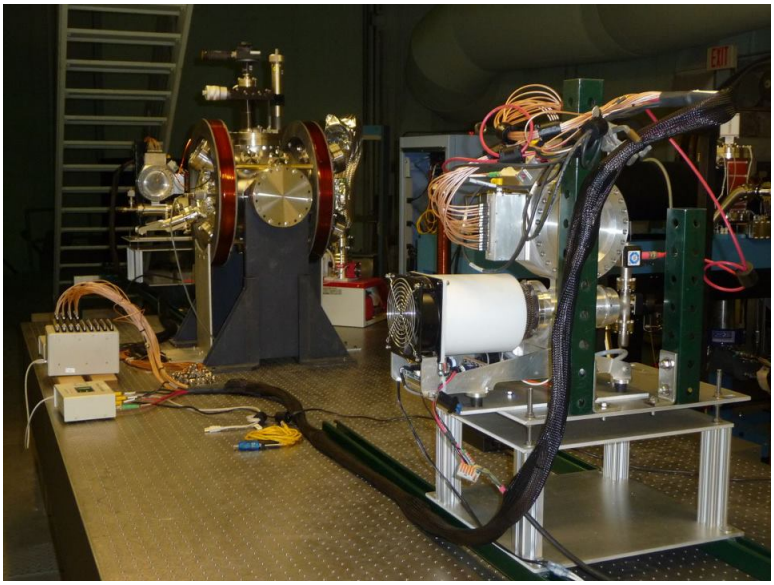

Figure 2. 3D-PASS: A central target chamber flanked by two position sensitive HPGe detectors, Detector 0 in the background, and Detector 1 in the foreground.

Data acquisition and processing is an important challenge in PAS, and considered as part of the 3D-PASS. In some PAS techniques, data collection times are long, due to low counting rates, to collect the counts required to meet statistical goals. Statistical

fluctuation of a histogram bin is related to the square root of the count, so higher counts are required to decrease uncertainty. If finer resolution is required additional counting is required to support additional binning. Additional statistical advantage is gained when the acquired data is corrected, folded, and/or deconvolved, steps which exploit an understanding of the measurement or material. The 3D-PASS data processing capabilities, described in Chapter IV, considers efficiency, geometry, and symmetry.

1.3 Positron Beam Overview

The addition of a slow positron beam enhances the capabilities of AFIT's 3D-PASS. The low-energy positrons from the beam do not deeply penetrate materials, preferentially sampling surfaces, and enabling surface studies. Slow positron beams are also capable of producing positron energies resonant with vibrational and electronic energy transitions, called Feshbach resonances, enabling new research areas. Only a few dozen positron beams permitting the research use of low-energy positrons are operational globally, and few of them operate in the United States. The use of these systems contribute in a range of disciplines to include astronomy, plasma physics, and material science. The AFIT positron beam system depicted in Figure 3 is based on the Surko buffer gas trap design, and consists of two modules. The first module, the Rare Gas Moderator (RGM) supplies a beam of positrons tuned for acceptance by the second module, the Advanced Positron Buffer Gas Trap. The RGM and buffer-gas trap are described in detail in Section 3.1.

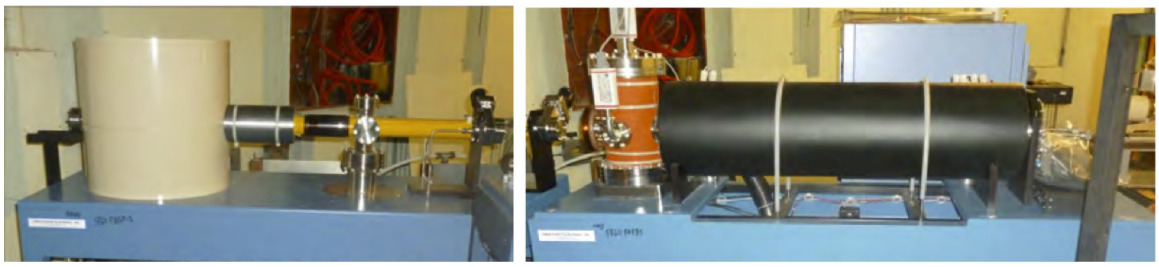

Figure 3. AFIT Slow Positron Beam. Left: RGM module containing ^{22}Na source and solid neon moderator. Right: Advanced positron buffer gas trap.

1.4 Motivation for this Research

Recently published results have sparked interest at AFIT in experimentation with low-energy positrons. Exciting research by GILBERT, IWATA, GRIBAKIN, and BARNES over the past 15 years shows enhanced annihilation rates for positrons at energies resonant with molecular binding energies of some materials [7, 35, 42, 50]. These enhancements may eventually allow for probing specific energy bands in experiments with the 3D-PASS.

In the near term, AFIT has interest in novel electrical materials as part of radiation effects on electronics research. The addition of a low-energy positron source, in combination with the existing 3D-PASS spectrometer, increases AFIT research capability to do comparison studies of surface versus bulk material properties. To this end, AFIT acquired a low-energy positron beam system from FirstPoint Scientific, Inc. in 2009.

WILLIAMS' experiments revealed that simultaneous ACAR and DBAR measurements allow for unique analysis due to the correlation of values in the measured 3D momentum distribution. However, the most recent experiments with correlated ACAR and DBAR measurements from JIMÉNEZ and FAGAN-KELLY resulted in spectra displaying instrumentation artifacts, and therefore obfuscating information. Due to the small data sets collected, on the order of 10^5 samples, algorithms were developed to reconsider previously discarded data to ensure full use of the available information.

The goals for this research include the improvement of spectra quality taken with the 3D-PASS, to explore using the positron beam for surface studies, and to set up future research for exploring Feshbach resonant annihilation studies.

1.5 Organization of this Document

This remainder of this dissertation is divided into 5 chapters.

Chapter II introduces the theoretical aspects of this research. The most important theoretical consideration is positron interaction with matter, which is necessary in understanding the operation of the positron beam and the desired measurement techniques. Topics in this chapter also include positron implantation depth in a material, and background to determine position information from a segmented high-purity germanium detector.

Chapter III describes the hardware of the positron beam system, the 3D-PASS, and associated electronics. The description of the positron beam system consists of information on the moderator and the positron trap, including the rotating wall technique. The description of the 3D-PASS includes an overview of the double-sided strip detectors.This chapter concludes with a description of supplemental detectors and equipment affecting the resolution of the ACAR and DBAR measurements.

Chapter IV discusses data processing and analysis methods. The important data processing steps covered include determining the position of events on each detector, and implementing the spectra correction scheme.

Chapter V presents the results after processing data for all collections including silver-doped zinc sulfate, lithium tetraborate and copper samples. Spectra artifacts present in prior student analyses were removed or reduced due to more accurate positioning algorithms and the use of a new distribution correction scheme.

Chapter VI concludes with discussion of future work.

II. Theoretical Aspects

This chapter presents the theoretical foundation that enable positron annihilation momentum measurements, as well as allow for the production of low-energy positron beams. In particular, this chapter serves as a primer on PAS momentum measurements, positron interactions with matter, and the physics behind the gamma detectors used in the experiment at AFIT.

2.1 Momentum Effects on Annihilation Radiation

PAS methods attempt to extract information about a system by detecting annihilation gamma (γ) rays. The techniques employed in this study probe a material's electron momentum distribution via the momentum distribution of the annihilation radiation. Several assumptions connect the two-gamma (2γ) momentum distribution to the momentum distribution of the electron prior to annihilation.

Energy, mass, momentum, and energy-momentum of the electron-positron system are conserved during the annihilation process. Equation 1 is the energy-momentum relation, which relates energy (E) to the rest mass (m_0c^2) and momentum (p) of a system, where (c) is the speed of light in a vacuum [75]. The relation is applicable to conservation laws before and after annihilation. To determine the value of the momentum in this relation, different frames of reference are considered.

$$E^2 = \left(m_0c^2\right)^2 + p^2c^2 \tag{1}$$

While the momentum carried by the electron-positron system will contribute additional energy to the annihilation photons, this contribution will be particularly small. For example, if the electron-positron system carried a large momentum of 50 keV/c, the total energy would be $\sqrt{1022^2 + 50^2} \approx 1023.22$ keV. An increase of only 1.22 keV

to the total energy, split between the two gamma rays, is within the energy resolution of even the best detectors. The momentum contribution of the most probable annihilations will only add several electron-volts to the measured energy. The total energy carried off after annihilation is also affected by the electron's binding energy.

The electrons being annihilated are bound to a material of interest. The binding energy of the electron to the molecule or atom, will reduce the total energy of the annihilation photons. The total energy of the electron-positron system will be the rest mass minus the binding energy, or $E_t = m_0c^2 - E_b$, contributing to energy-momentum as displayed in Equation 2 . In most cases, the binding energy will be negligible compared to the rest mass energy. While the binding energy of core electrons is significant, annihilation is rare due to repulsion by the positively charged nucleus. Due to the low-energy contribution, and shifting by binding energy, momentum is determined using approaches other than measuring the total energy.

$$(E + E_b)^2 = \left(m_0c^2\right)^2 + p^2c^2 \tag{2}$$

Consider an annihilation event, between a free electron and positron, in the center of mass reference frame. This frame moves with the momentum of the electron-positron system, which has a combined mass $m_0 = 2m_e$, where m_e is the mass of an electron or a positron. The momentum of the annihilation gamma rays $(p_{\gamma 0}, p_{\gamma 1})$ combined accounts for the rest mass of the electron and positron before annihilation (Equation 3).

$$\begin{aligned} E_{before}^2 &= E_{after}^2 \\ \left(m_0c^2\right)^2 &= (p_{\gamma 0} + p_{\gamma 1})^2c^2 \end{aligned} \tag{3}$$

Also consider that, by conservation of momentum, the momentum of the electron-positron system ($\vec{p}_{ep}$) equals the momentum of the annihilation photons, or $\vec{p}_{ep} = 0 = \vec{p}_{\gamma 0} + \vec{p}_{\gamma 1}$. Hence, $\vec{p}_{\gamma 0} = -\vec{p}_{\gamma 1}$, the momentum of both annihilation photons have the same magnitude (p_γ), but the vectors are in opposite directions. Applying this result to Equation 3 leads to momentums of 511 keV/c for each gamma ray (See Equation 4). The momentum of a gamma ray is $p_\gamma = \frac{E_\gamma}{c}$, so it follows the energy of each gamma particle (E_γ) is 511 keV.

$$\begin{aligned} m_0 c^2 &= 2 p_\gamma c \\ p_\gamma &= \frac{m_0 c^2}{2c} = \frac{2 m_e c^2}{2c} = \frac{m_e c^2}{c} = 511 \, \frac{\text{keV}}{\text{c}} \end{aligned} \tag{4}$$

In the laboratory reference frame, as depicted by Figure 4, the momentum carried by the resulting gamma rays will include the momentum of the electron-positron system prior to annihilation. The momentum of the gamma rays can be split into two components: a component perpendicular to center-of-mass frame gamma ray travel ($p_\perp$), shown in Figure 4-A, and a longitudinal component ($p_\parallel$) collinear to the direction of the center-of-mass-frame gamma ray travel, shown in Figure 4-B. Figure 4-C depicts the combined effect. Applying conservation of energy results in Equations 5 & 6.

$$p_\parallel = p_{\gamma 0} \cos\theta_0 - p_{\gamma 1} \cos\theta_1 \tag{5}$$

$$p_\perp = p_{\gamma_0} \sin\theta_0 + p_{\gamma_1} \sin\theta_1 \tag{6}$$

Equations 5 and 6 are simplified by applying small angle approximations. In this approximation, $\sin\theta \approx \theta$ and $\cos\theta \approx 1 - \theta^2/2$. Since the measured angles are on the order of milliradians, the θ^2 term becomes exceptionally small such that $\cos\theta \approx 1$.

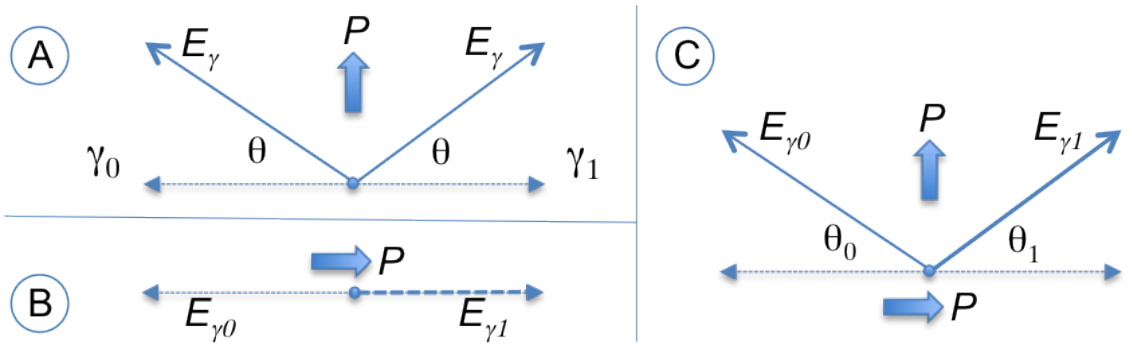

Figure 4. Momentum Effects on Annihilation Gamma Rays. A) Thin dashed arrows represent annihilation in center-of-mass frame. Angled arrows represent the response in the laboratory reference frame with transverse momentum. B) Parallel momentum results in a shift in gamma ray energy in the laboratory frame. C) Combined effect of angular response and Doppler broadening. θ **is exaggerated for visualization.**

Applying the small angle approximation yields Equations 7 and 8.

$$p_{\parallel} = p_{\gamma 0} - p_{\gamma 1} = \frac{E_{\gamma 0} - E_{\gamma 1}}{c} \tag{7}$$

$$p_{\perp} = p_{\gamma_0}\theta_0 + p_{\gamma_1}\theta_1 = \frac{E_{\gamma 0}\theta_0 + E_{\gamma 1}\theta_1}{c} \tag{8}$$

The momentum component parallel to center-of-mass travel, Equation 7, is wholly represented by a shift in energy, a Doppler shift, caused by the original electron-positron momentum. The total amount of the shift is shared among both annihilation photons. For annihilations with non-relativistic electrons, it is reasonable to assume that both annihilation photons have shifted in energy by the same magnitude. Consider the energy of each annihilation gamma as $E_{\gamma_1} = E_\gamma + \Delta E_1$ and $E_{\gamma_0} = E_\gamma - \Delta E_0$, where $E_\gamma = 511\,\text{keV}$. Equation 9 models the energy of photons doppler shifted due to the velocity between reference frames as a fraction of the speed of light [75]. Figure 5 plots the shift in energy of each photon, ΔE_0 and ΔE_1.

$$E_{obs} = \frac{\sqrt{1 + v/c}}{\sqrt{1 - v/c}} \cdot E_{src} \tag{9}$$

While the energy shift between both annihilation gamma rays is not exactly equal, $\Delta E_0 \approx \Delta E_1$ when $v \ll c$, with the difference representing the few eV of energy imparted by momentum. The right side of Figure 5, where the difference becomes appreciable, represents a large doppler shift of about 50 keV. The difference in energy is 1.22 keV, an amount within the energy resolution of most detectors. For the energies probed in this study, assuming $\Delta E_0 = \Delta E_1 \approx \Delta E$ is appropriate.

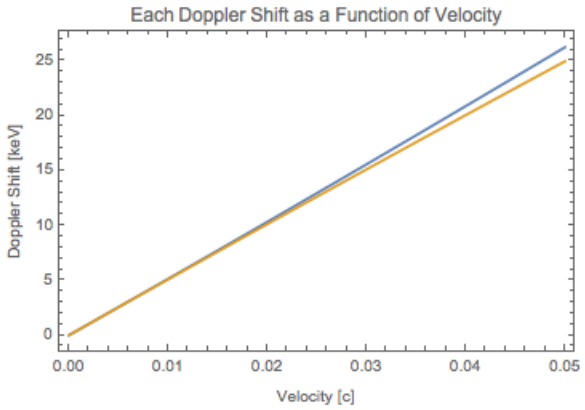

Figure 5. Doppler Shift as a Function of Velocity. The blue line denotes the magnitude of the positive Doppler shift, and the yellow line represents the negative Doppler shift.

Depending on the equipment available, $p_{\|}$ can be measured using either a single detector with high energy resolution, or with two such detectors in a coincident counting arrangement. In a single detector setup, the difference in energy of both gamma rays cannot be directly calculated. Instead, the assumption that the energy of both gamma rays are shifted by the same amount applies, $E_0 - E_1 = 2\Delta E$. Measuring only the energy of one annihilation photon (E), and subtracting the energy due to rest mass (E_γ) yields $p_{\|} = 2\Delta E/c = 2(E - E_\gamma)/c$. By comparison, the two detector setup offers the advantage of greatly reducing the influence of background and enhancing the higher momentum contribution of the spectra. For this reason, the two detector configuration is generally preferred.

The momentum component perpendicular to travel of the center-of-mass annihilation photons, Equation 8, depends on both the energy and angles between annihilation gamma rays. Applying the approximation that the energy of each annihilation gamma is shift by the same amount, $E_{\gamma_1} = E_\gamma + \Delta E$ and $E_{\gamma_0} = E_\gamma - \Delta E$, results in Equation 11. The difference in angles, $\theta_1 - \theta_0$, in Equation 11 is very small, and approximates to zero, simplifying to Equation 12. Since E_γ is assumed constant, this momentum component becomes dependent only on the angle between the photons. The sum of angles θ_0 and θ_1 represent a deviation of the two gamma rays from collinearity, θ_t.

$$cp_\perp = (E_\gamma - \Delta E)\theta_0 + (E_\gamma + \Delta E)\theta_1 \tag{10}$$

$$cp_\perp = E_\gamma(\theta_0 + \theta_1) + \Delta E(\theta_1 - \theta_0) \tag{11}$$

$$cp_\perp = E_\gamma(\theta_0 + \theta_1) \tag{12}$$

$$cp_\perp = E_\gamma\theta_t \tag{13}$$

The momentum determined by angular correlation is reported in the literature using a variety of units. When the value of $E_\gamma = 511\,\mathrm{keV}$ is included, Equation 13 is in the momentum units of $[\frac{kev}{c}]$. Traditionally, angular measurements were reported in units of the angular deviation [mrad], or the equivalent unit $[10^{-3}\,\mathrm{m_e c}]$ when θ_t is in milliradians.

$$cp_\parallel \approx E_{\gamma 0} - E_{\gamma 1} \tag{14}$$

$$p_\perp \approx \frac{E_\gamma}{c}(\theta_0 + \theta_1) = \frac{m_e c^2}{c}\theta_t = \theta_t[m_e c] \tag{15}$$

Equations 14 and 15 connect the momentum distribution of the electron-positron system just prior to annihilation to the 2γ momentum distribution measured, and serve as the basis for the ACAR and DBAR measurement techniques.

An ACAR or DBAR data collection, once binned, inherently integrates over unconstrained, or unresolved, degrees of freedom. Early detectors did not have the energy resolution to resolve DBAR, so spectra integrated over the parallel momentum component. A traditional 2D-ACAR spectrum, $N(p_x, p_y)$, resolves and bins over angle values, summing over an integration direction perpendicular to the detector faces. Equation 16 represents this projection of the 3D momentum density distribution, $\rho(\mathbf{p})$. Once high energy resolution detectors became available, measuring deviations away from the 511 keV annihilation line became popular. These DBAR spectra, $N(p_z)$, sum over all perpendicular momentum components, represented in Equation 17.

$$N(p_x, p_y) = \int \rho(\mathbf{p}) dp_z \tag{16}$$

$$N(p_z) = \int \rho(\mathbf{p}) dp_x \, dp_y \tag{17}$$

The electron-positron momentum distribution is assumed to be an appropriate approximation for the electron momentum distribution due to the low energy of the positron at annihilation. The next section is a survey of the physical processes a positron undertakes prior to annihilation as justification for this assumption.

2.2 Positron Interactions with Matter

The assumption is made that the momentum contribution of the positron is small compared to the electron momentum in the electron-positron system prior to annihilation. This section explores the positron physics needed to understand why that is an appropriate assumption. The same physical processes explain the operation of the slow positron beam discussed in Chapter III.

A positron may be emitted from a radioisotope with an energy of a few hundred kilo-electron-volts. The particle *thermalizes*, losing energy quickly and coming into equilibrium with its environment, as it interacts with a material through several important processes. The positron begins to lose its energy via *ionization* of nearby molecules. Very quickly, within a hundredth of a nanosecond, the positron energy reaches the the ionization threshold. Further energy loss occurs through exciting intermolecular vibrations and glancing collisions with molecules [51]. Once the positron can no longer excite surrounding molecules, the thermalized positron begins to *diffuse* through the material. For detailed information on low-energy positron interactions with matter, see SURKO's review [85].

As a consequence of thermalization and diffusion, positrons with higher energies have broader *implantation profiles* in a material. Control of positron energy can be used to sample a range of depths in a material. Conducting high and low-energy implantation may be used for the comparison of surface and bulk properties [71, 6]. Employing more sophistication, defect-depth profiles can be calculated using computer programs to analyze measurements as a function of incident positron beam energy [55]. For complex, layered materials, often Monte Carlo simulations are built to model implantation profiles [28].

VEHANEN demonstrated the study of multilayer structures was possible by varying the implantation depth in a material using a variable-energy positron beam [87]. Equations 18 and 19 model the implantation profile for monoenergetic positron beams in a material after thermalization, but before diffusion [55].

$$P\left(z,E\right) = \frac{mz^{m-1}}{z_0^m} exp\left[-\left(\frac{z}{z_0}\right)^m\right] \tag{18}$$

$$z_0 = \frac{AE^r}{\rho\Gamma\left(1+\frac{1}{m}\right)} \tag{19}$$

While the fit parameters m, A, and r, are material dependent, the values $m = 2$, $A = 4\,\mu g/cm^2 keV^{-r}$, and $r = 1.6$ are commonly used, along with ρ, the mass density of the sample [69, 31]. Using these common values, Figure 6 depicts the calculated implantation profile of two positron beams at different energies in Lithium Tetraborate ($Li_2B_4O_7$), one of the materials used in this study. A study comparing

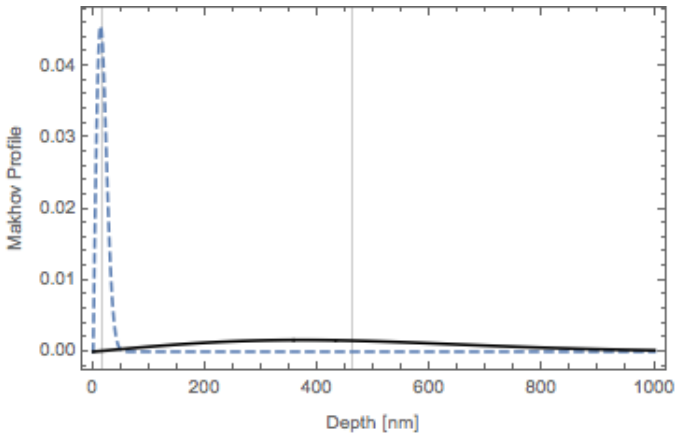

Figure 6. Calculated Positron Implantation Depth in Lithium Tetraborate ($Li_2B_4O_7$). The dashed curve represents a beam of 1 keV positrons, and the solid curve represents a beam of 8 keV positrons. The vertical gridlines represent the mean implantation depth of the distribtuion.

surface and bulk properties would use this type of calculation in the setup of an experiment and the analysis of spectra.

If a positron is implanted at a shallow depth, then it may diffuse back to the surface. Once a positron thermalizes, and before annihilation, it can diffuse up to 500 Å. If the positron implants less than the diffusion length, it may return to the surface. At the surface, the positron may be re-emitted into the vacuum, depending on the material's work function.

The work function of a material is the minimum amount of energy required to remove a solid to a point in the vacuum just outside the solid, and it is a function of surface properties. Since positrons are positively charge, few materials, like Tungsten

moderators, exhibit a *negative work function*. These materials may emit positrons off the surface without requiring additional energy. The effect was first described by COSTELLO as 'positrons which has [*sic*] been thermalized in the moderator and thrown out of a material' [22]. The presence of a surface dipole, which arises in metals due to the tailing of the electron distribution into a vacuum, makes the negative work function possible [21]. In rare-gas solids, like neon moderators, there are no free electrons, so the dipole contribution is smaller and the work function is positive. Despite a positive work function, the rate of energy loss is slower in rare-gas solids, and epithermal positrons reach the surface with enough energy to overcome the barrier, referred to by GULLIKSON as the 'hot positron model' [43]. At the surface of a material, a positron may also form positronium.

For the purpose of PAS, *positronium formation* is a competing processes with 2γ annihilation. If a positron's energy is above the Ps formation threshold of $E_{th} = E_i - E_{ps}$, where E_i is the ionization energy and $E_{ps} = 6.8\,\mathrm{eV}$, positronium can be formed [41]. In momentum sampling, excessive positronium formation can contaminate spectra. For conventional studies, where annihilations take place in the bulk, Ps formation is not usually a concern. However, in the case of surface studies, Ps formation needs to be considered. In materials like Quartz, positronium formation produces a sharp contribution to the spectrum which is not part of the material's band structure.

Annihilation occurs when the positron and electron wave functions overlap, resulting in the emission of $n - \gamma$ rays. Annihilation predominately results in the emission of 2 gamma rays, but may also result in 1, 3, or more gamma rays. If a recoil nucleus is nearby to satisfy conservation of momentum, annihilation may result in a single photon emission. The gamma rays are ultimately detected during experiment. The next section discusses gamma ray interaction with detector material.

Prior to annihilation, the positron may also get trapped in a negatively charged defect. Positrons, being positive, are repelled by the positively charged nuclei at lattice points, and attracted to the negatively charged electrons. At the site of a vacancy or void defect, the nucleus is missing. The positron may then localize at the site, becoming trapped until annihilation.

2.3 Segmented Detector Physics

A segmented, HPGe gamma ray detector detects the annihilation radiation in the 3D-PASS. HPGe detectors are a natural choice for conducting DBAR measurements because they possess a high-energy resolution. A detector with segmented electrodes provides the position information for the detected gamma ray that enable simultaneous ACAR measurements. This section explores the operation of a segmented HPGe detector to inform later discussion on determining position in Chapter IV.

When gamma rays interact with the germanium in a HPGe detector, an atom is ionized. The recoil electron performs a random walk, liberating charges along the path, and setting up a charge cloud on the order of micrometers in size (Figure7) [80]. The detector bias sweeps the positive charge (holes) toward the cathode (AC), and the negative carriers (electrons) toward the anode (DC). This movement of charge carriers sets up an induced charge on the electrodes, as described by the Shockley-Ramo Theorem [47, 76]. The charge cloud diffuses, spreading in size as it traverses the detector, growing to the order of tens of micrometers [56]. As the charge carriers reach each side, the amplitude of the induced waveform on that electrode is proportional to the total charge collected, allowing a measurement of the energy of the incident radiation.

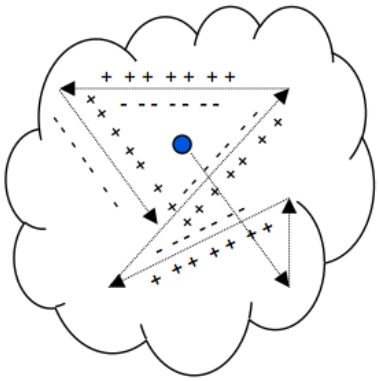

Figure 7. Charge Cloud Creation. When a γ-ray interacts with a crystal, an energetic electron begins a random walk, freeing charge along its path.

If the interaction deposits all of the energy in the crystal volume directly beneath a single electrode on the AC side and a single electrode on the DC side, then the location is immediately known to within an area of the crystal, a pixel, defined by the intersection of the skew collection strips. When two orthogonal strips collect an equivalent amount of charge (within a tolerance), in near coincidence, it follows that the charge cloud was created in the volume directly between the two collection strips. Early efforts to improve the spatial resolution of Double-Sided Strip Detectors (DSSD) focused on using minimal width collection strips. However, another method is available for improving position resolution.

As charges move across the crystal, a waveform is induced on adjacent electrodes. The amount of induced current is proportional to the distance from the cloud, and can be used to determine position information on a segmented HPGe detector within the size of an electrode pixel. Since the induced signal is strongest directly adjacent to the electrode collecting the charges, refinement of the position is achieved by comparing the induced signal on the adjacent electrodes. The details of this method are discussed in Section 4.2. Under the original position interpolation scheme, an event was ignored if the incident radiation deposited its energy between detection strips and each strip

collected a significant fraction of the charge. A method has been developed to reclaim this ignored data, which first requires an explanation of radiation interaction in the detector.

An annihilation photon interacts with the germanium crystal either through photoelectric absorption, or Compton scattering. If the interaction is via the photoelectric effect, the full energy is deposited at that site. If the site is between strips, the charge is collected by both strips. Compton scattering is the more probable effect for 511 keV gamma rays, leading to only a partial deposition of the gamma ray energy near the interaction site, and the remainder escaping in a scattered photon. In some cases, this scattered gamma can deposit the remaining energy elsewhere in the detector, concealing which position was the original interaction site [45]. The method to determine the position of a shared charge event attempts to discriminate against Compton events, and capture additional photoelectric interactions. Processing improvements, including position determination for charge sharing are described in detail in Section 4.2.

III. Experimental Setup

The apparatus used in this research, shown in Figure 8, can be broken down into two major components: the slow positron beam providing the source of positrons and the spectrometer taking the measurements. Coupling these two subsystems is a vacuum chamber and the associated magnets that guide the positron beam onto a target material. This chapter describes the general operation of these subsystems, with some discussion of how each piece contributes to the overall measurement resolution and ability to perform experiments.

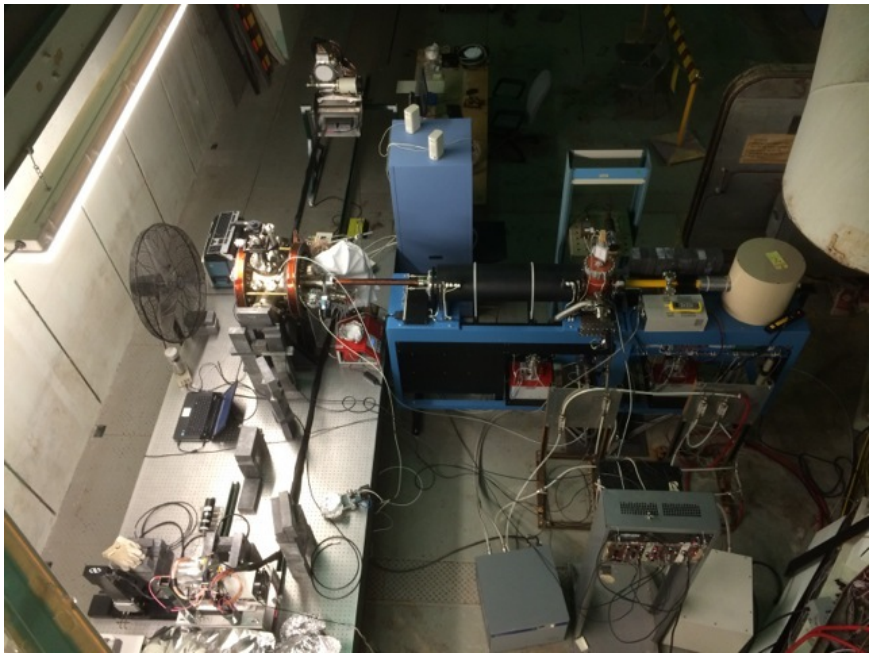

Figure 8. Top View of AFIT Positron Laboratory. Positron are magnetically guided, starting in the RGM (Right), into the buffer-gas trap (Center), and then pulsed into a target chamber (center left). The positron beam forms a 90° angle with the detector axis, formed by a line connecting Detector 0 (top left), and Detector 1 (bottom left). The target chamber magnetic coils are cooled using a high-speed pedestal fan (left).

3.1 Description of the Positron Beam Source

The AFIT positron beam is a FirstPoint Scientific designed system consisting of two modules, shown in Figure 9. The first module, the Rare-Gas Moderator (RGM) uses a solid neon film to moderate positrons into a steady, approximately monoenergetic, stream. The second module consists of a buffer-gas trap that accepts the beam from the RGM, accumulates a population of positrons, further lowers the positron energy, and reduces the beam cross section. The trap then expels a pulse of low-energy positrons for experimental use.

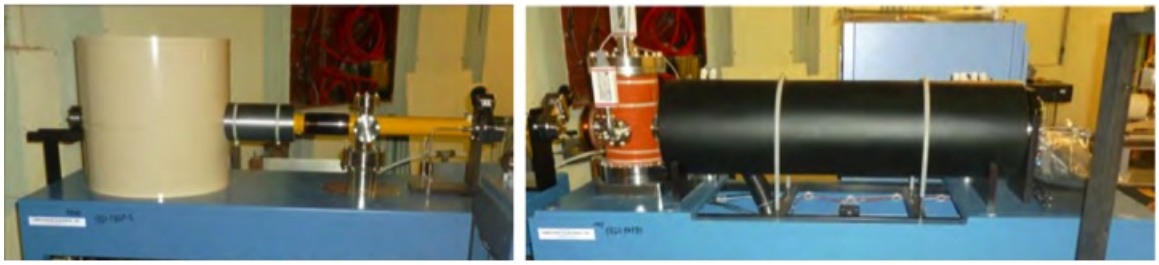

Figure 9. AFIT Slow Positron Beam. Left: RGM module containing ^{22}Na source and solid neon moderator. Right: Advanced positron buffer gas trap.

The goal of the RGM is to efficiently create a monoenergetic beam. The positrons in the RGM originate from an approximately 49.8 mCi ^{22}Na source assayed on 02 October 2012. A fraction of emitted positrons get embedded in a solid neon film grown on a copper parabolic cone adjacent to the source. Some positrons make it back to the surface with enough energy to overcome the positive work function at the surface, and become re-emitted into the vacuum. The energy width of a neon-moderated positron beam (0.58 eV to 1.9 eV) is an order of magnitude greater than a conventional, single-crystal tungsten-moderated beam [62]. However, neon films are

much more efficient. The increased efficiency of the neon moderator is up to 1 % of the source activity [38]. By biasing the copper cone, the positron beam energy is adjusted for acceptance into the buffer-gas trap.

The buffer-gas trap, sometimes called a Surko trap after its designer, is a Penning-Malmburg trap, which uses the combination of a homogenous magnetic field and electrostatic potentials to create a magnetic bottle [15, 84]. A magnetic field runs the length of the trap to radially constrain positrons. The trap contains three electrodes, defining each section, and two gate electrodes to axially reflect the positrons by creating electrostatic potential wells, each deeper in succession. As the positrons traverse the trap, they lose energy through inelastic scatter with the buffer and cooling gases until they come to room temperature (25 meV) in the third section well.

Positrons are admitted into the trap when the first gate potential is lowered below the energy of the incoming beam. Tungsten, a standard moderating material, has a 40 % trapping efficiency in a buffer-gas trap. The energy spread of the incoming neon-moderated beam reduces trapping efficiency to 30 %. However, a neon film creates a beam with an order of magnitude greater positron population, which more than compensates for this slight reduction in trapping efficiency [38]. The positrons become trapped in the electrostatic potential wells after losing energy through inelastic collisions with select gases.

The innovation of the Surko trap is the use of a buffer gas to trap the positrons and a cooling gas to further reduce positron energy. Pressure in each section is maintained through differential pumping driven by a cryopump. Positrons first interact with a low pressure (10^{-4} Torr) nitrogen (N_2) gas, losing energy primarily through electronic excitation [63]. While other gases could be used, nitrogen is the most efficient buffer gas due to a resonant cross section at 8.8 eV [83]. After a single scatter, the lower-energy positrons are then trapped by the higher electrical potential of neighboring

sections. The next sections contain lower pressures, 10^{-5} Torr and 10^{-6} Torr respectively, of buffer gas mixed with a cooling gas. A sulfur hexaflouride (SF_6) cooling gas is introduced into the third section, cooling the positrons through exciting vibrational modes in the gas. The cooling gas serves an additional role of removing energy added to the positron population when compressing the plasma.

The third section of the buffer-gas trap employs a rotating wall technique to compress the positron plasma to a 1 mm diameter. This technique was first used to overcome the drag on confined Mg^+ ions in a Penning trap [48]. It was later applied to positrons contained in a buffer-gas trap [39]. The rotating wall consists of cylindrically segmented electrodes applying a rotating asymmetric electric field, which can further compress the non-neutral plasma being contained. Finally, the compressed population of positrons is released from the trap by dropping the potential of the final gate electrode below the potential of the third storing stage. Positrons can be delivered to the target in two methods, pulse and pass-through modes.

Experiments that do not require the coldest available energies, and that can accept large beam spot sizes, can use the beam originally formed by the RGM directly to avoid losses during trapping. If all trap electrodes are assigned a low potential, and no cooling or buffer gas is introduced, then the trap acts as a large solenoid, transporting the thin steady stream of positrons from the RGM to the target. This is referred to as pass-through mode.

Operating the buffer-gas trap releases a pulse of compressed, room-temperature positrons with about 30 % efficiency. The energy width of the positron pulse from the trap can be as narrow as 18 meV [36], and is the only available method to experiment with Feshbach annihilation resonances. The operation of the buffer-gas trap is discussed further in Section 3.1.3, after first discussing the generation of positrons from the RGM using a solid-neon moderator.

3.1.1 Growing a Neon Moderator.

The neon film used to moderate positrons and create the beam must be periodically regrown. Moderator lifetime is dependent on moderator temperature and the vacuum conditions present [38]. Mills notes the expectation that moderator performance will decrease as the neon film absorbs any contaminates present in the vacuum [62]. Weber notes a moderator decay of 12 % over 2 weeks and ascribes it to the vapor pressure of neon (1×10^{-9} Torr) at 7 K [88]. Cassidy notes an increase in efficiency if the system continues to be pumped during neon admission. [18]. Cassidy was also able to decrease regrowing frequency in his system to once a month by placing an additional pump between the RGM and buffer-gas trap [30]. Gilbert grew a moderator that lasted for multiple months [37]. In our system however, the neon moderator had to be regrown twice a day to maintain a consistent population of positrons entering the trap. The base method follows:

Process to Grow New Moderator

1. *Warming*: Turn off ion pump and helium compressor. Connect roughing pump. Moderator will warm to about 24 K.
2. *Roughing*: Roughing pump will remove gas of previous neon moderator. Pump for 60 s.
3. *Pumping*: Reactivate the ion pump and pump for 60 s.
4. *Cooling*: Disconnect the roughing pump and reactivate the helium compressor with a setpoint of 5 K. Wait for temperature to reduce to 8 K.
5. *Stabilizing*: Use roughing pump to purge neon gas line. Set moderator temperature to 8.8 K and wait for 60s.
6. *Admission*: Disconnect roughing pump from neon line. Deactivate ion pump. Admit neon gas at 3.0 Standard Cubic Centimeters per Minute (SCCM) onto cooled copper cone for 240 s.
7. *Annealing*: Disconnect neon gas. Reactivate ion pump. Raise moderator temperature to 9.3 K for 1000 s.
8. *Finish*: Decrease moderator temperature to 6 K. The positron beam is ready.

3.1.2 Rare Gas Moderator Efficiency.

The efficiency of the RGM module determines the number of positrons that can enter the buffer-gas trap. The AFIT system provided approximately 10^6 positrons per second to the buffer-gas trap. However, rapid decay required moderator replacement twice a day. Significant losses can be realized if contaminates are present in the RGM. The population exiting the RGM can be determined using a scintillating detector pointed at the gate valve connecting the RGM and buffer-gas trap. When the valve is closed, positrons annihilate, creating 511 keV gamma rays. An in-depth discussion of the counting instrumentation setup is found in Appendix B.

The AFIT RGM shows features that more positrons may be available as well. Figure 10 shows the formation of the positron beam during moderator growth. From 0 to 5 minutes, neon gas is admitted into the RGM. The measured positron rate is suppressed

in the first five minutes because the presence of neon gas causes annihilations before the positrons can reach the gate valve. At five minutes, the gas flow is stopped, and the vacuum system reduced the pressure of neon gas, thereby improving positron transport. At 18 minutes, there is a discontinuity in flow. A short circuit in the positron beam magnet caused fluctuations in the applied current. At times, this caused changes to the beam strength. The increase starting at 19 minutes occurred while slowly opening the gate valve between the RGM and the trap. The measured increase of 500,000 additional positrons per second suggests that additional efficiency may be gained by fixing the short in the RGM tube magnet.

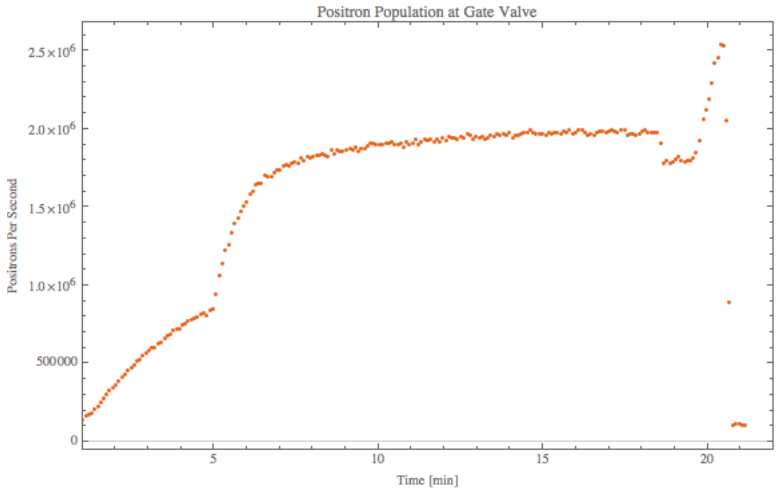

Figure 10. Annihilation Detection During Moderator Growth. Count rate increases as neon is introduced, solidifies, and excess gas evacuated. After an annealing period, temperature is reduced. A sudden shift in count rate is attributed to current shift in the beam tube coil due to the presence of a short circuit. A sharp increase in count rate is noted as the gate valve between the RGM and buffer-gas trap is slowly opened.

3.1.3 Producing Positron Pulses.

The buffer-gas trap operates by cycling through 3 phases: Fill, Store, and Dump. Each phase is defined by setting the potential of the five trap electrodes along with a duration. Table 1 lists the potential settings and duration for each phase. Buffer gas and cooling gas are admitted at a constant rate during all phases. During the Fill phase, positrons are admitted into the trap and increase the positron population of the third potential well section. The Store phase begins by setting the trap electrodes to isolate the third section, and activate the rotating wall, compressing the radial size of the positron population to about 1 mm. Finally, the Dump phase drops the exit gate to release the positron pulse.

Table 1. Electrode Potential Settings During Trap Operations.

(a) Note: Time is in addition to a 4 ms minimum for each phase.

Phase	Time [s]	Gate	Section 1	Section 2	Section 3	Exit Gate
Fill	0.1	2.0	-2.31	-11.48	-20.71	50.0
Store	0.9	2.0	20.00	50.00	12.00	50.0
Dump	0.0	20.00	20.00	50.00	8.00	0.0
Pass	N/A	0.00	0.00	0.00	0.00	0.0

There are tradeoffs between the achievable pulse repetition rate, the population in each pulse, and the energy of the positrons in each pulse. The repetition rate is determined by considering the timing of all 3 phases. There is a minimum time of 4 ms between phases, for a maximum repetition rate of 83.3 Hz. As time in the Fill phase is increased, the positron population of a given pulse increases. Longer store time further decreases positron energy and compresses the population. The Dump phase is kept at its minimum, since the positron pulse takes much less than 4ms to leave the trap.

As noted in Section 3.1, if all of the electrode potentials are set lower than the incoming positrons, the trap operates in a pass-through mode, transporting the positron beam as formed by the RGM to the target chamber. The Pass phase listed on Table 1 lists the potential settings used in the current research to achieve pass-through. The settings are input as an alternate Dump phase and then the trap is run for one cycle. The electrodes retain the value last set so that the dump phase settings become static. These settings remain active until the trap is run again.

3.1.4 Beam Pulse Width.

The time width of the positron beam pulse is driven by the amount of time needed to drop the exit gate potential. During trap operation, a NaI detector detects each pulse of annihilation photons, responding with a pulse height proportional to the positron pulse population. The pulse can then be captured using a fast oscilloscope. Figure 11 represents the smoothed oscilloscope data using a moving average over 30 values, each 2 ns apart. The derivative of the smoothed data (Figure 12) represents the population density of the pulse convolved with the resolution function of the detector and associated electronics. Assuming that the entire positron pulse occurs within the rise time of the detector's pulse signal, and taking the second derivative of that pulse signal over the rise time (Figure 13), the positron pulse Full Width at Half Maximum (FWHM) is estimated as 75 ns.

There exists a maximum positron population desired for each pulse. Since the width of positron pulses are narrower than the response time of the HPGe DSSDs (120 ns), all annihilation events detected from a single pulse will be recorded as coincident. If the positron population is small, and assuming that all events spread isotropically, then there will be a high probability that, at most, only one annihilation event passes through the solid angle subtended by the detectors. If the positron

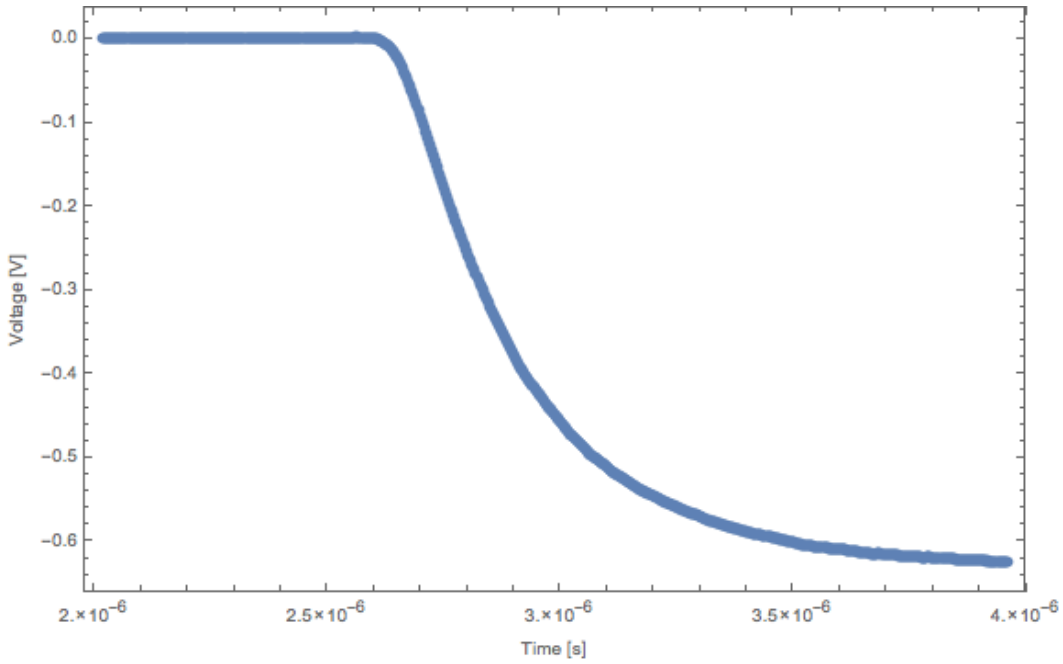

Figure 11. Positron Pulse Detection. NaI detector response due to a positron pulse. The data have been smoothed to reduce noise in the derivative plot.

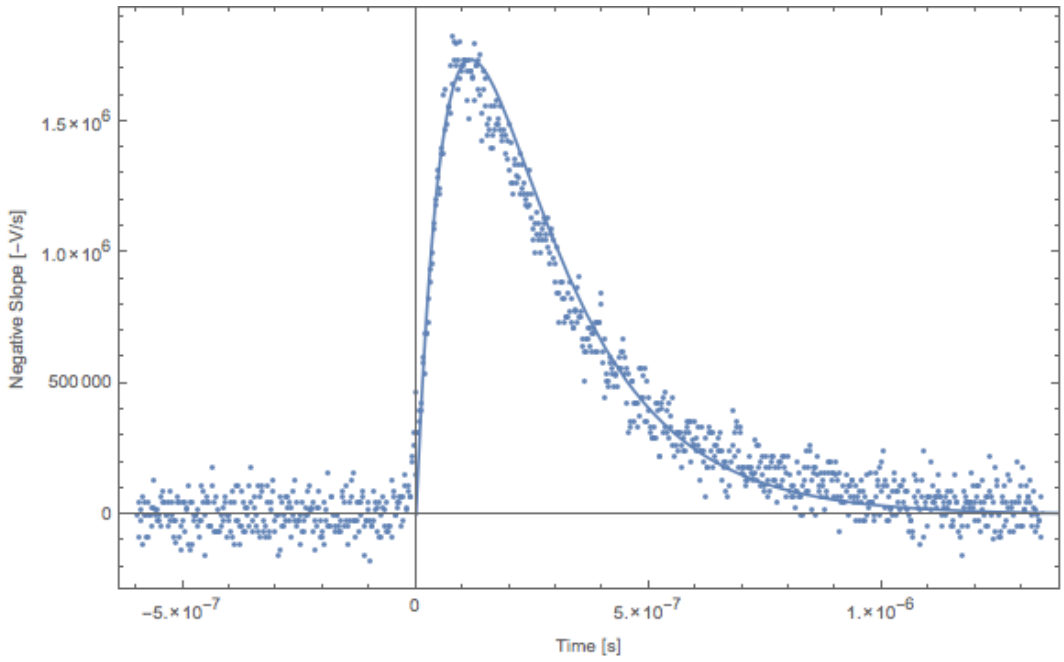

Figure 12. Derivative of Detected Positron Pulse. The fit line models the time response for a NaI detector, $A(e^{t/\tau_1} - e^{t/\tau_d})$, with a time constant (τ_1) of $80\,\text{ns}$ and decay constant (τ) of $230\,\text{ns}$. The coefficient A was set to match the pulse height of the data [54, p.229].

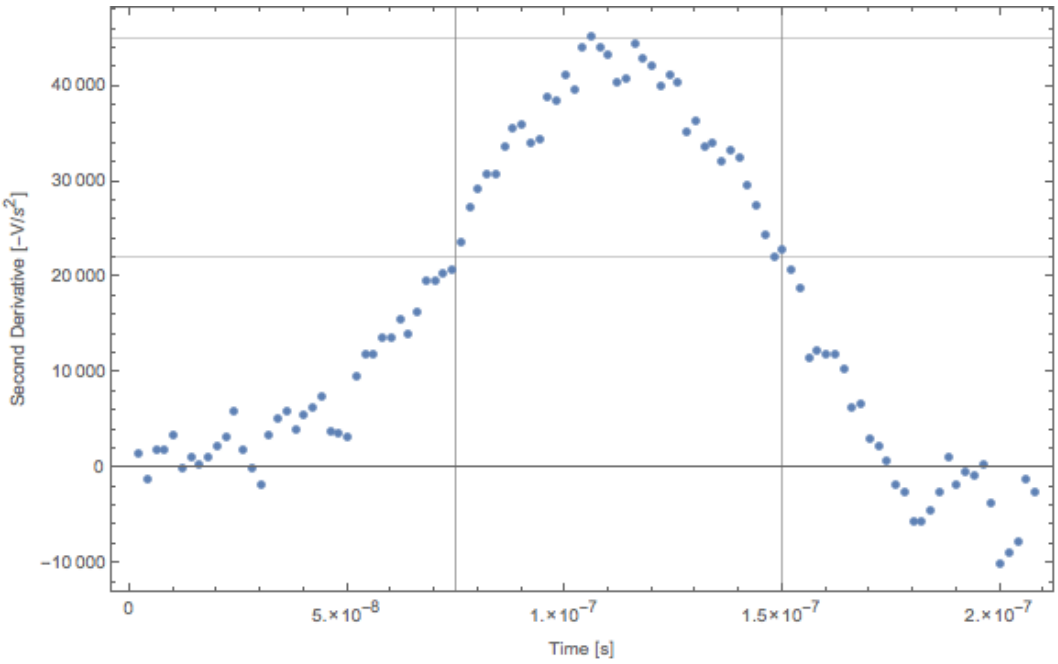

Figure 13. Second Derivative of Detected Positron Pulse. Used to reveal the underlying pulse contributing to the detector rise time. This pulse convolves the positron pulse along with detector response and associated electronics.

population in a given pulse becomes large, then two or more annihilation events may pass through the 3D-PASS detectors. If multiple annihilation events pass through a detector, one detector may detect a gamma ray from one event, while the other detector could detect a gamma ray from a different, independent event. The false coincident point would then pollute the momentum data, and could skew the results.

3.2 Positron Propagation Interface

When a population of positrons is released from the buffer-gas trap, they are guided to the target inside of a vacuum chamber. Divergence of the beam spot size is minimized through the design of the transfer magnets. Positron energy is manipulated using electric bias at the target. Surface studies require as low a pressure as attainable, so the target pressure is kept as low as possible.

3.2.1 Transfer Magnets.

The positron pulse is transported about 4 feet to the target using a set of three magnetic coils collectively referred to as the positron propagation interface. The transfer magnets are air cooled using two pedestal fans set on high during operation. These magnetic guides were designed by JIMÉNEZ [52]. The first coil is a 24 inches long solenoid denoted as the transfer coil, which guides the positrons to an inlet flange on the vacuum chamber with a field generated from 6 A of current. Once in the chamber, the positrons are guided to the target by the magnetic field generated by two Helmholtz coils surrounding the chamber. A 20 A current is split between the two Helmholtz coils, supplying about 10 A each, powered using a 420 W Sorrenson Dual-Power Source.

3.2.2 Target Chamber.

The target chamber is located at the intersection of the positron beam and the 3D-PASS spectrometer. The purpose of the chamber is to maintain high vacuum conditions, and to keep the sample material properly aligned.

The lowest pressure attainable in the AFIT target chamber is 1.5×10^{-6} mbar due to insufficient pumping capacity. An ion pump will be added to the chamber as described in the concluding remarks. Future surface studies will require operating the target chamber in the ultra-high vacuum regime.

The target chamber has two window options. Quartz windows allow 90 % transmission each of 511 keV gamma rays and ensure gamma rays have an unobstructed path to both HPGe DSSD detectors. Aluminum flanges with one-inch centered bore holes, milled with 0.010 inch windows that increase transmission to 98 % are also

available. However, the manipulator arm with current sample holder does not align with the center of the flanges, causing alignment issues. Options are discussed in the Chapter VI.

The target chamber holds the sample mount. Figure 14 depicts a quartz sample mounted in the system target chamber. The sample is fastened to the holder using high-vacuum conductive tape designed for electron microscopes. The sample mount positions a material of interest that is to be both in the positron beam and properly aligned with the spectrometer. Using sample materials larger than the beam diameter prevent positron annihilations on the sample mounting, once proper positioning is attained. Annihilations on structural material add noise to collected spectra. A sample is positioned along the axis of rotation of a manipulator arm to allow rotation for targeting different crystal planes.

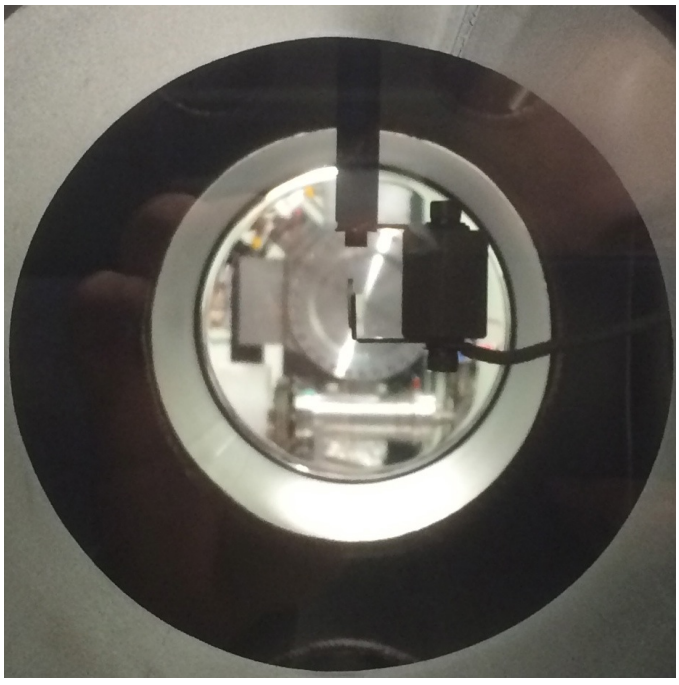

Figure 14. 3D-PASS Sample Mount. A single-crystal quartz sample is mounted in the target chamber aligned with the positron beam (left of figure) and 3D-PASS detector axis (into the page). Detector 1 is visible in the background through the chamber's quartz window. The sample is electrically isolated from the manipulator arm (top of figure) allowing high-voltage bias.

Samples are placed under a high voltage bias for bulk measurements. A ceramic spacer electrically isolates the manipulator arm, kept at ground, from the sample, which may be biased up to 8 keV. The spacer is rated up to 25 kV to enable future options. Biasing the sample mount also permits mounting a phosphor screen for imaging the positron beam.

3.2.3 Positron Energy Control.

Many experiments require fine control over the energy of the positron. For bulk material studies, higher positron energies, 30 keV and greater, ensure penetration into bulk material. Lower energies are useful for surface studies. The energy required for a particular depth can be modeled using Equation 18 introduced in Section 2.2. The cold positron temperatures attainable using the buffer gas trap are useful for studying Feshbach vibrational resonances of positron annihilation. In this research, positron energy was controlled by applying the highest available potential, a 8 keV high voltage bias directly to the source holder and target material, accelerating the positrons as they leave the buffer-gas trap. Accelerating the positrons was also necessary for imaging the positron beam. Future recommendations are discussed in Chapter VI.

3.2.4 Imaging the positron beam.

The sample holder contains screw mounts specifically for a silver-doped zinc sulfide (ZnS−Ag) phosphor screen, as shown in Figure 15. The AFIT beam pulsed spot was first imaged on 24 Oct 14 as depicted in Figure 15, by biasing a phosphor screen to -5kV and imaging with an ATIK 420 CCD camera attached to a Nikkon F35 lens with a 30 min exposure time. The beam spot takes up an estimated area of about 2.6mm by 1.3mm.

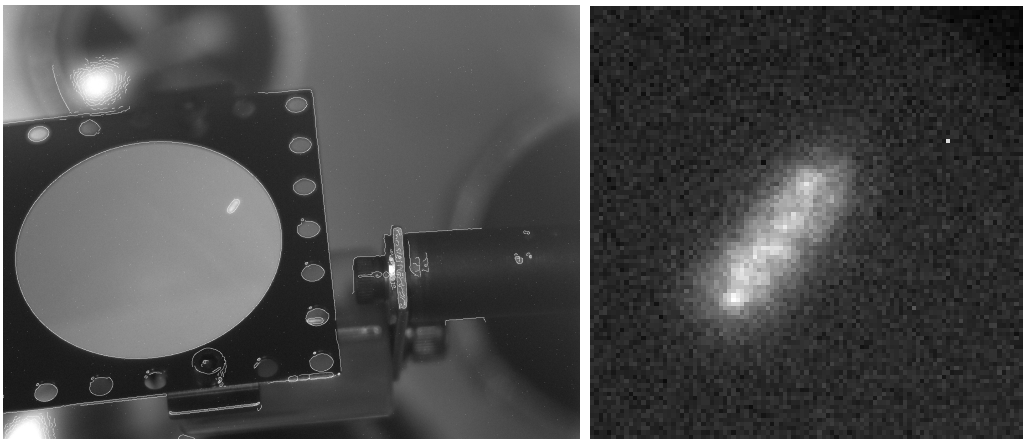

Figure 15. Pulsed Beam Spot Image. Left: Contrast enhanced image of positron pulse spot overlayed onto an image of the phosphor screen room lab illumination. Right: Zoom on beam spot. The beam spot takes up an area of about 2.6mm by 1.3mm, determined using the 3 mm circular holes on the screen as reference.

The AFIT 3D-PASS beam spot produced operating in pass-through mode (see Table 1) was also imaged. This mode increases the rate of positrons on target since trap efficiency does not further reduce the population in the beam. Figure 16 represents the beam spot produced in pass-through mode. The spot measures about 6 mm in diameter with a 3 mm hole in the center.

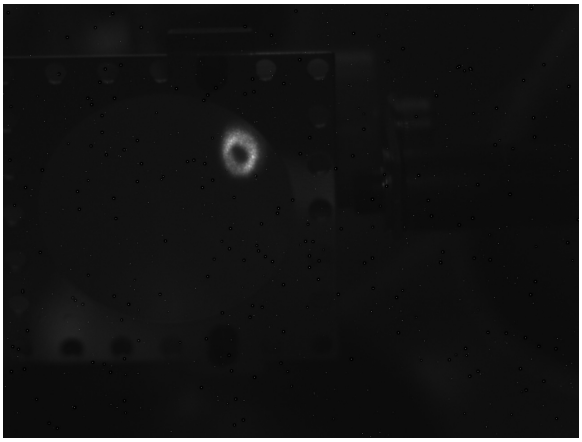

Figure 16. Beam Spot Image in Pass-Through Mode. The beam spot is 6mm in diameter with a 3mm hole inside, determined using the 3 mm circular holes on the screen as reference..

3.2.5 Beam Diagnostic Equipment.

Scintillation detectors were critical beam diagnostic tools. Two NaI scintillation detectors were set up to monitor annihilations at strategic positions in the system.

The first NaI detector was positioned at the gate valve connecting the RGM to the buffer-gas trap. Individual positrons moderated by the RGM would annihilate on the closed gate valve allowing for a positron rate estimation. This detector was connected to the counting electronics described in Appendix B. The RGM controlling software then recorded these counts as part of tracking moderator health.

The second NaI detector was positioned along the 3D-PASS and connected to an oscilloscope. Each pulse of positrons released from the buffer trap would annihilate at the target holder *en masse*, so that the strength of the pulse detected was related to the population of the positron pulse. The buffer-gas trap software would periodically read from this oscilloscope as part of utilities, such as estimating positron lifetime in the trap. Placing this detector near the target chamber, or a 3D-PASS detector would confirm the presence of annihilation gamma rays at various locations coincident with trap operations.

3.3 Description of the 3D-PASS

The purpose of the 3D-PASS spectrometer is to capture the data necessary to perform correlated ACAR and DBAR measurements. Historically, ACAR and DBAR measurements were performed separately, due to the unavailability of suitable detectors. The key information to collect is position data for ACAR measurements and energy data for DBAR measurements. The 3D-PASS simultaneously conducts ACAR and DBAR measurements as described by WILLIAMS [91], JIMÉNEZ [52], and FAGAN-KELLY [32].

The 3D-PASS detectors are two HPGe DSSD from PHDs Co. in Knoxville, TN. Each detector is a 9 cm diameter, single-crystal planar germanium disk with 16 amorphous-germanium contact strips on each side. The cathode and anode sides of the detector are denoted as AC and DC, respectively, referring to the coupling type connecting each contact to its respective pre-amplifier [45]. The AC side has 16 strips oriented vertically, while the DC side has 16 horizontally-oriented strips. Each strip is 4.75 mm wide, with a 0.25 mm gap between each strip, as depicted in Figure 17. Each detector is operated at a bias of about −600 V. A more detailed description of detector geometry is provided by FitzGerald [34]. In addition to excellent energy resolution, each detector provides position information through the use of vertical and horizontal charge collection strips [17, 46, 49]. In this section, the position and energy resolution of the detectors will be described in preparation for a description of the system momentum resolution.

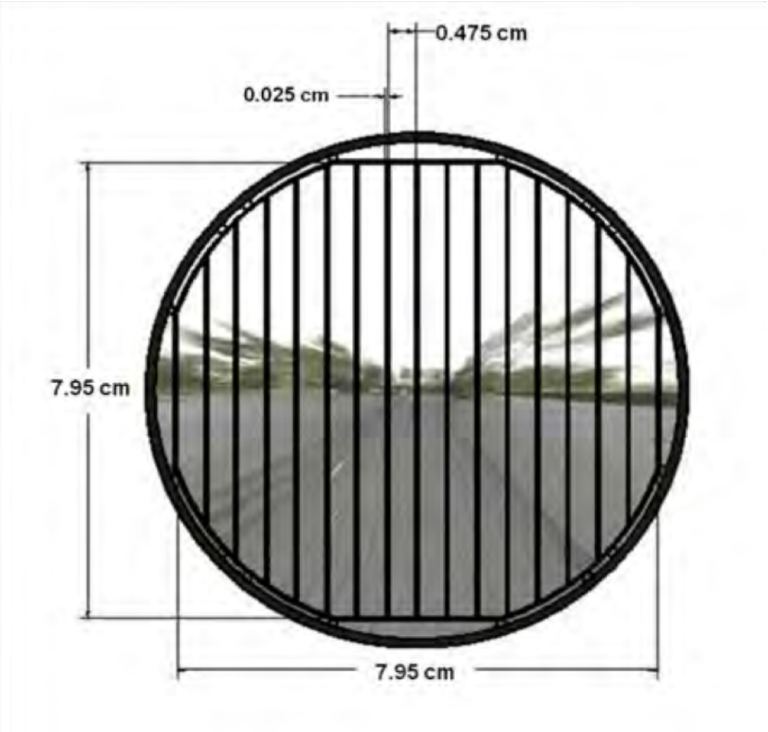

Figure 17. DSSD Strip Geometry. 'AC' side shown.

3.3.1 Spatial Resolution.

An experiment was conducted to determine the position sensitivity and resolution of the 3D-PASS detectors. A third HPGe DSSD PHD Co detector, NP5, was setup as representative of the response of detectors 0 and 1 from the AFIT 3D-PASS. A collimated beam of 662 keV gammas from a 1 mCi ^{137}Cs source was placed on a two-axis linear stage, which itself was placed in front of the detector. The collimator width, described by WILLIAMS as 0.15 mm wide, was much smaller than resolution of the detector, and did not contribute significantly to position broadening [91]. The setup was surrounded by lead shielding to minimize background. The full setup is pictured on the left of Figure 18.

The sensitive volume, the germanium crystal, was assumed to be centered on the detector. A 9 cm paper circle with a printed 5 mm grid, representing the crystal and contact strips was centered over the face for reference. Since the sensitive region of the detector was hidden from view, it was not possible to know the precise location of the incident radiation *a priori*. However, using precision movements of the linear stage by computer control, the true location of the collimated beam was known relative to other collimated data locations.

A C/C++ program, called PlaceCount, controlled the 2-axis linear stage and remotely operated the detector software. The purpose of the in-house code was to place the collimated source in front of a position of the detector and then command the detector software, called Imager32, to count for a period of time. Once counting has completed, the source was placed in a new location to start the next count. The program collected multiple sets of data without experimenter interaction between data sets. The right of Figure 18 depicts all of the 74 collected data sets over a 9 pixel region of the detector. The data collected at each position had a count time of 18 000 s.

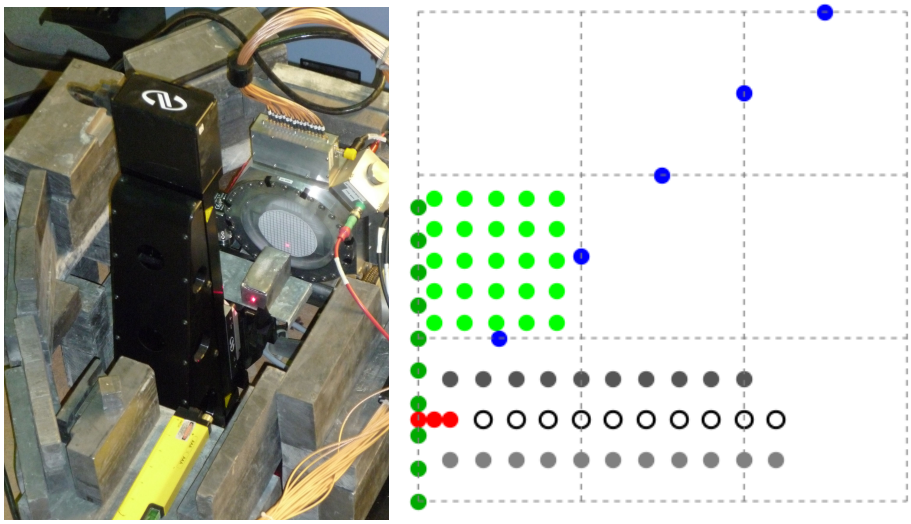

Figure 18. Spatial Resolution Experiment Setup. Left: A linear stage positions a collimator for a spatial resolution experiment. Right: Map of 74 18 000 s-count data sets collected over a 9 pixel section of detector. The colors present different collection series.

PlaceCount's input deck contained 4 commands: `PLACE`, `COUNT`, `STEP`, and `REPEAT`.

1. `PLACE`: Position the linear stage at a defined position.
2. `COUNT`: Command Imager72 to conduct a count for a defined number of seconds
3. `STEP`: Distance to increment the linear stage
4. `REPEAT`: Number of times to repeat program

The position of each event was calculated using the algorithm described in Section 4.2. For each 18 000 s data collection, the centroid position was calculated along with a standard deviation (σ). Assuming a gaussian distribution, the FWHM equals $2\sigma\sqrt{2\log 2}$. Over the 74 points of the detector face probed, the average position resolution (FWHM) was 1.70(8) mm.

3.3.2 Energy Resolution.

The resolution of the momentum measurements in the longitudinal direction is dependent on the energy resolution of the detectors, as will be discussed in Section 3.4. The energy resolution of both 3D-PASS detectors had been previously characterized by

Jiménez and Fagan-Kelly. Both researchers used ^{85}Sr sources since the 514 keV gamma ray the isotope produces is very close to the energy of annihilation radiation, without any additional Doppler broadening [52].

Jiménez placed a 90.9 µCi ^{85}Sr source (assay: December 2010) 15 inches in front of each detector and collected 30 h data sets. The energy resolution was computed for each of 32 collection strips, and then averaged over all strips to calculate a detector average. Detector 0 had an average energy resolution FWHM of 1.92(21) keV, and Detector 1 had an average energy resolution FWHM of 1.84(16) keV [52].

Fagan-Kelly placed a 100.8 µCi ^{85}Sr source (assay: July 2012) 18 inches from each detector and collected 8 h data sets. A 16×16 matrix reported the energy resolution calculated for each pixel. Each detector is composed of 220 pixels, formed by the intersection of two orthogonal collection strips. He calculated 1.827(252) keV for Detector 0 and 1.769(88) keV for Detector 1 . The data from the first two and last two strips on each detector face were removed before calculating the detector averages [32].

There is a difference in the techniques used by Jiménez and Fagan-Kelly. On a DSSD, each collection strip is individually calibrated. When an event occurs, positive charges are collected by a strip on one face and negative charges are collected by a strip on the other face. The energy from each face is recorded, and the accepted event energy is the average of the energy from each face. Fagan-Kelly reported a reduced FWHM compared to Jiménez's values, possibly due to averaging. Since averaging is the expected step in determining the energy of an event, I refer to Fagan-Kelly's reported values for the system's momentum resolution calculation [32].

3.4 Discussion of System Resolution

The overall resolution of the AFIT 3D-PASS is the combination of contributions from both ACAR and DBAR measurements. The resolution of a 2D-ACAR spectrometer is dependent on the spatial resolution of the detector, the annihilation volume in the sample, the distance between the detector and the sample, and the thermal motion of the positron. The resolution of a DBAR system depends on the energy resolution of the detector. In this section, these contributions will be combined to calculate the expected momentum resolution of the AFIT 3D-PASS.

The resolution of the ACAR measurement is limited by the spatial resolution at the source and at the detectors. Equations 20 and 21 are restatements of Equation 15, the ACAR momentum components, in terms of the positions in the detector system, sketched in Figure 19. The error of the momentum measurement is determined using partial derivatives, written out in Equations 22 through 24. The error contribution of the y-momentum component follows similarly to the x-component.

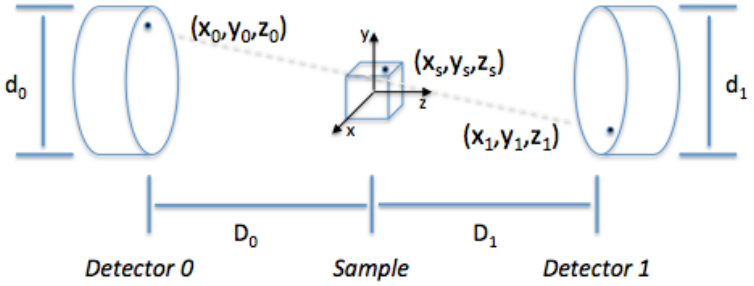

Figure 19. Schematic view of the 2D-ACAR setup.

$$p_\perp \approx m_e c\theta \qquad \text{(15 revisited)}$$

$$p_x = m_e c\left(\frac{x_0 - x_s}{z_s - z_0} + \frac{x_s - x_1}{z_1 - z_s}\right) \tag{20}$$

$$p_y = m_e c\left(\frac{y_0 - y_s}{z_s - z_0} + \frac{y_s - y_1}{z_1 - z_s}\right) \tag{21}$$

$$\frac{\partial p_x}{\partial x_s} = -\frac{1}{z_s - z_0} - \frac{1}{z_1 - z_s} \to \frac{1}{D_0} + \frac{1}{D_1} \tag{22}$$

$$\frac{\partial p_x}{\partial x_0} = \frac{1}{z_s - z_0} \to \frac{1}{D_0} \tag{23}$$

$$\frac{\partial p_x}{\partial x_1} = \frac{1}{z_1 - z_s} \to \frac{1}{D_1} \tag{24}$$

$$\sigma_{p_x} = \sqrt{\left(\frac{\sigma_{x_s}}{D_0} + \frac{\sigma_{x_s}}{D_1}\right)^2 + \left(\frac{\sigma_{x_0}}{D_0}\right)^2 + \left(\frac{\sigma_{x_1}}{D_1}\right)^2} \tag{25}$$

$$\sigma_{p_y} = \sqrt{\left(\frac{\sigma_{y_s}}{D_0} + \frac{\sigma_{y_s}}{D_1}\right)^2 + \left(\frac{\sigma_{y_0}}{D_0}\right)^2 + \left(\frac{\sigma_{y_1}}{D_1}\right)^2} \tag{26}$$

The most significant source of error in the x and y momentum components comes from the error in source annihilation position, followed by error in determining position on each detector face. Equation 22 describes the error due to the imprecision of the annihilation point in the sample. Equations 23 and 24 describe the significance of the error due to each detector respectively. Combining the significant contributions, the estimated resolution in the x and y momentum components are represented by Equations 25 and 26.

The resolution of the z-component momentum, via DBAR measurement, is limited by the energy resolution of the detectors. Equation 27, a restatement of Equation 14, represents the calculation for determining the longitudinal momentum component

($p_{\parallel}$) from an energy measurement. The coefficient $1/c$ is hidden in Equation 27, as it can be considered part of the momentum unit $\left[\frac{keV}{c}\right]$. The partial derivatives in Equation 28 lead to the z component error description in Equation 29.

$$p_{\parallel} \approx \Delta E_t / c \qquad \text{(14 revisited)}$$

$$p_z = E_0 - E_1 \tag{27}$$

$$\frac{\partial p_z}{\partial E_0} = \frac{\partial p_z}{\partial E_1} = 1 \tag{28}$$

$$\sigma_{p_z} = \sqrt{\sigma_{E_0}^2 + \sigma_{E_1}^2} \tag{29}$$

The thermal energy of the positron will also influence the total system resolution of the AFIT 3D-PASS. KUBICA described the impact of the thermal positron motion as "a 'smearing' in the Fermi cutoff of the electron momentum distribution" [58]. FALUB estimates a thermal contribution of 0.7 mrad to the Delft University ACAR system resolution [33]. CEEH at Technische Universität München (TUM) also estimates room temperature positrons having a contribution of 0.67 mrad. In order to decrease this contribution to 0.12 mrad, TUM incorporated a 4 K sample cold finger [19, 20]. Since all AFIT 3D-PASS measurements are at room temperature, a thermal contribution, $\sigma_{th} \approx 0.7\,\text{mrad} \approx 0.7/1000\,\text{rad}$, will be included. Consideration for a cooling sample stage in a future AFIT configuration is discussed in Chapter VI.

The total resolution, as a function of detector distances is delivered in Equations 30, 31, and 32. Conversion factors are present in all three equations to use the common momentum units in literature of $[m_e c \times 10^{-3}]$.

$$\sigma_{p_x} = 10^3 \sqrt{\left(\frac{\sigma_{x_s}}{D_0} + \frac{\sigma_{x_s}}{D_1}\right)^2 + \left(\frac{\sigma_{x_0}}{D_0}\right)^2 + \left(\frac{\sigma_{x_1}}{D_1}\right)^2 + \sigma_{th}^2} \tag{30}$$

$$\sigma_{p_y} = 10^3 \sqrt{\left(\frac{\sigma_{y_s}}{D_0} + \frac{\sigma_{y_s}}{D_1}\right)^2 + \left(\frac{\sigma_{y_0}}{D_0}\right)^2 + \left(\frac{\sigma_{y_1}}{D_1}\right)^2 + \sigma_{th}^2} \tag{31}$$

$$\sigma_{p_z} = \frac{10^3}{m_e c^2} \sqrt{\sigma_{E_1}^2 + \sigma_{E_2}^2} \tag{32}$$

3.5 Distance: Balancing Count Rate and Momentum Resolution

Detector distance from the source critically impacts ACAR spectrometer performance. Section 3.4 introduced the impact of detector distance on the ACAR momentum resolution. Maximizing resolution requires large detector placement distances. The detector distance also impacts the solid angle viewed from the source. The larger the distance, the smaller the measurable momentum range and smaller the counting efficiency. In this section, the tradeoff between these parameters will be discussed.

Since the AFIT system is a 3D momentum spectrometer, comparison of the x, y-component resolution needs to be compared with z-component resolution.

Table 2 summarizes the system characteristics presented in this chapter. Using these values, a model can be built to determine detector distance from the source.

Table 2. Summary of Select System Parameters.

	Beam (Pulse)	**Beam (Pass-Through)**	**Detector 0**	**Detector 1**
Spatial	2.6 × 1.3 mm	6 mm	1.7 mm	1.7 mm
Energy	18 meV	2 eV	1.83 keV	1.77 keV

If the sample is placed vertically, and normal to the positron beam, the beam spot size will only contribute to the y-component measurement, and not the x-component measurement. This leads to an estimated system resolution of the AFIT spectrometer, as shown in Equations 30 and 31, as 3.16 momentum units in the y-direction, and about 0.995 momentum units in the x-direction.

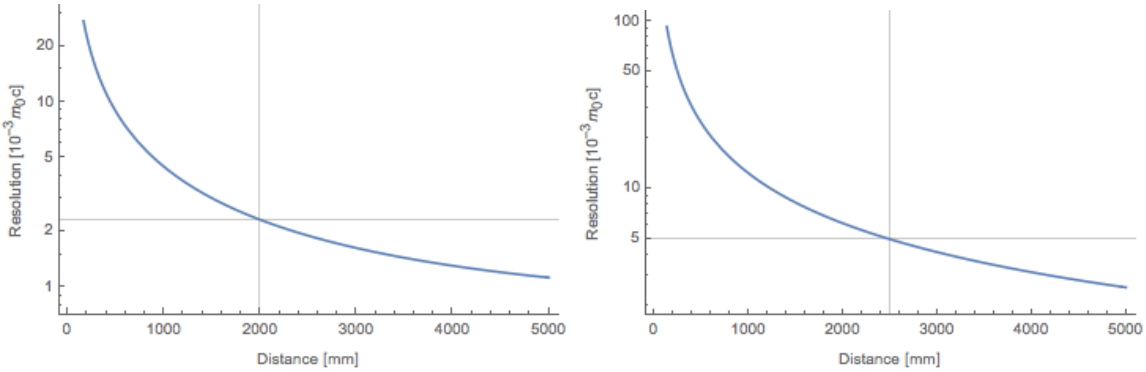

Figure 20. Momentum Resolution as a Function of Distance. Left: Operating with a pulsed beam. When both detectors are placed 2000 mm from the source, the estimated system resolution becomes 1.3 $\left[m_e c \times 10^{-3}\right]$. Right: Operating in pass-through mode. When both detectors are placed 2500 mm from the source, the estimated system resolution becomes 5 $\left[m_e c \times 10^{-3}\right]$.

The improvement in system error needs to be balanced with count rate. Moving the detectors closer to the target improves counting efficiency, but decreases momentum resolution. Suggested bounds can be set based on real-world limitations.

When the detectors are placed too close to the source, momentum resolution decreases. Due to the limits of energy resolution, DBAR spectrometers are recognized as having a lower momentum resolution than ACAR spectrometers. As a recommended lower bound of detector distance, the ACAR resolution should not be less than the DBAR resolution. Using Equation 32, the resolution of the longitudinal momentum component is calculated as $2.5\left[\frac{keV}{c}\right] \approx 5.0\left[m_e c \times 10^{-3}\right]$, corresponding to a minimum distance of 890 mm in pulse mode, and 2500 mm in pass-through mode.

As the detector distance increases, count times will increase as the solid angle intersecting annihilation gamma rays decreases. At AFIT, research supports graduate education and excessively long count times would interfere with student graduation schedules. Count times in excess of a month are too long to support master's research at AFIT, in which only 3 months of dedicated research time is allotted.

3.5.1 Beam Pulse Count Rate Estimate.

When annihilation photons interact with the germanium in the detectors, they may either deposit all of their energy in photoelectric absorption, or Compton scatter. Most of the events where the full energy is deposited will be the result of photoelectric absorption. Germanium has a low photoelectric cross section. The photoelectric cross section is $3.541 \times 10^{-3}\,\mathrm{cm}^2/\mathrm{g}$ [9].

The 3D-PASS suffers from a lower coincident count rate than similarly configured ACAR spectrometers. Germanium has a particularly low photoelectric cross section (σ_{PE}) for a 511 keV gamma of only $3.349 \times 10^{-3}\,\mathrm{cm}^2/\mathrm{g}$ [9]. At this energy, Compton scattering is much more likely. Using a germanium density of $5.323\,\mathrm{g/cm}^3$ and a crystal thickness of 1 cm, the probability of coincident annihilation photons both interacting with the detectors via photoelectric effect (P_{coin}) is calculated (Equation 33) to be only about 3 out of every 10 000 interactions.

$$\begin{aligned} P_{coin} &= (\rho_{ge} \cdot \sigma_{PE} \cdot t)^2 \\ &= \left(5.323\,\mathrm{g/cm}^3 \cdot 3.349 \times 10^{-3}\,\mathrm{cm}^2/\mathrm{g} \cdot 1\,\mathrm{cm}\right)^2 \\ &\approx 3.18 \times 10^{-4} \end{aligned} \tag{33}$$

The count rate is then dependent on the number of annihilation photon pairs that intersect both detectors in a given time. For a given positron source rate $\dot{S}$, interacting with the target material, then the number of photons that intersect the detectors is related to the solid angle that the detectors form with the target, assuming no attenuation in between. If a rate of $1 \times 10^6\,\mathrm{e}_+/\mathrm{s}$ are assumed to interact with the target material, as in Equation 34.

$$\begin{aligned} \dot{S}\Sigma &= \dot{S}\frac{d^2}{8D^2} \\ &= 10^6 \cdot \frac{80^2}{8 \cdot 2000^2} \\ &\approx 200 \end{aligned} \tag{34}$$

At 200 interactions every second, a coincident event is detected by photoelectric effect every 15 s or a count rate of about 240 counts per hour.

IV. Data Processing and Analysis

This chapter describes the processing steps required to extract electron momentum distributions from collected data. The process starts with determining the position and energy information of every detected coincident annihilation gamma pair. From this information, the three component momentum information is calculated. Due to geometric considerations, some momentums are sampled more frequently than others, and this bias needs to be corrected using a correction matrix. The center of the corrected matrix is determined, and if available, the spectrum is folded to exploit crystal symmetry.

4.1 Discussion of Data

The AFIT 3D-PASS Data Acquisition System records detector information for further processing. An example of collected data is presented in Table 3. The table contains the information for two independent gamma interactions, one collected on two strips on Detector 1, and the other collected on three strips on Detector 0. The count column lists the total number of detector strips that make up the gamma ray interaction. In order to determine coincidence between two detectors, the data acquisition system reads from both detectors simultaneously, as if it was one large detector. Any strip events detected within a 120 ns window are treated as in coincidence, since this is the maximum amount of time needed for charge collection. No timing information is provided between events. If the example data had existed in coincidence, it would have been recorded as a 5-strip interaction.

The channel information describes the detector and face of the event. Each collection strip is considered a channel, and labeled with a number in the range 0 to 63. Channels 0 to 31 are assigned to Detector 1, while Channels 32 to 63 are assigned

Table 3. Example data from Spec72 Data Acquisition System.

Event #	Count	Time	Channel	Energy [keV]	F Prev	F Succ
1	2	0	7	174.92	7.71	10.64
2	2	3	28	175.19	19.48	8.90
1	3	0	36	59.13	92.46	6.17
2	3	0	56	189.86	6.59	11.19
3	3	1	35	123.24	5.90	50.08

to Detector 0. The first half of each range represents the detector's DC side, and the second half for the detector's AC side. The algorithms in this chapter use *ch* to refer to the channel number.

Timing information provides the number of clock ticks between strip charge collection. Each clock tick represents 20 ns. The time for the first event will always be zero. Using this timing information, the depth of radiation interaction can be estimated with a resolution of 1 mm.

The last three columns provide energy information. The 'Energy' column reports 'slow' energy, representing the total response of the electrode due to charge collection, and reports the estimated energy deposited. The 'fast energy response', or the induced charge, from the adjacent strips is recorded in the 'F Prev' and 'F Succ' columns. Refining the position of the interaction exploits this information as described in Section 4.2.

The algorithm to process detector data splits up each event as a list of the strip data making up the strip interaction. For example, the detector event variable, or *detEvent*, for the first radiation interaction in Table 3 would contain the first two rows.

4.2 Incident Radiation Position

A 511 keV gamma-ray can interact with germanium in one of two general ways, as described in Section 2.3. First, a charge cloud can be created from an electron excited via photoelectric absorption. Competitively, a high energy electron and a scattered photon may be produced through Compton scattering, depositing energy in separate, incomplete clouds. At the energy of annihilation photons, Compton scattering is the favored interaction.

Three situations are of interest when considering these interactions under grid of collection strips, depicted in Figure 21. The most obvious case is for a single charge cloud created directly under a collection strip. The second consideration is that a single charge cloud is created in the gap between two collection strips, which splits the cloud and a portion of the charge is collected by each adjacent strip. The third situation is that Compton scattering results in a partial energy deposit at one location, and possibly the remainder being collected at a separate detector location. WILLIAMS published a method to determine position information for the first case where the full energy was deposited under a single collection strip on each face [92]. The second two cases required additional study.

Determining the position of gap events was researched by HAYWARD, a 2008 graduate from the University of Michigan. HAYWARD denotes the creation of a single charge cloud as a Single-Site Interaction (SSI), and a recoil photon in adjacent strips as a Close Compton Event (CCE) [45]. Though straight-forward to describe, a challenge exists to identify when an event is SSI or CCE. For the purpose of conducting ACAR measurements, the location and energy of all SSI events are desired. The following assumptions are made when processing 3D-PASS data:

1. If an interaction is collected by only one strip on each face of the detector, it is assumed to be SSI.

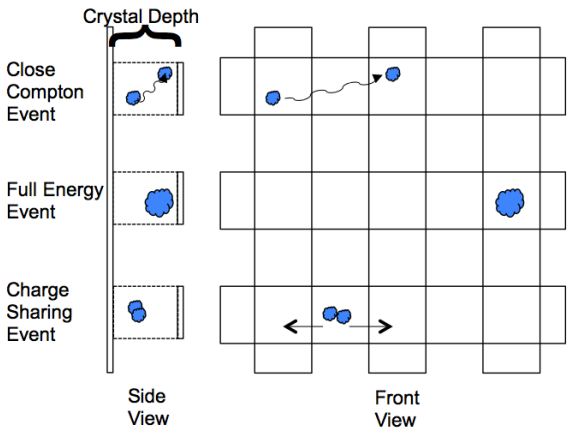

Figure 21. Summary of Event Types in DSSD. If a strip collects the full energy of a gamma ray, it is denoted as a full energy event. If two adjacent strips collect the full energy of a gamma ray, it may indicate a CCE or a charge sharing SSI event, which may be determined by estimating the depth of interaction.

2. If an interaction is collected by two non-adjacent strips, it is discarded as either separate event or a Compton event.

3. If an interaction is collected by two adjacent strips, at equivalent depths in the detector, it is assumed to be SSI.

4. If an interaction is collected by two adjacent strips, at different detector depths, it is assumed to be CCE.

Occasionally, a Compton scatter will result in two charge clouds with similar depth in the crystal, under adjacent strips, and cannot be differentiated from an SSI in the gap. HAYWARD refers to these events as unresolved CCEs, but which only contribute marginally.

JIMÉNEZ described those events fitting assumption one as full energy events, and those fitting assumption three as charge sharing events. The rest of this section will describe determining the position of full energy and charge sharing events.

4.2.1 Full Energy Position Determination.

In literature, a few interpolation schemes have been developed to use induced charges to estimate the position of radiation interactions inside a strip detector [16, 46, 92, 94]. At AFIT position determination for full energy events was previously described by WILLIAMS and implemented by subsequent AFIT students. However, during collimated experiments using the AFIT detectors, significant deviations were found between the actual and calculated position of events near the edge of DSSD collection strips. STEVENSON described this effect as a 'squeezing' of calculated positions towards the center of the strip [81]. Resolving the issue was critical to preserving high-quality angle measurements.

An improved interpolation method was developed for this research. WILLIAMS noted that the total induced charge on adjacent strips of a DSSD is proportional to the distance of the strip from the charge cloud produced by the radiation interaction [91]. Assuming each strip has a pitch w, a coordinate system is set up so that $x = 0$ is in the center of the preceding gap adjacent to the collection strip, as depicted in Figure 22.

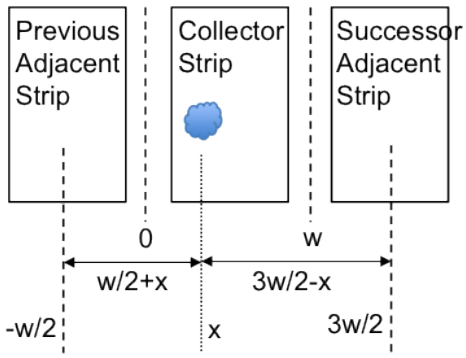

Figure 22. Detector Strip Diagram For Full-Event Measurements. In a strip detector with a strip pitch w, and incident radiation creating a charge cloud at x, the center of the adjacent strips are located at w/2+x and 3w/2-x, respectively.

Following the assumption that the amount of induced charge on a strip, described as the fast energy response, F, is inversely proportional to the respective distance between the charge cloud and the strip, then Equations 35 and 36 represent the induced charge on each adjacent strip, respectively, including a proportionality constant A. The subscript 'p' is used to denote the proceeding strip, and the subscript 's' is used to denote the succeeding strip.

$$F_p = \frac{2A}{w + 2x} \tag{35}$$

$$F_s = \frac{2A}{3w - 2x} \tag{36}$$

The strength of the induced charge, F, also scales with the energy deposited. The parameter A is a function of the charge carriers produced, which is indicative of the deposited energy. In the case of a full energy interaction, the charge cloud appears as a point source with respect to the adjacent strips. The induced charge on each adjacent strip is a result of the movement of the charges from the same cloud, making A of the adjacent strips equivalent.

It can also be useful to show the sum and difference of the fast energy response of the adjacent strips, Equations 37 and 38.

$$F_p + F_s = 2A\frac{4w}{(w + 2x)(3w - 2x)} \tag{37}$$

$$F_p - F_s = 2A\frac{2w - 4x}{(w + 2x)(3w - 2x)} \tag{38}$$

Existing interpolation methods use coefficients built using functions of the induced charge in the adjacent strips to interpolate the position of the incident radiation along the width of a collection strip. The position of the radiation interaction would then

be this coefficient, which I call β, times the strip pitch, w. Equation 39 represents the generalized approach. WILLIAMS called his method linear interpolation, using the coefficient in Equation 40 [92]. WULF used the method of asymmetric position, with the coefficient in Equation 41 [94].

$$x = \beta w \tag{39}$$

$$\beta_{lin} = \frac{F_s}{(F_p + F_s)} \tag{40}$$

$$\beta_{asm} = \frac{F_p - F_s}{(F_p + F_s)} \tag{41}$$

Substituting the representations for F from Equations 35 and 36 into the above representations of β, results in the expected values of β, Equations 42 and 43, given the position of the interaction.

$$\beta_{lin} = \frac{x}{2w} + \frac{1}{4} \tag{42}$$

$$\beta_{asm} = -\frac{x}{w} + \frac{1}{2} \tag{43}$$

Solving for the position of the interaction, x, yields Equations 44 and 45.

$$x = 2w(\beta_{lin} - \frac{1}{4}) \tag{44}$$

$$x = -w(\beta_{asm} - \frac{1}{2}) \tag{45}$$

The interpolation relation used in this research, Equation 44, differs from the originally assumed form, Equation 39. WILLIAMS implicitly assumed that β_{lin}, Equation 40, would range from 0 to 1 across the strip width. Equation 42 suggests that as

the position of interaction moves from $x=0$ on the left to $x=w$ on the right, the value of coefficient β_{lin} will only range from 0.25 to 0.75. The squeezing observed by STEVENSON is a consequence of this range difference.

4.2.2 Charge Shared Position Determination.

The above interpolation technique assumes the full energy of an interaction is collected by a single electrode on both sides of the detector. SSI events in the gap between strips can have their charge collected by both strips adjacent to the gap, preventing use of the above technique. A modified version is possible considering the induced charge located on the subsequent strips, as presented in Figure 23. Following

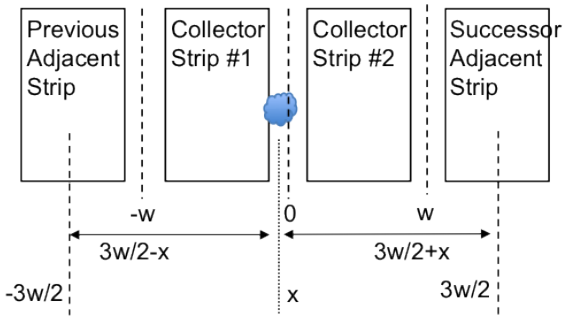

Figure 23. Detector Strip Diagram For Charge-Sharing Event Measurements. In a strip detector with a strip pitch w, and incident radiation creating a charge cloud at x, the center of the adjacent strips are located at 3w/2-x and 3w/2+x, respectively.

the process used in the preceding section, equations defining the charge cloud position are presented in Equations 46 and 47, depending if one chooses to use linear interpolation or asymmetric symmetry.

$$x = 3w(\beta_{lin} - \frac{1}{6}) \tag{46}$$

$$x = 3/2w\beta_{asm} \tag{47}$$

4.2.3 Position Determination Algorithm.

The essence of the process for determining both the full and shared energy position is represented in Algorithm 1. This function takes as input a description of the event $detEvent$, as well as options, and outputs the position as (x, y). The detector event contains the channel number of the incident, ch, and the fast energy response, ξ. Default values for the strip width, w, the size of the face, $dxMax, dyMax$, and the starting channel for the face, ch_i, can be changed using an option.

Algorithm 1 Event Position Function.

```
function eventPosition(detEvent, opts)
    for side ← 1, 2 do
        result[side] ← false                          ▷ Default is false for later error checking
        if ξ_p = 0.0 ∧ ξ_s = 0.0 then
            ξ_p ← 0.001; ξ_s ← 0.001                  ▷ If both are 0.0, set to non-zero values
        end if
        if only one strip in data for side then                                  ▷ Full energy
            result[side] ← (ch − ch_i) ∗ w + 2w(ξ_s/(ξ_p + ξ_s) − 0.25)
        end if
        if two strips in data for side then                                      ▷ Shared energy
            Sort(detEvent)                            ▷ Place events in order by channel
            if channels are adjacent ∧ depth ≤ tolerance then
                result ← (chL − ch_i) ∗ w + 3 ∗ w ( ξ_s/(ξ_p+ξ_s) − 1/6 )
            else
                result ← false
            end if
        end if
        if more than 2 strips in data for side then
            result[side] ← false
        end if
                                                      ▷ Center results
        if result ≠ false then
            if side = 1 then                                                     ▷ AC side
                result ← result − dxMax/2.0
            end if
            if side = 2 then                                                     ▷ DC side
                result ← dyMax − result
                result ← result − dyMax/2.0
            end if
        end if
    end for
    return result                 ▷ result is length 2 array with a value for each side
end function
```

4.3 Shared Energy Correction

Charge sharing occurs when the charges from a single charge cloud located in the gap between strips are split and collected by the two adjacent strips. The energy of original interaction can be constructed by summing the energy estimate from each strip. Comparing this energy sum, to the known energy of the gamma ray results in a charge loss of a few percent. ROSSI attributes the charge deficit to charge trapping near the surface, where the electric field is weak [72].

Figure 24 shows the distribution of the mean energy in a shared event from an AFIT DSSD as a fraction of energy estimate in the single strip using a ^{137}Cs source. The distribution shows two distinct peaks, a peak centered at full energy (1.0), and a peak with an average of 1 % energy loss. Such an error represents a loss of 5 keV of energy, corresponding to a miscalculation in momentum of 10 [10^{-3} $m_e c$], a rather large error for the z-component. To best use the events, an energy correction technique needs to be applied to reduce the effect on the momentum component derived from the DBAR measurement.

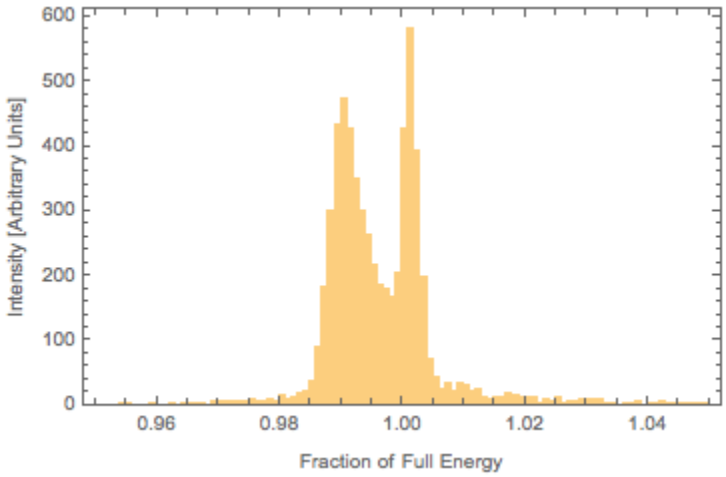

Figure 24. Comparison of Energy Fraction for Full and Shared Events. Detectors collect all charge from a full-energy event, resulting in a sharp peak at a fraction of 1.0. Detectors do not collect some charge from charge-sharing events due to weaker lateral electric fields in the gaps resulting in a peak with a few percent energy loss.

HAYWARD proposed an algorithm to correct for this loss as Equation 48, involving the energy of each shared collection strip, E_1 and E_2, and empirical fit parameters k_1 and k_2. HAYWARD also notes that separate fit parameters are needed for the AC and DC sides of the detector [45]. Using data collected from a collimated source directed in the gap between 2 strips, appropriate parameter values were found: $k_1 = 0.06$ and $k_2 = 0.03$ for the AC side and $k_1 = 0.075$ and $k_2 = 0.035$ for the DC side.

$$E_{new} = E_1 + E_2 + k_1 Min[E_1, E_2] - \frac{k_2 Min[E_1, E_2]^2}{E_1 + E_2} \tag{48}$$

4.3.1 Energy Calculation Algorithm.

In general, each strip is calibrated to report an energy amount for the amount of charge collected. For events composed of two strips, one strip comes from each detector face, and the estimated energy should be equivalent. There is usually a small difference between the energy reported on the two faces. The energy function, EVENTENERGY (Algorithm 2), checks that this difference is not greater than a user definable tolerance, with a default of 50 %. Evaluations for this research changed the tolerance to 10 %. For shared energy events (3+ strips), the mean energy could be deficient by up to 7 %, and a Hayward energy correction is applied. If the energy is outside of the tolerance, the code flags the value as 'False', so that it can be ignored for further processing.

Algorithm 2 Event Energy Function.

function EVENTENERGY(detEvent, opts)
  $ACen \leftarrow$ SUM(energy of each AC strip)
  $DCen \leftarrow$ SUM(energy of each DC strip)
  if AC side is a shared energy event **then**
    $E1 \leftarrow strip1energy$ ▷ Implement Hayward correction method
    $E2 \leftarrow strip2energy$
    $ACEn \leftarrow (E1 + E2) + k1 \cdot \text{MIN}(E1, E2) - k2 \cdot \frac{\text{MIN}(E1,E2)^2}{E1+E2}$
  end if
  if DC side is a shared energy event **then**
    $E1 \leftarrow strip1energy$ ▷ Implement Hayward correction method
    $E2 \leftarrow strip2energy$
    $DCEn \leftarrow (E1 + E2) + k1 \cdot \text{MIN}(E1, E2) - k2 \cdot \frac{\text{MIN}(E1,E2)^2}{E1+E2}$
  end if
  if $\frac{(ACEn-DCEn)}{\text{MAX}(ACEn,DCEn)} \leq eTol$ **then**
    $energy \leftarrow \text{MEAN}(ACEn, DCEn)$
  else
    $energy \leftarrow false$ ▷ Energy outside of tolerance
  end if
  return *energy* ▷ Calculated energy of the event
end function

4.4 Momentum Calculation Algorithm

Once position (x, y) and energy (E) for all coincident points are determined, the momentum is calculated. Equations 14 and 15 were derived in Section 2.1 for calculating momentum, and are stated as found in literature.

$$cp_{\parallel} = \Delta E_t / c \qquad \text{(14 revisited)}$$

$$p_{\perp} = m_e c \theta_t \qquad \text{(15 revisited)}$$

Equations 14 and 15 need to be restated using measured values. Also, ACAR and DBAR measurements are not usually presented in the same units, so Equations 49, 50, and 51 are presented in units of $[10^{-3}\,\mathrm{m_e c}]$, the units for ACAR measurements normally found in literature, and sometimes labeled as milliradians.

$$p_x = 1000 \cdot \theta_x = 1000 \left(\frac{x_0}{D_0} + \frac{x_1}{D_1} \right) \qquad (49)$$

$$p_y = 1000 \cdot \theta_y = 1000 \left(\frac{y_0}{D_0} + \frac{y_1}{D_1} \right) \qquad (50)$$

$$p_z = 1000 \cdot \frac{\Delta E_t}{511\,\mathrm{keV}} = 1000 \cdot \frac{E_{\gamma 1} - E_{\gamma 0}}{511\,\mathrm{keV}} \qquad (51)$$

These quantities can also be expressed in units of $\frac{keV}{c}$, common in the high energy physics community, as in Equations 52, 53, and 54. The pseudocode used for momentum calculation is presented in Algorithm 3.

$$p_x = \frac{E_\gamma}{c} \cdot \theta_x = \frac{E_0}{c}\frac{x_0}{D_0} + \frac{E_1}{c}\frac{x_1}{D_1} \approx \frac{511\,\mathrm{keV}}{c} \cdot \left(\frac{x_0}{D_0} + \frac{x_1}{D_1} \right) \qquad (52)$$

$$p_y = \frac{E_\gamma}{c} \cdot \theta_y = \frac{E_0}{c}\frac{y_0}{D_0} + \frac{E_1}{c}\frac{E_1 y_1}{D_1} \approx \frac{511\,\mathrm{keV}}{c} \cdot \left(\frac{y_0}{D_0} + \frac{y_1}{D_1} \right) \qquad (53)$$

$$p_z = \frac{\Delta E_t}{c} = \frac{E_1 - E_0}{c} \qquad (54)$$

The ACAR instrumentation does not sample angles uniformly, but a correction scheme can be applied to improve the momentum distribution. The next section discusses the algorithm used to correct the measured momentum distribution.

Algorithm 3 Momentum Calculation.

function CALCMOMENTUM(coinEvent, opts)
▷ Coin Evt Format: List of {{Det 0 Evt},{Det 1 Evt}}
$det0Evt \leftarrow coinEvt[All, 1]$; ▷ Detector 0
$det1Evt \leftarrow coinEvt[All, 2]$; ▷ Detector 1
▷ Det Evt Format: List of {{x,y}, En}
$det0Pts \leftarrow det0Evt[All, 1]$;
$det1Pts \leftarrow det1Evt[All, 1]$;

$\{\theta_{x0}, \theta_{y0}\} \leftarrow det0Pts/dist0$
$\{\theta_{x1}, \theta_{y1}\} \leftarrow det1Pts/dist1$
if SameFace **then** ▷ Same detector faces (AC/AC) face source
$\theta_x \leftarrow \theta_{x0} - \theta_{x1}$
$\theta_y \leftarrow \theta_{y0} + \theta_{y1}$
else ▷ Different detector faces (AC/DC) face source
$\theta_x \leftarrow \theta_{x0} + \theta_{x1}$
$\theta_y \leftarrow \theta_{y0} + \theta_{y1}$
end if
▷ Energy Calculations
$det0En \leftarrow det0Evt[All, 2]$
$det1En \leftarrow det1Evt[All, 2]$
$dEn \leftarrow det1En - det0En$

$pz \leftarrow dEn * 1000/511.$ ▷ Units: $10^{-3} m_e c$
$px \leftarrow \theta_x * 1000.$
$py \leftarrow \theta_y * 1000.$
return $\langle px, py, pz \rangle$ ▷ list of 3D momentum points
end function

4.5 Momentum Sampling Correction

After momentum is computed from ACAR data, the distribution is corrected for low-momentum bias in angular sampling. The following discussion on correcting ACAR spectra is based on WEST's description in [89]. Low-momentum events are detected more efficiently than large momentum effects due to finite detector sizes. Figure 25 demonstrates how higher momentum events intersect both detectors less frequently. The lowest momentum events ($\vec{p} \approx 0$) result in collinear annihilation radiation.

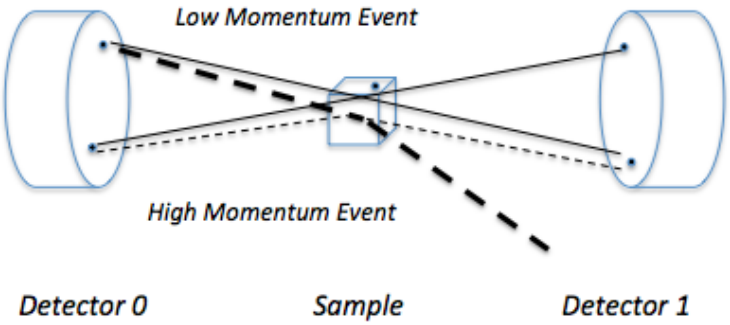

Figure 25. Momentum Sampling Bias Example. The solid lines represent low momentum events, and the dashed lines represent high momentum events. When a low momentum event is rotated, if it intersects one detector, then it also intersects the other detector. However, in higher momentum events, if a detectable event (thin dash) is rotated (thick dash), it may only intersect one detector, and coincident detection is not possible.

Annihilation gamma pairs that differ in deviation from collinearity are not uniformly sampled by the detectors. Assume that a spectrometer is symmetric, with identical detectors placed an equal, but opposing, distance from the target. For annihilation events corresponding to $|\vec{p}| = 0$, the annihilation gamma rays will be collinear. If the direction of one ray passes through one detector, the direction of the other ray necessarily passes through the opposite detector. Thus, the entire detector face is available for detection. As the perpendicular momentum component increases,

the annihilation gamma rays will increasingly deviate from collinearity. Once even a small deviation angle is present, there will exist an orientation where one ray will pass through a detector, but the other will not intersect the opposite detector. As the deviation angle increases, the opportunity for coincident detection decreases.

Thus, annihilations corresponding to low-momentum events are more easily sampled than annihilations from higher momentum events. The mapping of the efficiency of measuring a particular momentum is referred to as the Momentum Sampling Function (MSF), a tent-like function as depicted in Figure 26. The MSF of a symmetric spectrometer forms a peak that can cause problems with correction. WEST suggests offsetting detectors by 15 % to avoid singularities [89]. Idealized examples of slightly asymmetric systems are also presented in Figure 26.

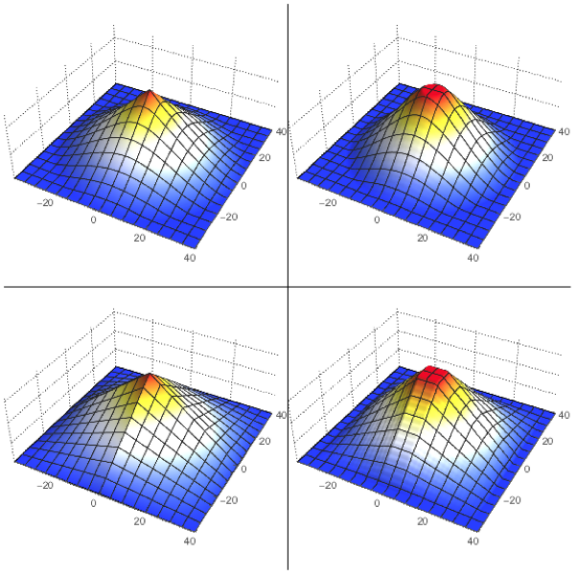

Figure 26. Idealized Momentum Sampling Functions. The form of the momentum sampling function for different arrangements of identical square and circular aperature detectors. The top row represents circular detectors and the bottom row represents square detectors. The left of the figure models a symmetric system, while an asymmetric system is modeled to the right.

A critical angle, θ_c, exists which cannot be simultaneously detected by both detectors. If momentum causes a deviation greater than θ_c, it will not be detected. For detectors placed differing distances from the source, each will have a different maximum angle detectible, θ_m, referenced from the detector axis. The sum of the two maximum angles, $\theta_{0m} + \theta_{1m}$ represents the critical angle, θ_c, detectable by the spectrometer. Thus, the MSF represents the ability to sample momentum values ranging from collinear gamma rays, to deviations of collinearity up to θ_c. Since the larger momentum are sampled less often, a correction factor is applied to compensate for the bias. The next section will introduce generating the MSF, and implementing the correction strategy, while a full discussion is presented in Appendix A.

4.5.1 MSF Algorithm.

The measured ACAR distribution (M) is the true distribution (N) times the MSF (c), as shown in eq 55 [89]. The MSF is the convolution of the efficiency map (ε) of each detector face over the range of measurable angles (θ, ϕ) as described in eq 56. The double integration takes place over all possible radiation orientations $(\bar{\theta}, \bar{\phi})$ incident on face of the detector. The efficiency map of a detector is the likelihood of a gamma ray being detector at a position, and can be represented as a map, ϵ_{ij}, of the relative efficiency at a binned position at (i, j). The pseudocode of the CALCMSF function, Algorithm 4, implements a discretized summation, Equation 57, due to the non-continuous efficiency matrix.

$$M(\theta, \phi) = c(\theta, \phi) N(\theta, \phi) \tag{55}$$

$$c(\theta, \phi) = \iint d\bar{\theta}\, d\bar{\phi}\, \varepsilon_1(\bar{\theta} + \theta/2; \bar{\phi} + \phi/2)\, \varepsilon_2(\bar{\theta} + \theta/2; \bar{\phi} + \phi/2) \tag{56}$$

$$c(\theta, \phi) \approx \Delta\bar{\theta}\, \Delta\bar{\phi} \sum\sum \left(\varepsilon_1(\bar{\theta} + \theta; \bar{\phi} + \phi)\, \varepsilon_2(\bar{\theta}; \bar{\phi})\right) \tag{57}$$

To calculate the MSF, a map of the efficiency, $\epsilon_{i,j}$, across each detector face is calculated. This map is more than just the intrinsic ability of the detector to detect a gamma ray, but reflects the ability of the whole spectrometer to allow a gamma to reach the detector. WEST suggests that this efficiency should be recalculated for every sample, with the sample positioned as measured, which serves to include any effects from self-shielding. Since this efficiency measures the relative probability that an annihilation gamma will be detected by a particular bin, it necessitates that the usual coincident requirement is relaxed. In traditional 2D-ACAR systems, separate measurements are taken enabling and disabling coincidence to gather the required information [89]. Fortunately, coincident and non-coincident information is collected simultaneously by the 3D-PASS, allowing for the MSF calculation to be part of the data analysis workflow [89].

4.5.2 The Impact of Symmetry on the MSF.

When a 2D-ACAR spectrometer is composed of two identical detectors an equivalent distance from the source, the system is considered symmetric. Symmetric systems optimize several variables related to count rate, and solid angle. However, when the detectors of a symmetric system have similar periodic efficiency constructive interference can result in wide variations in momentum sampling.

The efficiency of the detector can add artifacts to collected spectra. It was also noted by WILLIAMS, JIMÉNEZ, and FAGAN-KELLY, that efficiency of the edges of the DSSD strips are much less than at the center of the strips. This resulted in a significantly-varying periodic efficiency across the detector face. The severity of the observed effect was due to the combination of the choice of interpolation method and

Algorithm 4 Calculating the Momentum Sampling Function (Part I).

function CALCMSF(momentumPoints, det0Eff, det1Effs)

▷ Setup initial variables

▷ Options passed into function: ($detectorWidth$), detector distance from source ($dist0, dist1$)

$subMax \leftarrow \text{LENGTH}(\epsilon_0)$

$sw0 \leftarrow detectorWidth/subMax$

$sw1 \leftarrow detectorWidth/subMax$

$dist0 \leftarrow distanceDet0$

$dist1 \leftarrow distanceDet1$

$res0 \leftarrow sw0 * 1000./dist0$ ▷ Determine angular resolution

$res1 \leftarrow sw1 * 1000./dist1$ ▷ of each detector in mrad

if $res0 > res$ **then**,

$resM \leftarrow res0$

$\theta_{max} \leftarrow res0 * (subMax - 1)$

else

$resM \leftarrow res1$

$\theta_{max} \leftarrow res1 * (subMax - 1)$

end if

$Mmax \leftarrow \text{FLOOR}(\theta max/resM)$

▷ (Store dimensions of the MSF matrix for later padding)

$Mpad \leftarrow 2 * (Mmax) + 1$

LOAD efficiency matrices of each detector (ϵ_0, ϵ_1)

$cBin \leftarrow Mpad/2. + 0.5;$ ▷ Find Center Bin (0)

for $i \leftarrow 0, Mpad$ **do** ▷ Bin Specification

$bMSF[i] \leftarrow resM * (i - cBin + 0.5)$

end for

for $i \leftarrow \text{FLOOR}(-(subMax - 1)/2), \text{FLOOR}(\frac{subMax-1}{2})$ **do**

for $j \leftarrow \text{FLOOR}(-(subMax - 1)/2), \text{FLOOR}(\frac{subMax-1}{2})$ **do**

$\theta_0 \leftarrow res0 * i - res0/2, res0 * j - res0/2$

$\theta_1 \leftarrow res1 * i - res1/2, res1 * j - res1/2$

end for

end for

$\theta_{0p} \leftarrow Partition[Flatten[\theta_0], 2];$

Algorithm 5 Calculating the Momentum Sampling Function (Part II).

```
    for {θ̄, 1, subMax}, {φ̄, 1, subMax} do                    ▷ Finding Spectral Center
        hold ← Transpose(θ_0p[All, 1] − θ_1[θ̄, φ̄][1], θ_0p[All, 2] − θ_1[θ̄, φ̄][2])
35:     hold2 ← Partition(hold, subMax)
        Δθ_T ← hold2[x, y][x, y]
    end for
    pos ← Floor[Δθ_T[[All, All]][[All, All]]/resM + (Mmax + 1.5)];
                                                    ▷ pos stores the bin position
40: for θ̄ ← 1, subMax do                                        ▷ Calculate MSF
        for φ̄ ← 1, subMax do
            for θ_i ← 1, subMax do
                for φ_i ← 1, subMax do
                    MSlice[θ_i, φ_i] ← ϵ_0[θ_i, φ_i] · ϵ_1[θ̄, φ̄]
45:             end for
            end for
            Pad MSlice as MSF based on θ̄, φ̄
            PadRight(
            Flatten(pos[[θ̄, φ̄]], 1)− > Flatten[Mslice]), Mpad, Mpad]
50:         MSF ← MSF + MSlice
        end for
    end for
    cS ← 15                                              ▷ Scale MSF to peak value
    sM ← Floor[Mpad/2 + cS/resM]
55: mScale ← Max[Mc[[−sM; ; +sM, −sM; ; +sM]]]
    nMSF ← Mc/N[mScale]
                                                        ▷ Build Weighted list
    for all row, 1, Length(momentumPts) do
        indices ← getBinIndex(momentumPts[row], bMSF)
    end for
60: for i, 1, Length(indices) do
        wList[i] ← nMSF[index[i]]                ▷ Build list of MSF values at indices
    end for
    if Count[wList,0.]=0 then                    ▷ Check for zero before inverting
        nwList ← 1./wList                                ▷ Export Weighted List
65: else
        nwList ← {}
    end if
    return {bMSF, Mc, nwList}                          ▷ bins, array, and weighting list
end function
```

ignoring of charge sharing events. The efficiency of a representative pixel, generated using data collected by Jiménez, is produced as Table 4. This efficiency reduction at strip edges had a significant effect on how momenta was sampled by the spectrometer.

Table 4. Efficiency in a Representative 5×5 Pixel using JIMÉNEZ's reported data.

	1	**2**	**3**	**4**	**5**
1	0.0190265	0.0490639	0.0484341	0.0474071	0.0183717
2	0.16863	0.794816	0.834812	0.737318	0.152914
3	0.185556	0.951251	1.000	0.894164	0.170627
4	0.155755	0.729331	0.772258	0.670616	0.142765
5	0.0147252	0.0371048	0.0386685	0.0359954	0.0142028

The MSF of the spectrometer created by JIMÈNEZ is represented by Figure 27. The MSF from this symmetric system contains many sharp peaks & valleys, many singularities, which make correcting the ACAR spectra particularly difficult. The low efficiency of strip edges manifested as a significant variation in momentum sampling. The peaks and valleys of the MSF represent momentums preferentially sampled and ignored. Momenta represented by an angle formed between the center of a strip on one detector, and the edge of a strip on the opposite detector were under-sampled due to low efficiency. The pitch of 5mm corresponds to a deviation with an integer multiple of 2.5 milliradians.

To avoid suppressing periodic angular sampling due to periodic efficiency losses, a 2D-ACAR spectrometer may be setup to be asymmetric. Additionally, similar periodic detector efficiency across both detector faces enhances artifact creation. Other 2D-ACAR spectrometers configure one detector rotated 90^o from each other to prevent aligning periodic efficiencies and enhancing artifacts [89]. The manufactures of the AFIT 3D-PASS detectors, PHD Co, recommended that the detectors not be rotated for mechanical reasons.

WILLIAMS collected spectra that did not display the sampling bias observed in JIMÉNEZ's spectra by serendipitously having an asymmetric system. While the detectors of WILLIAMS' spectrometer were placed equidistant from the target, he used detectors from two different companies, of different sizes. Using his reported average

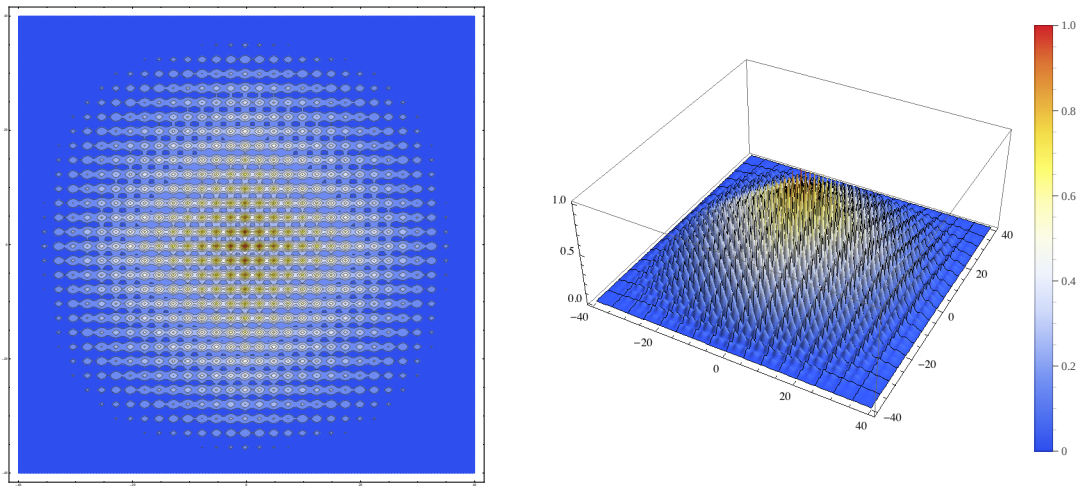

(a) Overhead View. (b) 3D View.

Figure 27. MSF for JIMÉNEZ's Spectrometer. The MSF of the previous 3D-PASS configuration calculated for comparison using JIMÉNEZ's copper source data. The peaks and valleys result from detector efficiencies with periodic gaps placed symmetrically about the source. [52].

efficiency values, Figure 28 recreates the MSF for his setup. The spectrometer created by WILLIAMS sampled momenta fairly evenly within the bounds of -4 to $4\,[10^{-3}\,\mathrm{m_e c}]$, and could effectively sample up to $12\,[10^{-3}\,\mathrm{m_e c}]$.

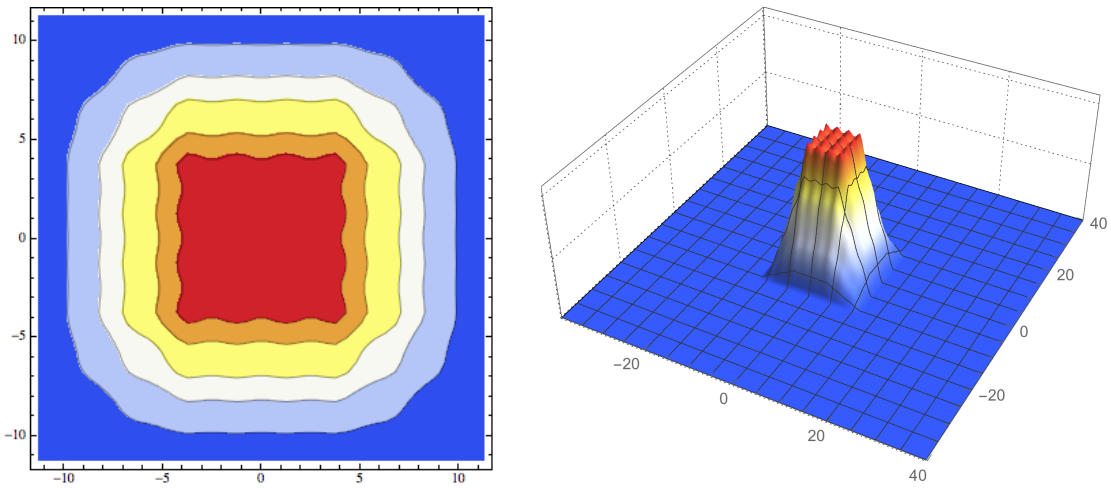

(a) Overhead View. (b) 3D View.

Figure 28. MSF for WILLIAMS' Spectrometer. The spectrometer configuration used two detectors with different face sizes placed equidistant from the source to create an asymmetric system. This MSF was generated using WILLIAMS' reported efficiency data [91].

4.5.3 Center Estimation.

Despite every effort to align the sample and detector centers, persistent precision alignment is not possible. The center of the ACAR distribution will shift from sample to sample, so the center needs to be identified for each spectrum. KRUSEMAN notes that the center of a distribution will even shift over time of counting for a single sample, an effect he attributes to the heating of system electronics [57]. In order to perform the symmetry-folding operations explained in the next section, identifying a well-defined center is required. Fortunately, methods are available to correct for any offset in the ACAR spectra.

Two algorithms exist for identifying the center of the ACAR distribution, one using anisotropy and the other using a chi-squared test. The earliest method to determine the center of an ACAR distribution was identified with the aid of anisotropy plots [89]. WEST notes that an ACAR plot should possess reflective symmetry over two orthogonal axes, with the origin denoting the center. An anisotropic plot, generated by subtracting a representative isotropic contribution, will enhance such anisotropic features [73]. In 1990, SMEDSKJAER & LEGNINI introduced the chi-squared method, testing an ACAR spectra for C_2 symmetry to identify the center [79]. KRUSEMAN describes the chi-squared double summation given in Equation 58. An ACAR distribution, $n(k,l)$, is rotated by π to transform into $n'(k,l)$, and then compared with itself. The center is then adjusted under chi-squared is minimized [57, 79].

$$\chi^2 = \sum_k \sum_l \frac{\left(n'(k,l) - n(k,l)\right)^2}{n(k,l)} \tag{58}$$

SMEDSKJAER suggested χ^2-values less than 0.03 were acceptable, indicating instrument artifacts less than 17 % of the standard deviation of the binned data [79]. Table 5 compares the χ^2-values for the samples processed in this research.

Table 5. χ^2 Metric of Fit. Assess the goodness-of-fit of the center determined for each data set. The analysis focused on the range -5.0 to $5.0\,[10^{-3}\,\mathrm{m_e c}]$, with $1.0\,[10^{-3}\,\mathrm{m_e c}]$ bins.

Sample	χ^2-Value
Cu	0.0049
LTB	0.0103
LTB-Ag	0.0047
LTB-Cu	0.0384
ZnS-Ag	0.0376

4.5.4 Symmetry Folding.

Once a spectra is properly centered, a folding operation can exploit symmetry to improve statistical variation. In addition to the reflective symmetry and C_2 rotational symmetry discussed above, the ACAR spectra should possess the symmetry of the sample.

A single-crystal sample will possess symmetries about certain points and axes. The momentum samples collected via ACAR, while in reciprocal space, also possesses the same symmetries. For example, a body-centered cubic lattice, such as a copper single-crystal will exhibit C_4 symmetry about the [100] axis. The momentum distribution will exhibit the same C_4 symmetry about the [100] axis in momentum space. The collected spectra is then rotated or reflected based on the crystal symmetry, and then overlaid on itself. If the center was appropriately chosen, and artifact contribution is low, the superimposed spectra will constructively reinforce desired features.

V. Results and Discussion

In this research, a new method for processing data on the AFIT 3D spectrometer was developed, as well as the incorporation of a slow positron beam to serve as a new positron source. The data processing includes a new interpolation method to determine gamma interaction positions on each HPGe DSSD, implements a MSF-based data correction scheme, and explores statistical improvements by leveraging crystal symmetries. Emphasis is placed in this chapter on demonstrating the unique ability of the 3D-PASS to filter the data set to isolate and study particular features present.

The existing data sets from the target materials of previous 3D-PASS studies were re-evaluated, and are presented in this chapter. A demonstration of the improvements will be made comparing the original results with the new processing. The chapter begins with the reevaluation of JIMÉNEZ's copper standard source (Cu) data [52]. Analysis continues discussing lithium tetraborate ($Li_2B_4O_7$ or LTB) bulk PAS data previously collected on the 3D spectrometer by FAGAN-KELLY [32]. The spectra of a third material of interest, silver-doped zinc sulfide (ZnS−Ag), was collected during this research using the slow beam as a positron source.

5.1 Interpolation Improvements

Two specific improvements were made to the interpolation scheme used on AFIT's 3D-PASS. First, the method presented by WILLIAMS was adjusted to eliminate the squeezing effect noted by STEVENSON. These improvements to position accuracy were presented in Section 3.3.1. Second, the new interpolation scheme includes interactions that occur in the gaps between collection strips, which share charge collection.

Coincident charge sharing events adds a significant number of counts to the available data, presented in Table 6. Each target material in the table includes the original count and collection time reported, with a calculated rate, before reporting the count attained using the new algorithm. For example, with twice as many counts, the standard deviation reduces by about 30 %. WILLIAMS' data was unavailable, but for comparison, he reported a collection of 1.12×10^6 counts over a day (86 400 s), a rate of 46 667 counts per hour, possible due to his high activity 106.5 mCi ^{22}Na source [91].

Table 6. Improved coincident counts by including charge sharing.

Sample	Time [Hr]	Count	Rate [/hr]	New Count	New Rate [/hr]
Cu	408	37 516	92	95 270	234
LTB	276	17 380	63	47 396	172
LTB-Ag	290	12 722	44	72 221	249
LTB-Cu	312.5	5 913	19	10 190	33
ZnS-Ag	80	– —	—	18 141	227

5.2 MSF Improvements

Periodic efficiencies on the detector faces impacts the MSF of the spectrometer. As noted in Section 4.5.2, the data processed by JIMÉNEZ and FAGAN-KELLY suffered sampling issues due to symmetry in the spectrometer. Figure 29 depicts the sampling deficiency that occurred at 2.5 mrad intervals in their detector configuration. Early in the current research, Detector 0 was moved to a distance of 2500 mm to create an asymmetry to resolve this issue based on JIMÉNEZ's copper data, and the existing interpolation method.

During the course of this research, the implementation of the new interpolation method softened the severity of the periodic efficiency across the detector face. Figure 30 compares the resulting MSF of JIMÉNEZ's symmetric setup, to the new asymmetric

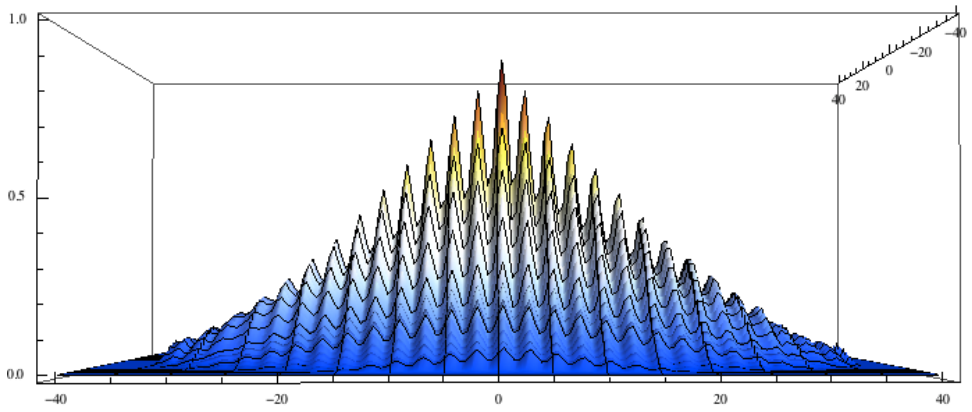

Figure 29. MSF Profile for Prior System Configuration. Calculated using Cu-Doped LTB data collected by FAGAN-KELLY. Note: Periodic peak efficiencies occur at integer multiples of 2.5 mrad [32].

setup when the new interpolation method is applied. The left side of Figure 30 shows the improvement in sampling due to the new interpolation scheme compared to the original scheme represented in Figure 29. While the offset represented on the right side of Figure 30 further improved the smoothness of the MSF, the improved sampling comes at the cost of efficiency. Due to the interpolation improvements, a reduced distance can be implemented by future researchers to regain some efficiency lost.

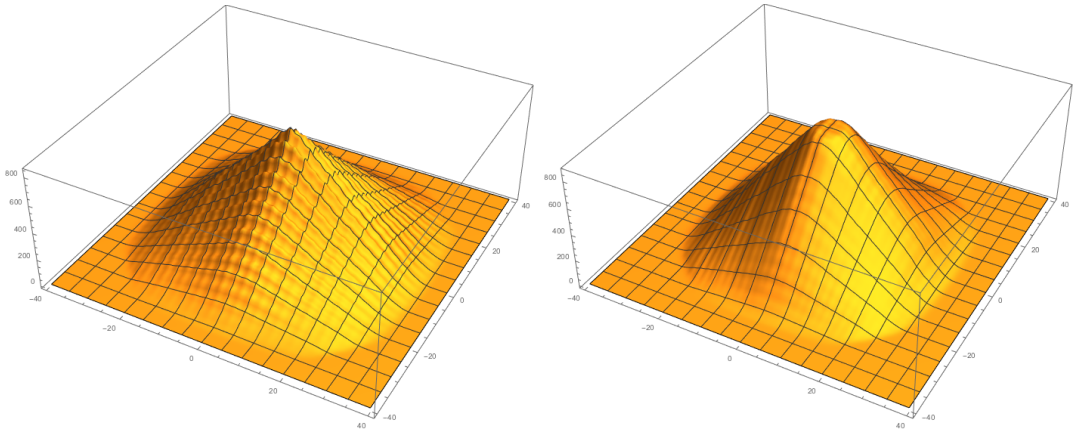

Figure 30. Comparison of MSF for Configurations. Images represent processing using the interpolation technique developed in this study. Data from JIMÉNEZ and FAGAN-KELLY used an MSF from a symmetric system (Left), while the asymmetric configuration collected ZnS-Ag data (Right).

The efficiency for coincident events are related to the solid angle of the detector placed further away. The system is optimized for collection efficiency when the two detectors are placed equidistant at 2000 mm, and will be referenced in this paragraph as 100 %. When the furthest detector is placed at 2500 mm, the configuration of the system for the ZnS collection, only 64 % of the coincident gammas can be collected relative to the equidistant (2000 mm) configuration. This offset distance was determined before the new interpolation technique was implemented, and the detectors responded with areas of very low, periodic efficiency. The new recommended distance is to place one detector at 2300 mm, represented on the right side of Figure 31. This represents an offset of 15 %, as recommended by WEST and as discussed in section 4.5. This new detector distance would increase the data collection rate from 64 to 75 % of the equidistant configuration, while maintaing a smooth momentum sampling. A less asymmetric option of 2200 mm is presented for comparison on the left side of Figure 31, which presents some undesirable rippling.

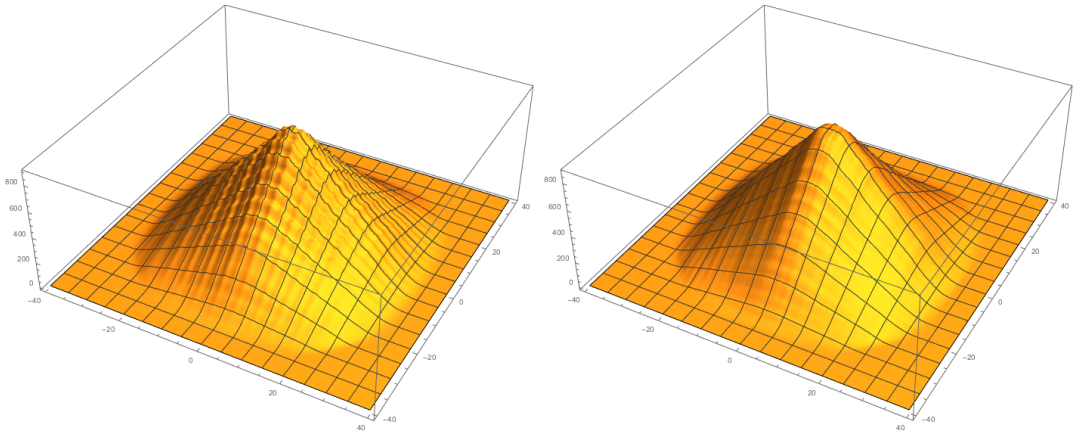

Figure 31. Comparison of MSF for Potential Configurations. Detector 1 is placed at 2000 mm in both configurations. Left: Detector 0 at 2200 mm. Right: Detector 0 at 2300 mm.

5.3 Copper Standard Source

JIMÉNEZ collected coincident ACAR and DBAR measurements using a sandwiched copper sample. The sample consisted of two 10 mm x 10 mm x 0.4 mm squares of single-crystal copper with a layer of carrier free ^{22}Na at an activity of about 22.3 µCi evaporated between [52]. This resulted in an efficient use of positrons, and the most coincident counts compared to collections since. JIMÉNEZ's ACAR results are reprinted on the left of Figure 32 for comparison with the new unweighted results on the right of Figure 32.

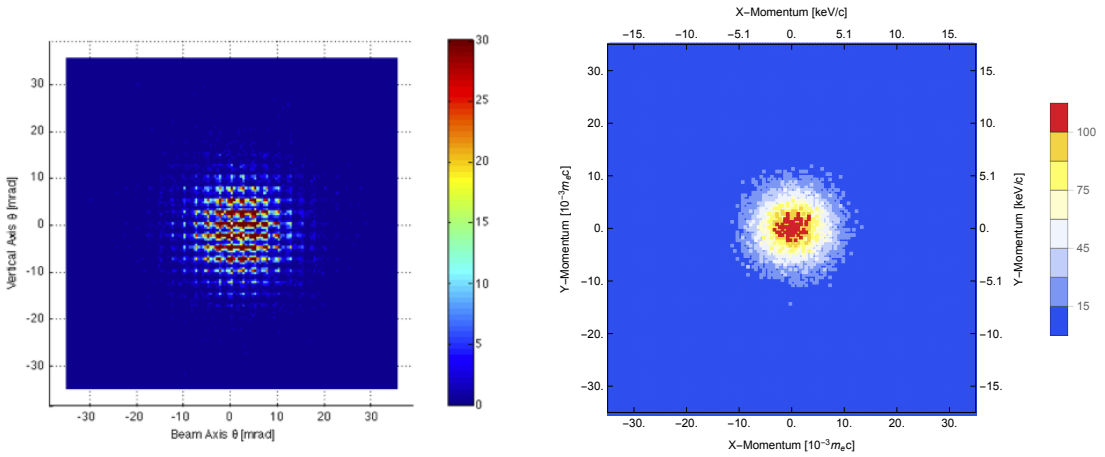

Figure 32. Unweighted Copper ACAR Results. Left: As reported by JIMÉNEZ[52]. Right: Using processing developed in this study.

JIMÉNEZ's ACAR spectra suffered from pixelation due to very low, periodic counting efficiencies at the edges of detector contact strips. The ACAR spectra on the right, even before applying correction techniques, avoided this issue with the improved position estimation.

In addition to momenta information acquired using ACAR, DBAR measurements are taken, with each data point correlated with the ACAR measurement. Figure 33 presents the 2D-DBAR from both JIMÉNEZ (Left) and the current research (Right).

Both spectra show collected data with incomplete charge collection, the horizontal and vertical column features on each plot about 511 keV. Very few data points exhibit pile-up behavior, data appearing toward the top or to the right on the plot, which is the result of multiple interactions in the detector. Unfortunately, incomplete charge collection and pileup contribute misrepresentations of 3D momentum data. Filtering these data points reduces the noise contribution. The acceptance criteria is that the sum of the collected gamma energy should be about equal to the combined rest mass of the electron and positron, or $E_0 + E_1 = 2m_e c^2 \pm 2\,\text{keV}$. Figure 34 shows DBAR data before and after filtering.

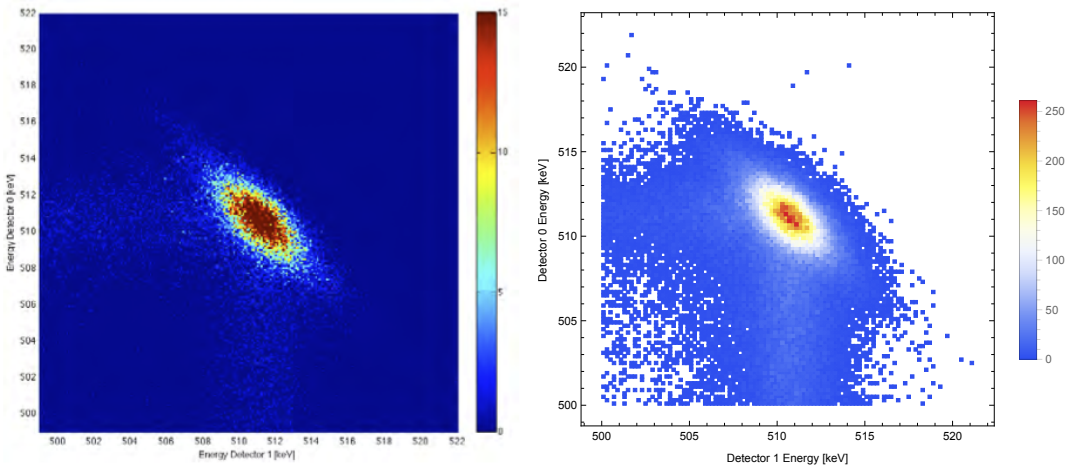

Figure 33. Unweighted Copper Results. Left: As reported by JIMÉNEZ[52]. Right: Calculated in this study.

The detectors may collect the full energy of some annihilation events that do not meet the acceptance criteria. The acceptance criteria assumes negligible binding energy, as discussed in Section 2.1. The binding energy of conduction and valence electrons in copper range up to the tens of electron-volts. The weakest bound core electrons range from tens of electron-volts to thousands of electron-volts. When the binding energy of a core electron is above about 1 keV, it has the potential of being filtered from the data set. For core electrons, which possess higher binding energies,

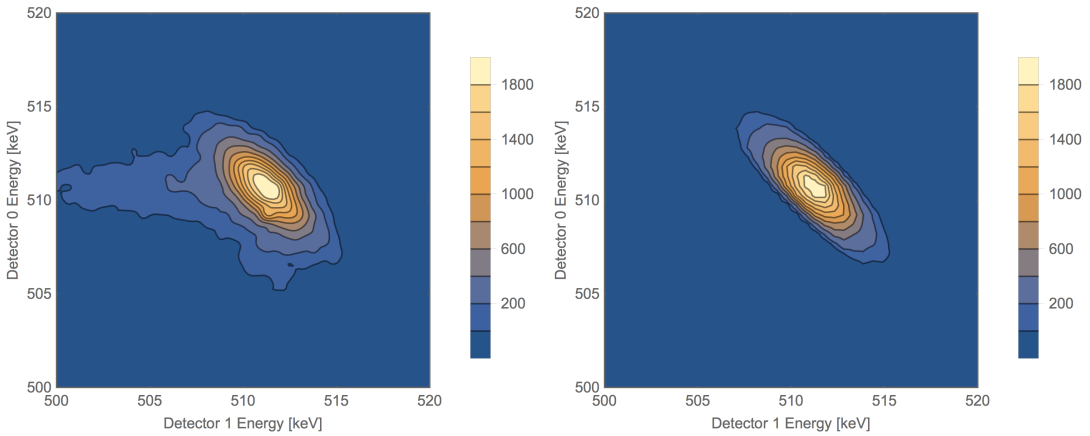

Figure 34. Weighted Copper DBARResults. Left: DBAR spectrum weighted by MSF Correction Matrix. Right: DBAR spectrum Weighted and Filtered.

the probability of annihilation becomes vanishingly small. For copper, the binding energy for $3p$ and $3s$ electrons are on the order 100 eV, while the $2s$ and $2p$ electrons have binding energies on the order of 1 keV. The probability of annihilation with these more tightly bound electrons is collectively only 0.1 % [68]. In a data collection of 100 thousand samples, only 100 data points would be expected to belong to $2s$ or $2p$ orbitals, and may only contribute one or two counts to a particular bin. From Figure 35 it is apparent that without filtering out incomplete charge collections, the distribution will include apparent high-momentum components out to 30 keV.

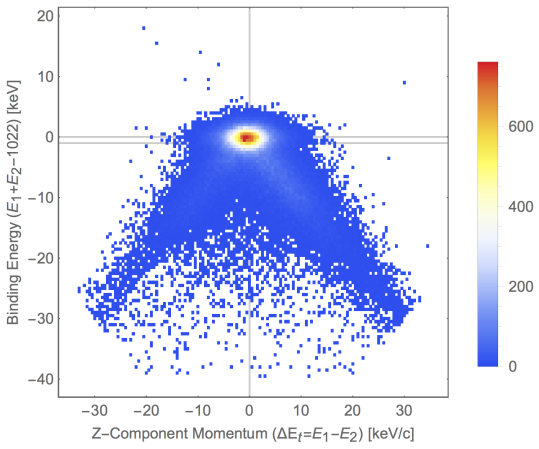

Figure 35. Binding Energy versus Doppler Broadening for Copper Sample.

After the 3D momentum data is filtered, the correction matrix is applied and the spectrum is folded according to expected symmetry. As mentioned in Sections 4.5.3 and 4.5.4, an ACAR spectra is expected to have at least C_2 symmetry. The left of Figure 36 shows an ACAR plot exploiting C_2 symmetry. The 3D nature of the data collected on the 3D-PASS allows for symmetry operations on the data set that are not possible on traditional ACAR spectrometers. A single-crystal material may have a dozen or more points or axes on which a symmetry operation may be applied. The right of Figure 36 shows an ACAR plot where C_2 symmetry operations have been applied along all three principle axes.

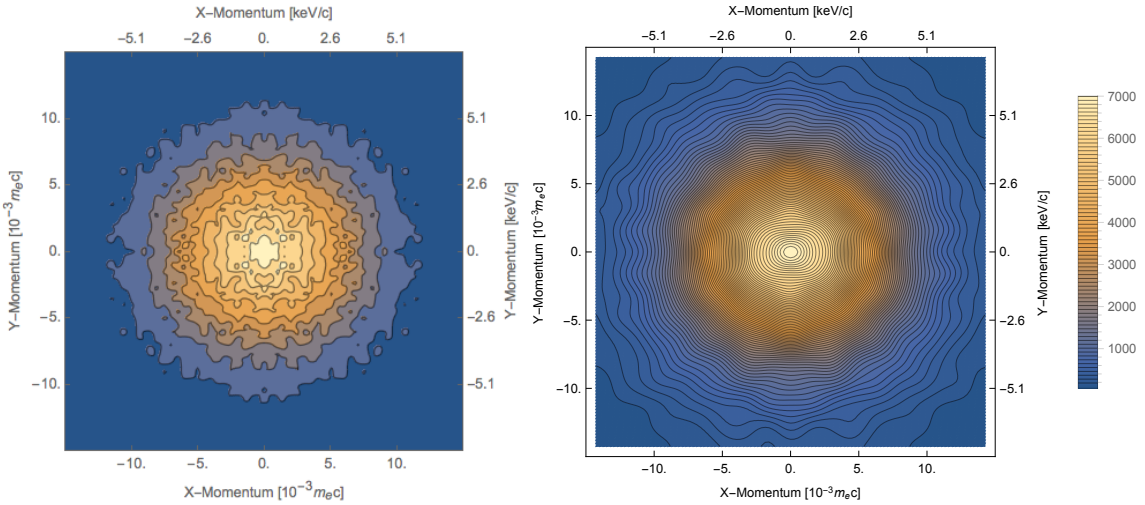

Figure 36. Copper ACAR with Symmetry Folding. Left: ACAR Spectrum Featuring C_2 Folding About the Z-axis. Right: ACAR Spectrum Featuring C_2 Folding About the X, Y, and Z-Component Axes.

Oriented single-crystal materials allow the experimenter to leverage crystal symmetry if mounted along an axis of symmetry. The surface of JIMÉNEZ's copper sample contained the (100) crystal plane. The orientation of the [010] and [001] directions could have fallen in any direction along the (100) plane. JIMÉNEZ mounted the copper sample at a 45° angle with respect to the detector axis, to mimic the data taken

by WILLIAMS. However, without knowing the orientation of the plane, the integration plane, the crystal plane parallel to the detectors, could not be known after the rotation [52, 91].

Since the AFIT 3D-PASS uniquely records all three momentum components, an integration over the [100] direction was completed. After calculating the momentum, the data points were extracted in the form $\{p_x, p_y, p_z\}$. The list of data points were rotated 45° about the negative x-axis, and a momentum plot was created integrating over the [100] direction. Strictly speaking, Figure 37 is not an ACAR plot, but it is an integration of the 3D data over the [100] direction. This is the first demonstration of generating a 2D momentum spectra integrated over a direction other than the mounted ACAR direction, a feature unique to the AFIT 3D-PASS. The generated spectrum agrees well with the theoretical spectra generated by HAGHGOOIE displayed on the right side of Figure 37 [44].

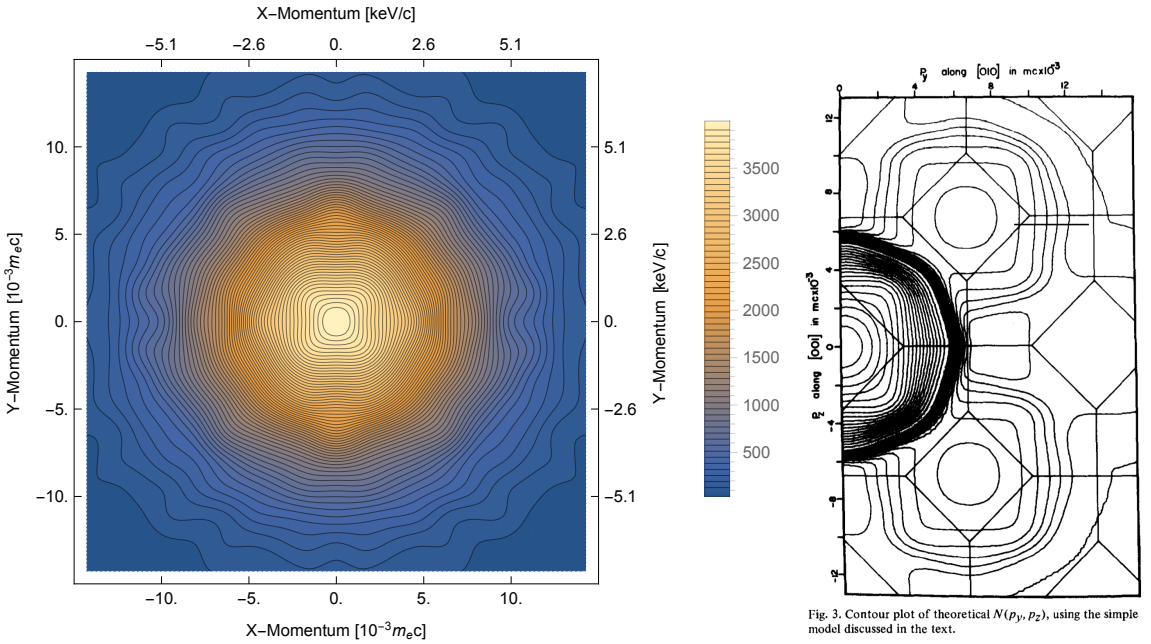

Figure 37. Copper (100) Plane Momentum Measurement. Left: Experimental Results. Right: Theoretical Expectation Using Independent Particle Model From HAGHGOOIE [44].

Reconstruction of the 3D electron momentum distribution using ACAR requires the collection of multiple projections. Since AFIT's 3D-PASS collects 3D momentum components simultaneously, an iso-surface can be generated with a single collection. Figure 38 is an iso-surface representation of the fermi surface of copper using a single collection on the AFIT 3D-PASS. The density iso-surface was chosen to display the neck features from the L-points in copper's first Brillouin zone.

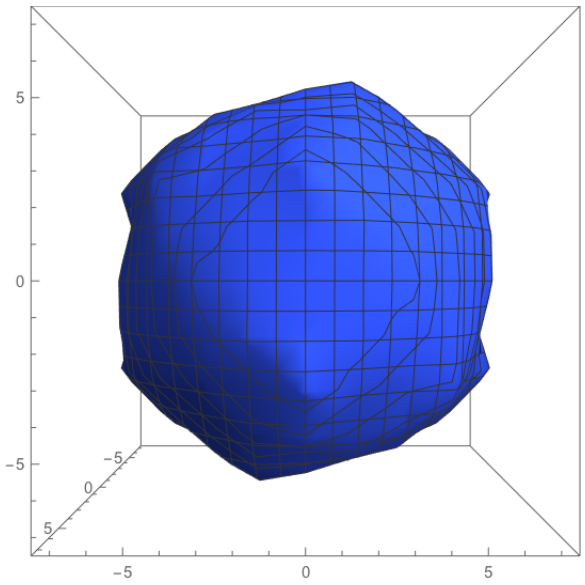

Figure 38. 3D perspective of Copper Fermi Surface. The protrusions correspond to the neck features at L-Points on the Surface of the First Brillouin Zone.

The resolution of the Figure 38 is low due to lack of counts. For example, given a 10×10 matrix of 1 mrad momentum bins, 10 000 counts would be required if each bin contained 100 counts. A similar 3D collection would require an order of magnitude more counts to maintain the same statistical uncertainty in each voxel.

Another advantage of correlated 3D data is the ability to filter ACAR or DBAR derived momentum data based on desired features observed in either data set. This ability was demonstrated earlier when the 3D data set was filtered to only data meet-

ing DBAR acceptance criteria. WILLIAMS used this capability to plot DBAR spectra corresponding only to selected ACAR features. This capability can be used to compare data subsets to the whole.

For example, the magnitude of the momentum vector can be determined using Equation 59. The momentum magnitude in turn is related to the fermi energy of free electrons, most applicable to simple metals, as represented in Equation 60 [61]. Figure 39 compares the momentum magnitude before and after the DBAR filtering step. The inclusion to incomplete charge collection would greatly broaden the perceived momentum distribution in the z-component.

$$p_{mag} = \sqrt{p_x^2 + p_z^2 + p_z^2} \tag{59}$$

$$2m\varepsilon_f = p_x^2 + p_z^2 + p_z^2 \tag{60}$$

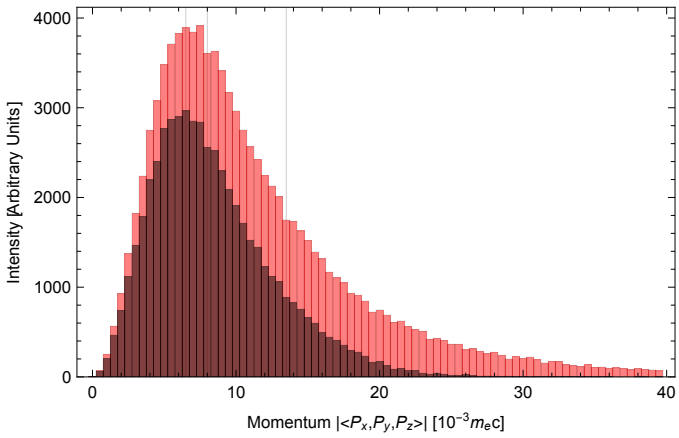

Figure 39. Copper Momentum Magnitude Distribution. Light Red: Distribution as Collected. Dark Red: Distribution After Filtering.

Using the peak value of the distribution (6.25 mrad, or 3.19 keV), the fermi energy (ε_f) of copper is estimated to be 9.9 eV, a little larger than the accepted value of 7.0 eV.

5.4 Lithium Tetraborate

Stefan FAGAN-KELLY, in his master's thesis, collected coincident ACAR and DBAR measurements using doped and undoped samples of hydrothermally grown lithium tetraborate. A shielded sample of ^{22}Na served as the positron source. All samples were oriented with their crystal faces placed 45° to the detector axis, the same orientation of the copper sample described in the previous section [32].

LTB has a band gap that ranges, depending on crystal orientation of 8.9 eV to 10.1 eV [93].

Figure 40 depicts the band structure of bulk LTB.

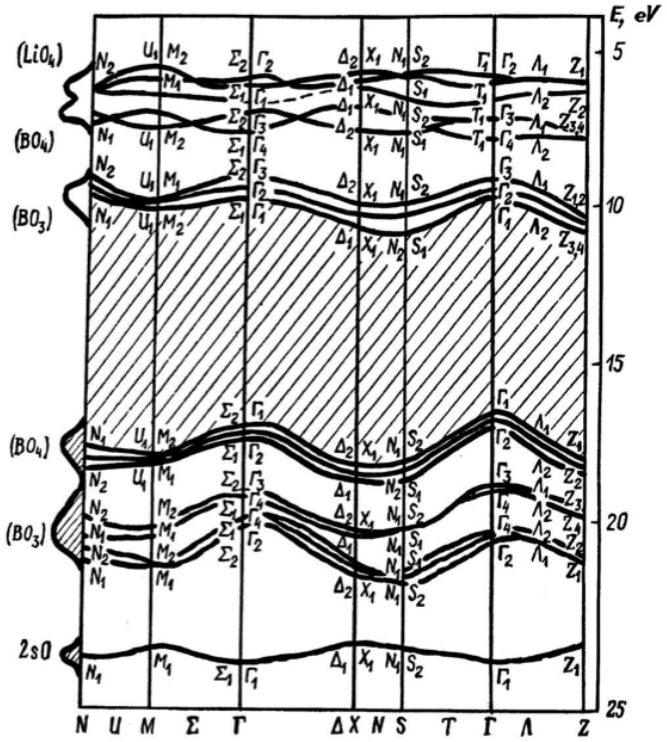

Figure 40. The Calculated Electronic Bulk Band Structure of Lithium Tetraborate [1].

5.4.1 Undoped Lithium Tetraborate.

FAGAN-KELLY's first sample was a virgin sample to be compared with the doped samples. He reported that the undoped LTB crystal was cut along the (001) plane [32]. FAGAN-KELLY's reported ACAR spectra suffered from the same pixelation issues as JIMÉNEZ, and is depicted in Figure 41.

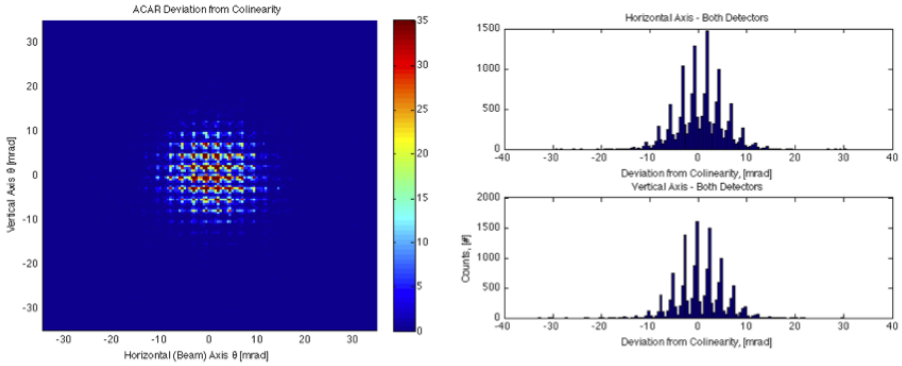

Figure 41. LTB ACAR Results As Presented By FAGAN-KELLY[32].

The same process described to extract the copper data was applied to LTB samples. Figure 46 shows the momentum across the (001) plane after applying symmetry operations. The [001] direction has C_{2v} symmetry, so only C_2 symmetry was applied to the data set [93]. The first Brillouin zone is visible, with the k_y basis vector vertical, as compared to Figure 43.

Figure 44 depicts the electron momentum magnitude distribution. Applying equation 60, using the peak value of 6.25 mrad (9.9 keV). The Fermi energy would be in the band gap depicted between 10 to 17 eV. WOOTEN notes the Fermi level will be closer to the conduction band in the presence of oxygen vacancies. [93].

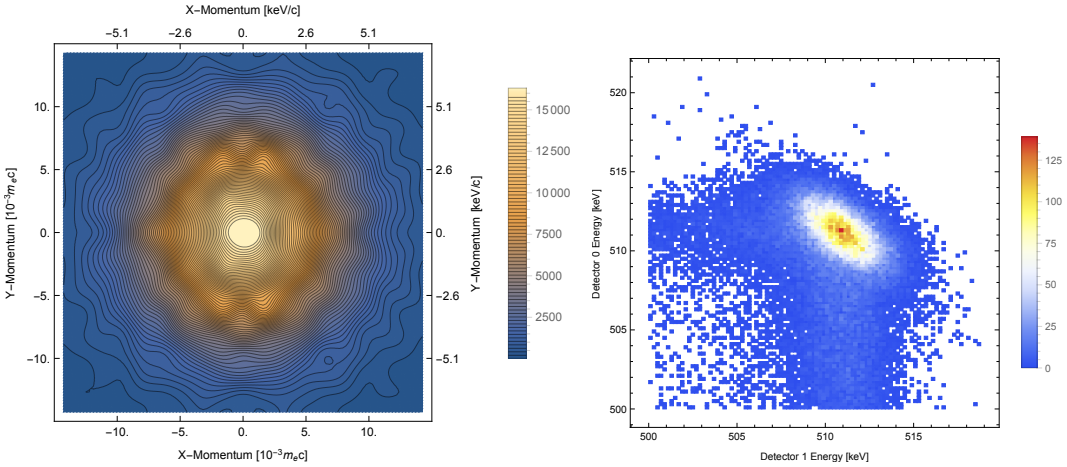

Figure 42. LTB Spectra Produced Using Processing Developed In This Work. Left: 2D Momentum Spectra over (001). Right: DBAR spectra before data filtering.

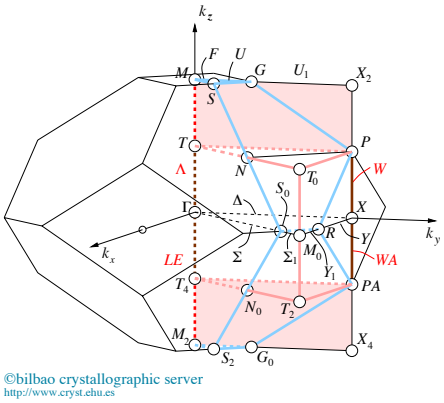

Figure 43. LTB First Brillouin Zone [5, 86].

5.4.2 Silver-Doped Lithium Tetraborate.

FAGAN-KELLY did not describe the orientation of the Ag-doped LTB crystal. He did report that the LTB-Ag crystal was x-ray irradiated, introducing trapped charges, and turning the crystal green. The 2D momentum spectra is depicted in Figure 45.

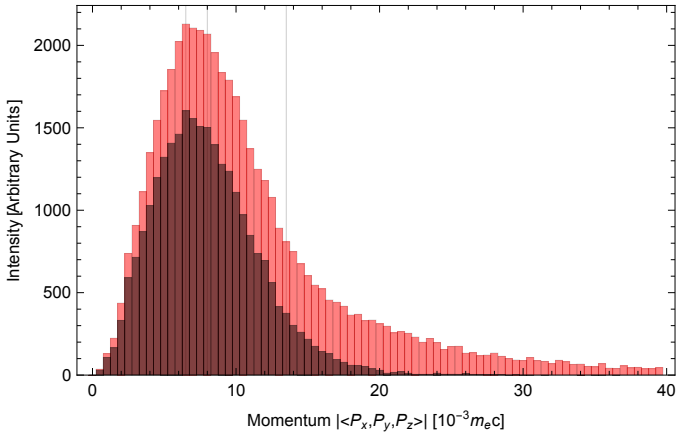

Figure 44. Silver-Doped LTB Momentum. Peak at 5.8 mrad**, and Mean at** 8.0 mrad (4.1 keV)**.**

5.4.3 Copper-Doped Lithium Tetraborate.

FAGAN-KELLY's copper-doped LTB had a low count rate due to a combination of the sample's small size, and misalignment in the chamber. As with the silver-doped LTB sample, FAGAN-KELLY did not report the orientation of the Cu-doped LTB crystal.

5.4.4 Comparison of Lithium Tetraborate Samples.

A common method of data analysis for DBAR spectra is the calculation of parameters based on the distribution lineshape. The percent of counts in the center of the spectra to describe a 'shape' (S) parameter, while the proportion found in the 'wings' of the spectra define the second (W) parameter.

The S and W parameters relay information about the concentration of vacancy defects in a material. The center of the distribution represents low-momentum events, which are associated with annihilations in the conduction and valence band. The wing parameters represent high momentum events, and are associated with the annihilation of core electrons. When a material possesses a higher concentration of vacancy defects, the positrons tend to find these defect sites. This increases annihilations with

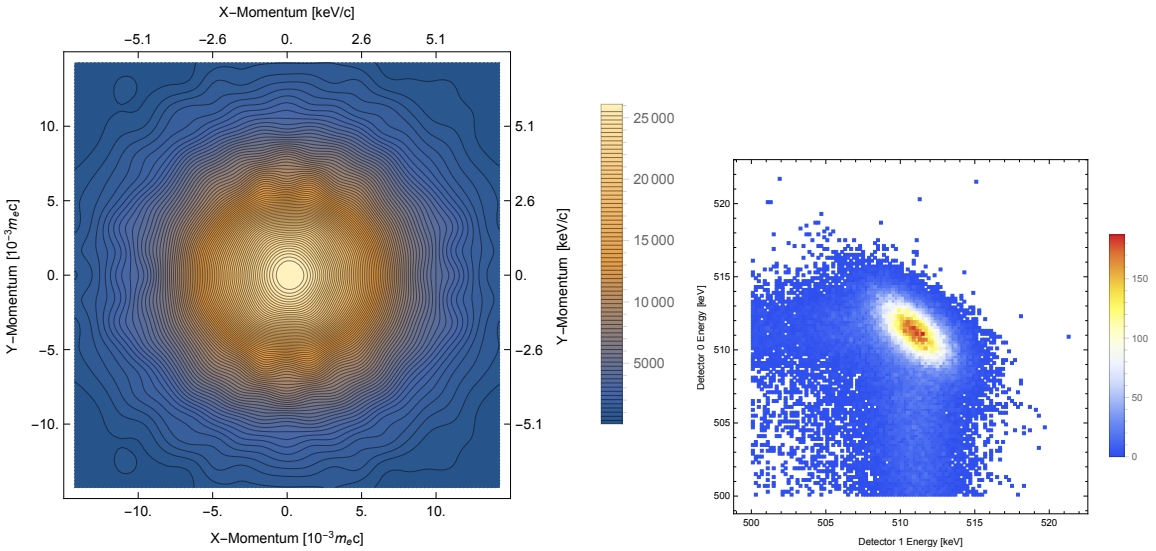

Figure 45. Silver-Doped LTB Results. Left: Symmetry folded spectra. Right: DBAR. The shaded region represents momentum distribution after energy filtering.

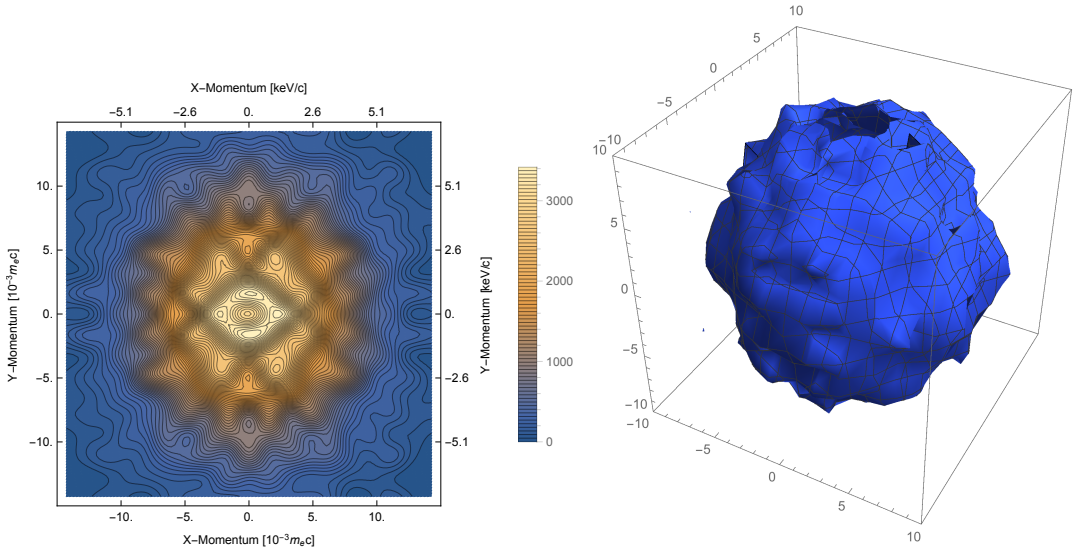

Figure 46. Cu-Doped LTB Results. Left: 2D momentum density spectra. Right: 3D momentum density spectra.

valence electrons, and decreases core electron annihilations. As a result, the DBAR spectra narrows, increasing the S-parameter, and decreasing the W-parameter. This analysis technique is useful for comparing the concentration of defects in virgin and

damaged materials. Since positrons are excellent at sampling negatively charged defects, such as void and vacancy defects, this technique is beneficial even at low defect concentrations [55].

The line shapes of all three crystals are drawn in Figure 47. A summary of all parameter values is in Table 7. Two doped LTB crystals are compared to an undoped reference crystal. The DBAR spectra of two sets of data in a series for comparing the sharpness and wing lineshape parameters.

Table 7. Line Shape Parameter Summary.

Sample	Shape (S)	Wing (W)	S/S_{ref}	W/W_{ref}
LTB	0.5449	0.2487	1.0000	1.0000
LTB-Ag	0.5370	0.2573	0.9856	1.0346
LTB-Cu	0.5502	0.2427	1.0098	0.9758

Line shape parameter analysis is also common when comparing surface and bulk properties. This technique will be useful as AFIT further develops studies in surface science.

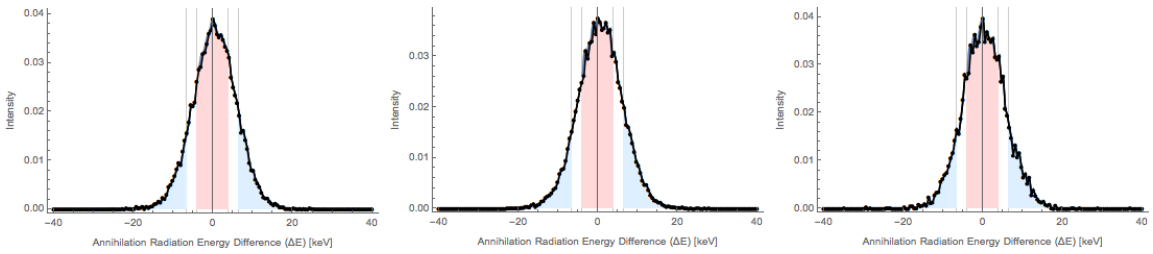

Figure 47. Lineshape Parameters for Doped LTB Crystals. The red area encloses the area for the 'sharpness' parameter, while the blue area encloses the area for the 'wing' parameter. Left: Undoped Reference Crystal. Middle: Silver-Doped Crystal. Right: Copper-Doped Crystal.

5.5 Silver-Doped Zinc Sulfide

A key goal of this research was to combine a cold positron beam with the three dimensional spectrometer. A silver-doped zinc sulfide (ZnS−Ag) screen was used to image the beam spot (see Section 3.2.4) and as a target material of opportunity to demonstrate correlated ACAR and DBAR with the positron beam. The screen consisted of ZnS-Ag powder, along with a binder, on a stainless steel backing.

The ZnS-Ag screen was mounted onto an electrically isolated rotating manipulator arm. The screen was positioned rotated about 45° about the y-axis so that the beam spot would have the same size projection along the x-axis as found on the y-axis. The intention was to reduce the resolution along the x-direction so that it was roughly equivalent to the y-direction.

While the positrons used for the preceding target materials used positrons from ^{22}Na, the positrons incident on the ZnS-Ag sample were neon-moderated in the RGM before being accelerated to the ZnS-Ag screen by applying a 8 kV bias directly to the screen. The beam trap was not used due to a malfunction.

Originally, a quartz sample was to be used. However, there was an uncertainty about the position of the beam, which require imaging. Using the screen as a sample material allowed for imaging the beam between data files.

Since the ZnS-Ag is a powder in binding, there is no crystal symmetry to exploit. The expected C_2 ACAR symmetry still applied, and that fact was used to generate Figure 48.

On the left of Figure 48 is a 2D momentum plot for silver doped ZnS, with the data rotated as if the screen had been facing the detector axis directly. While the distribution was expected to be isotropic due to an assumed random arrangement of ZnS power in the binding, the result does not appear isotropic.

The momentum distribution on the right in Figure 48 is displayed without the unfiltered distribution. The peak of the distribution is found at 6.25 mrad (3.19 keV), with a mean at 11.37 mrad (5.81 keV), corresponding to electron energies of 9.9 eV and 16.3 eV, respectively. Neither value is in particularly good agreement with 12.46 eV [82]. This is to be expected as ZnS is a wide band gap semiconductor, and the fermi energy would fall within the gap. A gridline is placed at 6.98 mrad to represent a Fermi energy of 12.46 eV, as well as two more at 5.08 mrad and 8.88 mrad to represent a band gap of 3.8 eV centered on the Fermi energy [82].

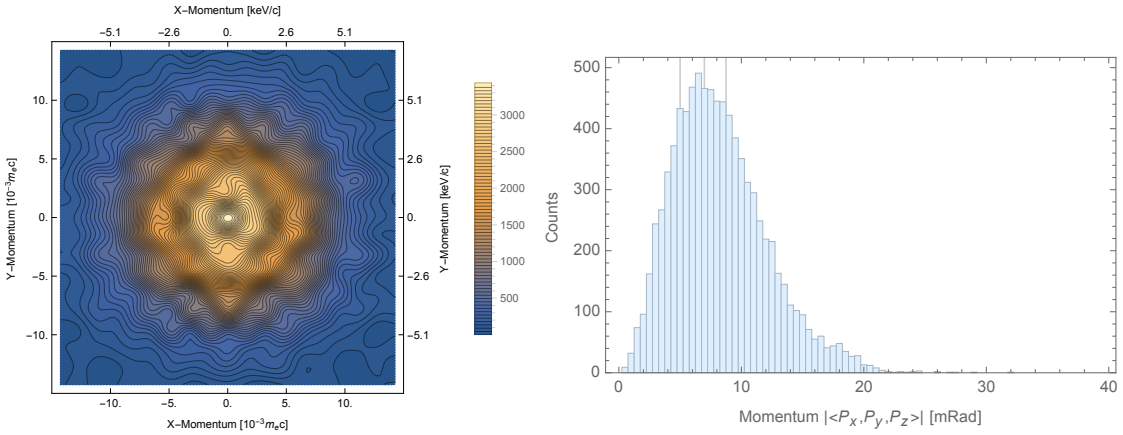

Figure 48. Silver-Doped ZnS Results. Left: 2D Momentum Distribution. Right: Momentum magnitude distribution after energy filtering.

VI. Conclusions and Suggestions for Future Work

In this research, the three dimensional electron momentum distribution was extracted for five target materials, including: a copper single-crystal, single-crystal lithium tetraborate, silver-doped single-crystal lithium tetraborate, copper-doped single-crystal lithium tetraborate, and a silver-doped zinc sulfide screen. Additionally, a low-energy positron beam was integrated with the AFIT 3D-PASS. Most significantly, processing of spectrometer data was re-engineered to improve estimation of gamma-interaction position, include interaction between collection strips, include improved correction, and improve statistical variation through use to symmetrical folding.

6.1 Suggestions for Future Work

Significant time can pass between research studies focussed on positron projects. A dedicated post-doctorate researcher is suggested to advance the lab without losing continuity. Such faculty would serve as a mentor for future research students. Additionally, the beam and spectrometer equipment require periodic maintenance that is best accomplished with regular attention. The remaining suggestions are split into advancements with the hardware, and further processing improvements.

6.1.1 Equipment Augmentation.

Improving the transport of the positrons in the beam is a priority before experiments that exploit the low-energy beam can begin. The first priority is to repair the beam tube of the RGM. During setup, a short in the beam tube was found preventing a suitable magnetic field from being setup over the whole tube length. This issue was compounded when a loss of cooling caused overheating in the beam tube.

Two of the advantages of having a low-energy positron beam are having a source of positrons cold enough to explore Feshbach vibrational resonances, and having a monoenergetic source of positrons. However, adding instrumentation to better measure and control the energy of the positron beam will be necessary to further exploit the capability. A simple accelerator can be fabricated to control accelerating the positrons and thus whether the measurement samples the bulk or near surface of the sample. Additionally, a retarding field analyzer (RFA), also known as a retarding potential analyzer (RPA), can be used to characterize the energy of the beam.

One of the major research areas at AFIT is the effects of radiation on electronic materials. Positron annihilation spectroscopy techniques have been successful in the past with determining the concentration of negatively charge defects by using a combination of DBAR and PALS measurements. Since DBAR measurements are already accomplished using the 3D-PASS, the addition of a PALS system would increase the capability of the laboratory.

6.1.2 Further Processing Improvements.

Lock-Crisp-West (LCW) folding, named after the authors of the 1973 paper suggesting the practice, is an important method of folding the ACAR spectrum. Wavevectors outside of the first Brillouin zone are folded back into the first zone, emphasizing Fermi surface features. By summing the contribution over all zones on top of each other, the structure of the partially filled zones is reinforced, denoting the location of the Fermi surface. [59, 70]. The summation represents the total number of occupied states over all Brillouin zones, unoccupied outside of the Fermi surface, and fully occupied within. The discontinuity marks the Fermi surface. In literature, LCW folding is applied to 2D-ACAR spectra, and implementing a 3D LCW folding for 3D-PASS data should not be overlooked.

Further improvements to calculating the position of incident radiation may be possible considering the depth of radiation interaction. BURK observes that the induced charge is a function of the depth of interaction in the crystal [16]. In particular, the induced signal is bipolar for interactions less than 3 mm from the detector surface, which HAYWARD notes degrades the resolution of lateral position [45].

Appendix A. Momentum Sampling Function Algorithm

The Momentum Sampling Function (MSF) described by KRUSEMAN [57] and WEST [89] is continuous. However, ACAR data is binned, so the MSF double integral needs to be discretized in order to calculate correction values.

A.1 Algorithm Development

WEST presents the MSF as the double integral in Equation 61. Looking at Equation 61, one can see that the MSF at a particular deviation from collinearity (θ, ϕ), is the summation of the combined efficiency at all points on the detector faces $(\varepsilon_{1ij} \times \varepsilon_{2kl})$ that form this angle.

$$c(\theta, \phi) = \iint d\bar{\theta}\, d\bar{\phi}\, \varepsilon_1(\bar{\theta} + \theta/2; \bar{\phi} + \phi/2)\, \varepsilon_2(\bar{\theta} - \theta/2; \bar{\phi} - \phi/2) \tag{61}$$

KRUSEMAN presents the MSF as the double integral in Equation 62. This notation emphasizes that the MSF samples momentum, and shifts the deviation angle so that it is reflected only on one detector during the calculation. This representation inspired the approach below to shift equation 61 similarly, keeping the position on one detector constant, while performing computations over the other detector face.

$$c(p_x, p_y) = \iint d\bar{p_x}\, d\bar{p_y}\, \varepsilon_1(p_x - \bar{p_x}; p_y - \bar{p_y})\, \varepsilon_2(\bar{p_x}; \bar{p_y}) \tag{62}$$

Considering that each MSF bin has a fixed width and height, corresponding to a fixed change in angle, $d\theta$ and $d\phi$ becomes $\Delta\theta$ and $\Delta\phi$, respectively, depicted in Equation 63. Since the MSF will be scaled relative to its peak at the end, and the $\Delta\theta\, \Delta\phi$ term is constant through the calculation, it can be considered just part of the

scaling, and does not need to be included in the computation, leaving equation 64.

$$c(\theta,\phi) = \Delta\theta\,\Delta\phi \sum_{\bar{\theta}} \sum_{\bar{\phi}} \varepsilon_1(\theta-\bar{\theta};\phi-\bar{\phi})\,\varepsilon_2(\bar{\theta};\bar{\phi}) \tag{63}$$

$$c(\theta,\phi) = \sum_{\bar{\theta}} \sum_{\bar{\phi}} \varepsilon_1(\theta-\bar{\theta};\phi-\bar{\phi})\,\varepsilon_2(\bar{\theta};\bar{\phi}) \tag{64}$$

The implementation used in this research to calculate the MSF attempts to minimize computation time. Instead of computing the entire MSF for each particular deviation (θ,ϕ) one-by-one, a matrix representing the contribution of a particular location bin on Detector 1 over all possible deviation angles to Detector 0 is calculated. For simplicity, this matrix is referred to as a slice of the MSF. The process is repeated until a slice is created for every location bin in Detector 1. Since each slice calculation is independent, processing time is reduced by performing the operation in parallel. A complete MSF is produced by summing together all slices. Each element in the matrix is then divided by the maximum element value to get the final, scaled MSF.

The described approach works particularly well for identical detectors placed symmetrically about the target, but a problem emerges for asymmetric systems. For an asymmetric system, the angle increment formed between the source and bins on Detector 0 will differ from the angle increment formed between the source and bins on Detector 1. In order to sum over all slices of the MSF, each slice must be the same dimensions, with bins representing the same momentum values. The matrix representing the MSF is predetermined to contain a value range up to the maximum angle measurable, starting with a bin centered at (0,0) and incremented at a user selected resolution. The deviation from collinearity between adjacent bins on the detector efficiency matrix will not be the same as the resolution of the MSF matrix such that

two adjacent locations on the detector may contribute to the same MSF bin, and thus must be combined. To determine the contribution to a MSF slice, a mapping of pairs of locations between each detector to MSF binning is pre-calculated.

A.2 Correction Stragtegy

Once the full MSF matrix is calculated, it can be used to correct ACAR and DBAR spectra. The 3D momentum values for a collected spectra are stored as a 3-tuple list, $\langle p_x, p_y, p_z \rangle$, for which each $\langle p_x, p_y \rangle$ is represented by a bin on the MSF matrix. A weighting value for each 3D momentum is determined by locating the corresponding MSF bin, and taking the reciprocal of the MSF bin value. The value is appended to the momentum values, and a new 4-tuple list is stored as $\langle p_x, p_y, p_z, weight \rangle$.

A traditional ACAR or DBAR plot is a histogram of an integration over the 3D momentum distribution. When a plot is generated based on this weighted momentum list, a histogram bin's value is the summation of all of the weights of the points that fall into that bin. This weighting process applies even for DBAR plots, which are histograms of p_z.

Correction methods are not traditionally needed for DBAR spectra because the detector is usually placed very close to the source, so extreme momentum do not suffer decreased sampling that occurs for ACAR measurements. In this research DBAR events are correlated to ACAR events. Since higher momentum ACAR events are sampled less frequently, than any DBAR measurements correlated with higher momentum ACAR events are also sampled less frequently.

The described correction strategy will work well as long as the MSF value is constant, or changes slowly, across a bin. If the value varies greatly between adjacent bins, then there will be a large error in the correction factor. When applying corrections in such a system, interpolating between bins may mitigate large variation in correction weights.

Appendix B. Maintenance Instrumentation

Characterizing and troubleshooting the AFIT Positron Beam requires efficient instrumentation to detect annihilating positrons. The beam system hardware and software includes an input for a Transistor-Transistor Logic (TTL) compliant signal for counting 511 keV gammas. This appendix describes the equipment used to provide the diagnostic signal.

B.1 NIM Bin Setup

Nuclear Instrumentation Modules (NIM), such as a gate generator, can provide a TTL-compliant signal when provided with an appropriate trigger. The requirements for TTL compliance include a pulse between 0 V and 5.0 V. A logical `0` is represented by a low signal from 0.0 V to 0.8 V, while a logical `1` is represented with a signal voltage from 2.0 V to 5.0 V. The rise/fall time of the logic pulse should be less than 50 ns [65]. Instructions from GREAVES at FirstPoint Scientific included that the pulse width should be greater than 1.0 µs. The completed setup diagram, using NIM bins, is shown in Figure 49, with the components identified in Table 8.

The setup takes a signal from a NaI scintillating detector, and when that signal represents a gamma photon in a predetermined window about 511 keV, a logic pulse is generated. The signal pulse generated by the detector, and conditioned by the pre-amp, is proportional to the energy deposited. The window is set on the Single Channel Analyzer (SCA) by accepting pulses with peak voltages between a high and low value. The SCA requires an input signal between 0 V to 10 V, which is provided by a spectroscopy amplifier (spec amp). If the signal falls within the SCA-set window, the signal passes to a gate & delay generator, which creates the TTL-compliant logic pulse. The logic pulse is then sent to the ICU-3.

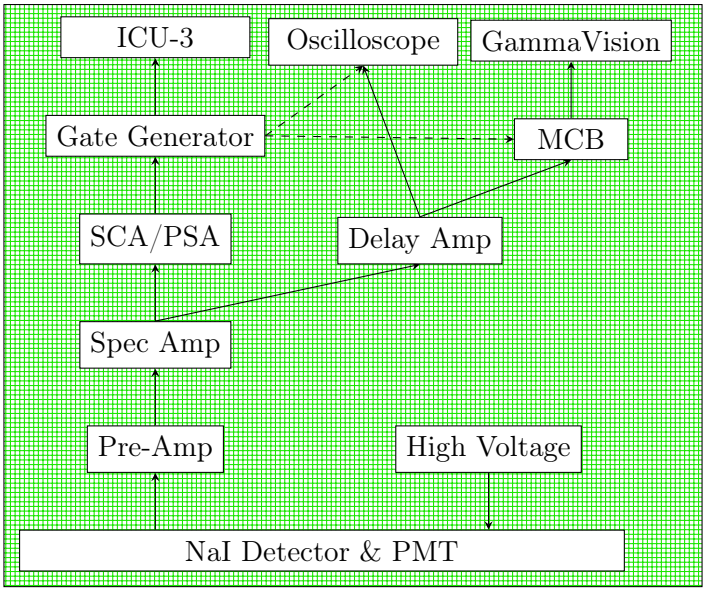

Figure 49. TTL Compliant Detector Setup. Dashed connections are optional.

Table 8. Components used.

Device	Manufacture	Model
NaI Detector	Bicron	3M3/3
PMT	ORTEC	266
High Voltage	ORTEC	556
Pre-Amp	ORTEC	113
Spec Amp	ORTEC	672
Delay Amp	ORTEC	427A
PSA/T-SCA	ORTEC	552
Gate Generator	ORTEC	416A
ADCAM MCB	ORTEC	926
Oscilloscope	Tektronix	DPO 7104

B.2 Energy Window Setup

To set the window on the SCA, the voltage levels of the detector signal associated with the desired energy must be determined. A multi-channel analyzing program, such as 'GammaVision' is used to determine the appropriate energy window. First, an isotope (or multiple isotopes) with known gamma energies are placed near the detector, and the signal is collected by GammaVision, displaying the cumulative energy spectra. The peaks on the program can then be identified, and GammaVision can be calibrated.

The Multi-Channel Buffer (MCB), which accepts a 0 V to 10 V signal to pass to GammaVision, will accept a second signal to use as a gate. By connecting the gate generator to the gate of the MCB, shown as optional in Figure 49, GammaVision will collect the spectra of the signal that corresponds to the currently selected window on the SCA. An oscilloscope and a delay amplifier are useful to ensure that the split signal and generated gate coincide at the MCB.

Finally, the window can be set. Using a 514 keV ^{85}Sr source to simulate the 511 keV annihilation photons, and starting with SCA-set window fully open, the window can be slowly narrowed. The spectra counts displayed by GammaVision will increase only within the narrowing window. When GammaVision is only adding counts at the desired energies, the window is set.

Bibliography

1. Adamiv, Volodymyr T., Yaroslav V. Burak, David J. Wooten, John McClory, James Petrosky, Ihor Ketsman, Jie Xiao, Yaroslav B. Losovyj, and Peter A. Dowben. "The Electronic Structure and Secondary Pyroelectric Properties of Lithium Tetraborate". *Materials*, 3(9):4550–4579, 2010. ISSN 1996-1944. URL http://www.mdpi.com/1996-1944/3/9/4550.

2. Alichanian, A. I., A. I. Alichanow, and L. A. Arzimovitch. "Conservation of Momentum in the Process of Positron Annihilation". *Nature*, 137:703–704, April 1936.

3. Anderson, Carl D. "The Positive Electron". *Phys. Rev.*, 43:491–494, Mar 1933. URL http://link.aps.org/doi/10.1103/PhysRev.43.491.

4. Anderson, Carl D. "The production and properties of positrons". Nobel Lecture, December 1936.

5. Aroyo, Mois I., Danel Orobengoa, Gemma de la Flor, Emre S. Tasci, J. Manuel Perez-Mato, and Hans Wondratschek. "Brillouin-zone database on the *Bilbao Crystallographic Server*". *Acta Crystallographica Section A*, 70(2):126–137, Mar 2014. URL http://dx.doi.org/10.1107/S205327331303091X.

6. Asoka-Kumar, P. and K. G. Lynn. "Implantation profile of low-energy positrons in solids". *Applied Physics Letters*, 57(16):1634–1636, 1990.

7. Barnes, L. D., S. J. Gilbert, and C. M. Surko. "Energy-resolved positron annihilation for molecules". *Phys. Rev. A*, 67:032706, Mar 2003. URL http://link.aps.org/doi/10.1103/PhysRevA.67.032706.

8. Bell, R. E. and R. L. Graham. "Time Distribution of Positron Annihilation in Liquids and Solids". *Phys. Rev.*, 90:644–654, May 1953. URL http://link.aps.org/doi/10.1103/PhysRev.90.644.

9. Berger, M.J., J.H. Hubbell, S.M. Seltzer, J. Chang, J.S. Coursey, R. Sukumar, D.S. Zucker, and K. Olsen. "XCOM: Photon Cross Sections Database (Version 1.5)", 2010. URL http://physics.nist.gov/xcom.

10. Beringer, Robert and Carol Gray Montgomery. "The angular distribution of positron annihilation radiation". *Physical Review*, 61(5-6):222, 1942.

11. Berko, S., M. Haghgooie, and J. J. Mader. "Momentum density measurements with a new multicounter two-dimensional angular correlation of annihilation radiation apparatus". *Physics Letters A*, 63(3):335–338, 11 1977. URL http://www.sciencedirect.com/science/article/pii/0375960177909227.

12. Berko, Stephan and Frank Hereford. "Experimental Studies of Positron Interactions in Solids and Liquids". *Rev. Mod. Phys.*, 28:299–307, Jul 1956. URL http://link.aps.org/doi/10.1103/RevModPhys.28.299.

13. Bhabha, H.J. and H.R. Hulme. "The Annihilation of Fast Positrons by Electrons in the K-Shell". *Proceedings of the Royal Society of London. Series A*, 1934.

14. Blackett, P. M. S. and G. P. S. Occhialini. "Some Photographs of the Tracks of Penetrating Radiation". *Proceedings of the Royal Society of London. Series A, Containing Papers of a Mathematical and Physical Character*, 139(839):699–726, March 1933.

15. Brown, Lowell S. and Gerald Gabrielse. "Geonium theory: Physics of a single electron or ion in a Penning trap". *Rev. Mod. Phys.*, 58:233–311, Jan 1986. URL http://link.aps.org/doi/10.1103/RevModPhys.58.233.

16. Burks, M., E. Jordan, E. Hull, L. Mihailescu, and K. Vetter. "Signal interpolation in germanium detectors for improved 3-D position resolution". *Nuclear Science Symposium Conference Record, 2004 IEEE*, volume 2, 1114–1118. 2004. ISSN 1082-3654.

17. Burks, M.T., Mark Amman, Steven E. Boggs, E.L. Hull, Paul N. Luke, N.W. Madden, V.J. Riot, and K.-P. Ziock. "A germanium gamma ray imager with 3D position sensitivity". *Nuclear Science Symposium Conference Record, 2001 IEEE*, volume 1, 223–225 vol.1. 2001. ISSN 1082-3654.

18. Cassidy, D. B., S. H. M. Deng, R. G. Greaves, and A. P. Mills. "Accumulator for the production of intense positron pulses". *Review of Scientific Instruments*, 77(7):073106, 2006. URL http://scitation.aip.org/content/aip/journal/rsi/77/7/10.1063/1.2221509.

19. Ceeh, Hubert, Josef-Andreas Weber, Michael Leitner, Peter Böni, and Christoph Hugenschmidt. "Performance of the new 2D ACAR spectrometer in Munich". *ArXiv e-prints*, 10 2012. URL http://arxiv.org/abs/1210.3497.

20. Ceeh, Hubert, Josef Andreas Weber, Michael Leitner, Peter Boni, and Christoph Hugenschmidt. "The source-sample stage of the new two-dimensional angular correlation of annihilation radiation spectrometer at Technische Universität München". *Review of Scientific Instruments*, 84(4):043905–043905–7, 2013. ISSN 0034-6748.

21. Charlton, M. and J.W. Humberston. *Positron Physics*. Cambridge University Press, 2001.

22. Costello, D. G., D. E. Groce, D. F. Herring, and J. Wm. McGowan. "Evidence for the Negative Work Function Associated with Positrons in Gold". *Phys. Rev. B*, 5:1433–1436, Feb 1972. URL http://link.aps.org/doi/10.1103/PhysRevB.5.1433.

23. DeBenedetti, S., C. E. Cowan, W. R. Konneker, and H. Primakoff. "On the Angular Distribution of Two-Photon Annihilation Radiation". *Phys. Rev.*, 77:205–212, Jan 1950. URL http://link.aps.org/doi/10.1103/PhysRev.77.205.

24. Deutsch, Martin. "Evidence for the Formation of Positronium in Gases". *Phys. Rev.*, 82:455–456, May 1951. URL http://link.aps.org/doi/10.1103/PhysRev.82.455.

25. Dirac, Paul AM. "The quantum theory of the electron". *Proceedings of the Royal Society of London. Series A, Containing Papers of a Mathematical and Physical Character*, 117(778):610–624, 1928.

26. Dirac, Paul AM. "A theory of electrons and protons". *Proceedings of the Royal Society of London. Series A*, 126(801):360–365, 1930.

27. Dirac, Paul AM. "Quantised Singularities in the Electromagnetic Field". *Proceedings of the Royal Society of London. Series A, Containing Papers of a Mathematical and Physical Character*, 133(821):60–72, September 1931.

28. Dryzek, Jerzy and Paweł Horodek. "Positron implantation profiles in layered samples". *Nuclear Instruments and Methods in Physics Research Section B: Beam Interactions with Materials and Atoms*, 267(21–22):3580–3589, 11 2009. URL http://www.sciencedirect.com/science/article/pii/S0168583X09009148.

29. Dumond, J., D. Lind, and B. Watson. "Precision Measurement of the Wave-Length and Spectral Profile of the Annihilation Radiation from Cu^{64} with the Two-Meter Focusing Curved Crystal Spectrometer". *Phys. Rev.*, 75:1226–1239, Apr 1949. URL http://link.aps.org/doi/10.1103/PhysRev.75.1226.

30. Dupasquier, A., A.P. Mills, and R.S. Brusa. *Physics with Many Positrons, Proc. Int. School of Physics Enrico Fermi*. IOS Press, 2010.

31. Eichler, S., C. Hübner, and R. Krause-Rehberg. "A Monte-Carlo simulation of positron diffusion in solids". *Applied Surface Science*, 116(0):155 – 161, 1997. ISSN 0169-4332. URL http://www.sciencedirect.com/science/article/pii/S016943329601046X. Proceedings of the Seventh International Workshop on Slow-Positron Beam Techniques for Solids and Surfaces.

32. Fagan-Kelly, Stefan B. *Three-Dimensional Positron Annihilation Momentum Spectroscopy of Lithium Tetraborate Crystals*. Master's thesis, Air Force Institute of Technology, March 2013.

33. Falub, C.V. *The Delft intense slow positron beam 2D-ACAR facility for analysis of nanocavities and quantum dots*. Ph.D. thesis, Delft University of Technology, 2002.

34. FitzGerald, Jack G. *A Programmable Liquid Collimator for Both Coded Aperture Adaptive Imaging and Multiplexed Compton Scatter Tomography*. Master's thesis, Air Force Institute of Technology, March 2012.

35. Gilbert, S. J., L. D. Barnes, J. P. Sullivan, and C. M. Surko. "Vibrational-Resonance Enhancement of Positron Annihilation in Molecules". *Phys. Rev. Lett.*, 88:043201, Jan 2002. URL http://link.aps.org/doi/10.1103/PhysRevLett.88.043201.

36. Gilbert, S. J., C. Kurz, R. G. Greaves, and C. M. Surko. "Creation of a monoenergetic pulsed positron beam". *Applied Physics Letters*, 70(15):1944–1946, 1997. ISSN 0003-6951.

37. Gilbert, Steven Jay. *A new ultra-cold positron beam and applications to low-energy positron scattering and electron-positron plasmas*. Ph.D. thesis, University of California, San Diego, 2000.

38. Greaves, R. G. and C. M. Surko. "Solid neon moderator for positron-trapping experiments". *Canadian Journal of Physics*, 74(7-8):445–448, 2013/08/11 1996. URL http://dx.doi.org/10.1139/p96-063.

39. Greaves, R. G. and C. M. Surko. "Inward Transport and Compression of a Positron Plasma by a Rotating Electric Field". *Physical Review Letters*, 85(9):1883–1886, 2000.

40. Green, R. and A. Stewart. "Angular Correlation of Photons from Positron Annihilation in Light Metals". *Phys. Rev.*, 98:486–491, Apr 1955. URL http://link.aps.org/doi/10.1103/PhysRev.98.486.

41. Gribakin, G. F., J. A. Young, and C. M. Surko. "Positron-molecule interactions: Resonant attachment, annihilation, and bound states". *Rev. Mod. Phys.*, 82:2557–2607, Sep 2010. URL http://link.aps.org/doi/10.1103/RevModPhys.82.2557.

42. Gribakin, GF and J Ludlow. "Enhancement of Positron-Atom Annihilation near the positronium formation threshold". *Physical review letters*, 88(16):163202, 2002.

43. Gullikson, E. M. and A. P. Mills. "Positron Dynamics in Rare-Gas Solids". *Phys. Rev. Lett.*, 57:376–379, Jul 1986. URL http://link.aps.org/doi/10.1103/PhysRevLett.57.376.

44. Haghgooie, M., J. J. Mader, and S. Berko. "Direct observation of the high-momentum components of the conduction band of copper by two-dimensional angular correlation of annihilation radiation". *Physics Letters A*, 69(4):293–296, 12 1978. URL http://www.sciencedirect.com/science/article/pii/0375960178901913.

45. Hayward, Jason P. *Charge loss correction and inter-strip interpolation in a high-purity germanium double-sided strip detector*. Ph.D. thesis, University of Michigan, 2008.

46. Hayward, J.P. and D.K. Wehe. "Inter-Strip Interpolation Measurements in a High-Purity Germanium Double-Sided Strip Detector". *Nuclear Science, IEEE Transactions on*, 56(3):800–807, June 2009. ISSN 0018-9499.

47. He, Zhong. "Review of the Shockley-Ramo theorem and its application in semiconductor gamma-ray detectors". *Nuclear Instruments and Methods in Physics Research Section A: Accelerators, Spectrometers, Detectors and Associated Equipment*, 463(1-2):250–267, 5 2001. URL http://www.sciencedirect.com/science/article/pii/S0168900201002236.

48. Huang, X.-P., F. Anderegg, E. M. Hollmann, C. F. Driscoll, and T. M. O'Neil. "Steady-State Confinement of Non-neutral Plasmas by Rotating Electric Fields". *Physical Review Letters*, 78(5):875–878, 1997.

49. Hull, Ethan L., Morgan Burks, Chris P. Cork, William W. Craig, and Del Eckels. "Germanium orthogonal strip detector system for gamma-ray imaging". *Proc. SPIE 4507, Hard X-Ray and Gamma-Ray Detector Physics*, III(132), 2001.

50. Iwata, Koji, G. F. Gribakin, R. G. Greaves, C. Kurz, and C. M. Surko. "Positron annihilation on large molecules". *Phys. Rev. A*, 61:022719, Jan 2000. URL http://link.aps.org/doi/10.1103/PhysRevA.61.022719.

51. Jean, Y. C., P. E. Mallon, and D. M Schrader. *Principles and Applications of Positron and Positronium Chemistry*. World Scientific, New Jersey, 2003.

52. Jiménez, Stephen M. *Design and Characterization of a Three-Dimensional Positron Annihilation Spectroscopy System Using a Low-Energy Positron Beam*. Master's thesis, Air Force Institute of Technology, March 2012.

53. Klemperer, Otto. "On the annihilation radiation of the positron". *Mathematical Proceedings of the Cambridge Philosophical Society*, 30:347–354, 7 1934. ISSN 1469-8064. URL http://journals.cambridge.org/article_S0305004100012536.

54. Knoll, Glenn F. *Radiation detection and measurement*. John Wiley & Sons, Inc., New York, 3rd edition, 2000.

55. Krause-Rehberg, Reinhard and Hartmut S. Leipner. *Positron Annihilation in Semiconductors*. Springer, 1999.

56. Kroeger, R. A, N Gehrels, W. N Johnson, J. D Kurfess, B. P Phlips, and J Tueller. "Charge spreading and position sensitivity in a segmented planar germanium detector". *Nuclear Instruments and Methods in Physics Research Section A: Accelerators, Spectrometers, Detectors and Associated Equipment*, 422(1–3):206–210, 2 1999. URL http://www.sciencedirect.com/science/article/pii/S016890029801095X.

57. Kruseman, Abraham Cornelis. *Two-Dimensional ACAR and Low-Background DBAR Studies on Materials with Defects*. Ph.D. thesis, Delft University of Technology, 1999.

58. Kubica, P. and A. T. Stewart. "Positron motion in metals". *Canadian Journal of Physics*, 61(7):971–978, 2014/07/08 1983. URL http://dx.doi.org/10.1139/p83-120.

59. Lock, D G, V H C Crisp, and R N West. "Positron annihilation and Fermi surface studies: a new approach". *Journal of Physics F: Metal Physics*, 3(3):561, 1973. URL http://stacks.iop.org/0305-4608/3/i=3/a=014.

60. Lynn, K., J. MacDonald, R. Boie, L. Feldman, J. Gabbe, M. Robbins, E. Bonderup, and J. Golovchenko. "Positron-Annihilation Momentum Profiles in Aluminum: Core Contribution and the Independent-Particle Model". *Phys. Rev. Lett.*, 38:241–244, Jan 1977. URL http://link.aps.org/doi/10.1103/PhysRevLett.38.241.

61. McKelvey, John Philip. *Solid state physics for engineering and materials science*. Krieger Publishing Company, 1993.

62. Mills, A.P. and E.M. Gullikson. "Solid neon moderator for producing slow positrons". *Applied Physics Letters*, 49(17):1121–1123, 1986. ISSN 0003-6951.

63. Murphy, T. J. and C. M. Surko. "Positron trapping in an electrostatic well by inelastic collisions with nitrogen molecules". *Phys. Rev. A*, 46:5696–5705, Nov 1992. URL http://link.aps.org/doi/10.1103/PhysRevA.46.5696.

64. Murray, G. "The Doppler broadening of annihilation radiation". *Physics Letters B*, 24(6):268–269, 3 1967. URL http://www.sciencedirect.com/science/article/pii/0370269367904431.

65. National Instruments. "What Is the Definition of a TTL (Transistor-Transistor Logic) Compatible Signal?", 2002. URL http://digital.ni.com/public.nsf/allkb/ACB4BD7550C4374C86256BFB0067A4BD.

66. Oppenheimer, J. "Two Notes On the Probability of Radiative Transitions". *Phys. Rev.*, 35:939–947, Apr 1930. URL http://link.aps.org/doi/10.1103/PhysRev.35.939.

67. Ore, A. and J. L. Powell. "Three-Photon Annihilation of an Electron-Positron Pair". *Phys. Rev.*, 75:1696–1699, Jun 1949. URL http://link.aps.org/doi/10.1103/PhysRev.75.1696.

68. Pikart, Philip and Christoph Hugenschmidt. "Determination of electron binding energies in two-dimensional Coincident Doppler Broadening spectra". *Journal of Physics: Conference Series*, 443(1):012089, 2013. URL http://stacks.iop.org/1742-6596/443/i=1/a=012089.

69. Puska, Martti J and RM Nieminen. "Theory of positrons in solids and on solid surfaces". *Reviews of modern Physics*, 66(3):841, 1994.

70. Rabou, L. P. L. M. and P. E. Mijnarends. "Approximate validity of the Lock-Crisp-West theorem in positron annihilation". *Solid State Communications*, 52(11):933–936, 12 1984. URL http://www.sciencedirect.com/science/article/pii/0038109884908597.

71. Rich, A., J. Van House, D.W. Gidley, R.S. Conti, and P.W. Zitzewitz. "Spin-polarized low-energy positron beams and their applications". *Applied Physics A*, 43(4):275–281, 1987. ISSN 0947-8396. URL http://dx.doi.org/10.1007/BF00635183.

72. Rossi, G., J. Morse, and D. Protic. "Energy and position resolution of germanium microstrip detectors at X-ray energies from 15 to 100 keV". *Nuclear Science, IEEE Transactions on*, 46(3):765–773, 1999. ISSN 0018-9499.

73. Rozing, G. J., P. E. Mijnarends, A. A. Menovsky, and P. F. de Chtel. "Positron-annihilation study of the electronic structure of URu_2Si_2". *Phys. Rev. B*, 43:9523–9531, Apr 1991. URL http://link.aps.org/doi/10.1103/PhysRevB.43.9523.

74. Ruark, Arthur. "Positronium". *Phys. Rev.*, 68:278–278, Dec 1945. URL http://link.aps.org/doi/10.1103/PhysRev.68.278.

75. Serway, Raymond A., Clement J. Moses, and Curt A. Moyer. *Modern Physics*. Saunders College Publishing, 2nd edition, 1997.

76. Shockley, W. "Currents to Conductors Induced by a Moving Point Charge". *Journal of Applied Physics*, 9(10):635–636, 1938. URL http://scitation.aip.org/content/aip/journal/jap/9/10/10.1063/1.1710367.

77. Singru, R. M. "Novel approach to study angular correlation of positron annihilation radiation". *Physics Letters A*, 46(1):61–62, 11 1973. URL http://www.sciencedirect.com/science/article/pii/0375960173906853.

78. Singru, R. M. "Measurement of the angular correlation of positron annihilation radiation using a Ge(Li) detector". *Journal of Physics and Chemistry of Solids*, 35(1):33–35, 1 1974. URL http://www.sciencedirect.com/science/article/pii/0022369774900067.

79. Smedskjaer, L.C. and D.G. Legnini. "A study on symmetrization of 2D {ACAR} positron annihilation data". *Nuclear Instruments and Methods in Physics Research Section A: Accelerators, Spectrometers, Detectors and Associated Equipment*, 292(2):487 – 493, 1990. ISSN 0168-9002. URL http://www.sciencedirect.com/science/article/pii/016890029090406V.

80. Spieler, Helmuth. *Semiconductor Detector Systems*. Oxford University Press, 2005.

81. Stevenson, Alexander W. *Improving the Efficiency of Photon Collection by Compton Rescue*. Master's thesis, Air Force Institute of Technology, March 2011.

82. Suresh, Sagadevan. "Synthesis, structural and dielectric properties of zinc sulfide nanoparticles". *International Journal of Physical Sciences*, Vol. 8(21):pp. 1121–1127, 9 June 2013.

83. Surko, C. M. and R. G. Greaves. "Emerging science and technology of antimatter plasmas and trap-based beams". *Physics of Plasmas (1994-present)*, 11(5):2333–2348, 2004.

84. Surko, C. M., M. Leventhal, Crane W.S., and A.P Mills. "The Positron Trap – A New Tool for Plasma Physics". KF Canter, PH Lippel, WS Crane, and AP Mills Jr (editors), *Positron Studies of Solids, Surfaces, and Atoms*. World Scientific, Singapore, 1986.

85. Surko, Clifford M., G.F. Gribakin, and Stephen J. Buckman. "Low-energy positron interactions with atoms and molecules". *Journal of Physics B: Atomic, Molecular and Optical Physics*, 38(6):R57, 2005.

86. Tasci, E.S., de la Flor, G., Orobengoa, D., Capillas, C., Perez-Mato, J.M., and Aroyo, M.I. "An introduction to the tools hosted in the Bilbao Crystallographic Server". *EPJ Web of Conferences*, 22:00009, 2012. URL http://dx.doi.org/10.1051/epjconf/20122200009.

87. Vehanen, A., K. Saarinen, P. Hautojärvi, and H. Huomo. "Profiling multilayer structures with monoenergetic positrons". *Phys. Rev. B*, 35:4606–4610, Apr 1987. URL http://link.aps.org/doi/10.1103/PhysRevB.35.4606.

88. Weber, M., A. Schwab, D. Beckek, and K. G. Lynn. "Solid neon moderated electrostatic or magnetic positron beam". 73(1-2):147–157, 1992. URL http://dx.doi.org/10.1007/BF02628215.

89. West, R. N. *Positron Spectroscopy of Solids*, chapter Positron Studies of the Electronic Structure of Solids, 75–143. IOS Press, 1995.

90. West, R N, J Mayers, and P A Walters. "A high-efficiency two-dimensional angular correlation spectrometer for positron studies". *Journal of Physics E: Scientific Instruments*, 14(4):478, 1981. URL http://stacks.iop.org/0022-3735/14/i=4/a=021.

91. Williams, Christopher S. *Three-Dimensional Positron Annihilation Momentum Measurement Technique Applied To Measure Oxygen-Atom Defects in 6H Silicon Carbide*. Ph.D. thesis, Air Force Institute of Technology, March 2010.

92. Williams, C.S., W.P. Baker, Larry W. Burggraf, P.E. Adamson, and J.C. Petrosky. "Toward Simultaneous 2D ACAR and 2D DBAR: Sub-Pixel Spatial Characterization of a Segmented HPGe Detector Using Transient Charges". *Nuclear Science, IEEE Transactions on*, 57(2):860–869, 2010. ISSN 0018-9499.

93. Wooten, David. *Electronic Structure of Lithium Tetraborate*. Ph.D. thesis, Air Force Institute of Technology, June 2010.

94. Wulf, Eric A., Bernard F. Phlips, W.N. Johnson, J.D. Kurfess, C.J. Lister, and F. Kondev. "Strip interpolation in silicon and germanium strip detectors". *Nuclear Science Symposium Conference Record, 2004 IEEE*, volume 2, 925–929. 2004. ISSN 1082-3654.

Vita

Maj Angelo Bonavita graduated from Embry-Riddle Aeronautical University with a Bachelor's degree in Engineering Physics in 2002, and a Master's degree in Nuclear Engineering from the Air Force Institute of Technology in 2004.

REPORT DOCUMENTATION PAGE

Form Approved
OMB No. 0704–0188

The public reporting burden for this collection of information is estimated to average 1 hour per response, including the time for reviewing instructions, searching existing data sources, gathering and maintaining the data needed, and completing and reviewing the collection of information. Send comments regarding this burden estimate or any other aspect of this collection of information, including suggestions for reducing this burden to Department of Defense, Washington Headquarters Services, Directorate for Information Operations and Reports (0704–0188), 1215 Jefferson Davis Highway, Suite 1204, Arlington, VA 22202–4302. Respondents should be aware that notwithstanding any other provision of law, no person shall be subject to any penalty for failing to comply with a collection of information if it does not display a currently valid OMB control number. **PLEASE DO NOT RETURN YOUR FORM TO THE ABOVE ADDRESS.**

1. REPORT DATE *(DD–MM–YYYY)*	2. REPORT TYPE	3. DATES COVERED *(From — To)*
24–03–2016	Dissertation	Aug 2011 — Mar 2016

4. TITLE AND SUBTITLE

APPLICATIONS OF CORRELATED 2D-ACAR AND CDBAR USING A LOW-ENERGY POSITRON BEAM

5a. CONTRACT NUMBER

5b. GRANT NUMBER

5c. PROGRAM ELEMENT NUMBER

6. AUTHOR(S)

Bonavita, Angelo M., Maj, USAF

5d. PROJECT NUMBER

5e. TASK NUMBER

5f. WORK UNIT NUMBER

7. PERFORMING ORGANIZATION NAME(S) AND ADDRESS(ES)

Air Force Institute of Technology
Graduate School of Engineering and Management (AFIT/EN)
2950 Hobson Way
WPAFB OH 45433-7765

8. PERFORMING ORGANIZATION REPORT NUMBER

AFIT-ENP-DS-16-M-056

9. SPONSORING / MONITORING AGENCY NAME(S) AND ADDRESS(ES)

AFOSR/RSA (Dr. Michael R. Berman)
875 North Randolph Street, Room 3112
Arlington VA 22203
Tele: (703)696-7781, DSN: 426-7781, FAX: (703)696-7320,
michael.berman@afosr.af.mil

10. SPONSOR/MONITOR'S ACRONYM(S)

AFOSR/MOA

11. SPONSOR/MONITOR'S REPORT NUMBER(S)

12. DISTRIBUTION / AVAILABILITY STATEMENT

DISTRIBUTION STATEMENT A. APPROVED FOR PUBLIC RELEASE; DISTRIBUTION UNLIMITED.

13. SUPPLEMENTARY NOTES

14. ABSTRACT

The three-dimensional positron annihilation spectroscopy system (3D-PASS) at the Air Force Institute of Technology (AFIT) correlates coincidence Doppler broadening of annihilation radiation with two-dimensional angular correlation of annihilation radiation measurements using two position-sensitive, high-purity germanium (HPGe) detectors. The low photoelectric cross section of germanium, combined with the limited output of the radioisotope-based positron beam, produced sparse data necessitating careful data extraction. Processing techniques employed to increase 3D-PASS spectra quality include an improved algorithm for determining radiation-interaction position on HPGe double-sided strip detectors, a momentum sampling function based correction scheme and spectra folding informed by crystal symmetries. The 3D nature of the correlated data allowed for leveraging multiple axes of crystal symmetry and producing 2D momentum plots along different projection directions. Integration of the 3D-PASS with a low-energy positron beam enables future studies of enhanced annihilation as well as nondestructive characterization of material surfaces.

15. SUBJECT TERMS

positron, positron annihilation spectroscopy, angular correlation of annihilation radiation, Doppler broadening of annihilation radiation, low-energy positron beam, three-dimensional positron annihilation momentum measurement

16. SECURITY CLASSIFICATION OF:			17. LIMITATION OF ABSTRACT	18. NUMBER OF PAGES	19a. NAME OF RESPONSIBLE PERSON
a. REPORT	b. ABSTRACT	c. THIS PAGE			Dr. Larry W. Burggraf
U	U	U	U	126	19b. TELEPHONE NUMBER *(include area code)* (937) 255-3636, x4507; larry.burggraf@afit.edu